

A. C. Susceptibility Measurements
on the $\text{Ce}(\text{Fe}_{1-x}\text{Ru}_x)_2$ System

BY

DI WANG

A Thesis
Submitted to the Faculty of Graduate Studies
in Partial Fulfillment of the Requirements
for the Degree of

MASTER OF SCIENCE

Department of Physics
University of Manitoba
Winnipeg, Manitoba

(c) July, 1994

Name

Di Wang

Dissertation Abstracts International is arranged by broad, general subject categories. Please select the one subject which most nearly describes the content of your dissertation. Enter the corresponding four-digit code in the spaces provided.

Physics, Solid State

SUBJECT TERM

0611

SUBJECT CODE

U·M·I

Subject Categories

THE HUMANITIES AND SOCIAL SCIENCES

COMMUNICATIONS AND THE ARTS

Architecture 0729
 Art History 0377
 Cinema 0900
 Dance 0378
 Fine Arts 0357
 Information Science 0723
 Journalism 0391
 Library Science 0399
 Mass Communications 0708
 Music 0413
 Speech Communication 0459
 Theater 0465

EDUCATION

General 0515
 Administration 0514
 Adult and Continuing 0516
 Agricultural 0517
 Art 0273
 Bilingual and Multicultural 0282
 Business 0688
 Community College 0275
 Curriculum and Instruction 0727
 Early Childhood 0518
 Elementary 0524
 Finance 0277
 Guidance and Counseling 0519
 Health 0680
 Higher 0745
 History of 0520
 Home Economics 0278
 Industrial 0521
 Language and Literature 0279
 Mathematics 0280
 Music 0522
 Philosophy of 0998
 Physical 0523

Psychology 0525
 Reading 0535
 Religious 0527
 Sciences 0714
 Secondary 0533
 Social Sciences 0534
 Sociology of 0340
 Special 0529
 Teacher Training 0530
 Technology 0710
 Tests and Measurements 0288
 Vocational 0747

LANGUAGE, LITERATURE AND LINGUISTICS

Language
 General 0679
 Ancient 0289
 Linguistics 0290
 Modern 0291
 Literature
 General 0401
 Classical 0294
 Comparative 0295
 Medieval 0297
 Modern 0298
 African 0316
 American 0591
 Asian 0305
 Canadian (English) 0352
 Canadian (French) 0355
 English 0593
 Germanic 0311
 Latin American 0312
 Middle Eastern 0315
 Romance 0313
 Slavic and East European 0314

PHILOSOPHY, RELIGION AND THEOLOGY

Philosophy 0422
 Religion
 General 0318
 Biblical Studies 0321
 Clergy 0319
 History of 0320
 Philosophy of 0322
 Theology 0469

SOCIAL SCIENCES

American Studies 0323
 Anthropology
 Archaeology 0324
 Cultural 0326
 Physical 0327
 Business Administration
 General 0310
 Accounting 0272
 Banking 0770
 Management 0454
 Marketing 0338
 Canadian Studies 0385
 Economics
 General 0501
 Agricultural 0503
 Commerce-Business 0505
 Finance 0508
 History 0509
 Labor 0510
 Theory 0511
 Folklore 0358
 Geography 0366
 Gerontology 0351
 History
 General 0578

Ancient 0579
 Medieval 0581
 Modern 0582
 Black 0328
 African 0331
 Asia, Australia and Oceania 0332
 Canadian 0334
 European 0335
 Latin American 0336
 Middle Eastern 0333
 United States 0337
 History of Science 0585
 Law 0398
 Political Science
 General 0615
 International Law and
 Relations 0616
 Public Administration 0617
 Recreation 0814
 Social Work 0452
 Sociology
 General 0626
 Criminology and Penology 0627
 Demography 0938
 Ethnic and Racial Studies 0631
 Individual and Family
 Studies 0628
 Industrial and Labor
 Relations 0629
 Public and Social Welfare 0630
 Social Structure and
 Development 0700
 Theory and Methods 0344
 Transportation 0709
 Urban and Regional Planning 0999
 Women's Studies 0453

THE SCIENCES AND ENGINEERING

BIOLOGICAL SCIENCES

Agriculture
 General 0473
 Agronomy 0285
 Animal Culture and
 Nutrition 0475
 Animal Pathology 0476
 Food Science and
 Technology 0359
 Forestry and Wildlife 0478
 Plant Culture 0479
 Plant Pathology 0480
 Plant Physiology 0817
 Range Management 0777
 Wood Technology 0746
 Biology
 General 0306
 Anatomy 0287
 Biostatistics 0308
 Botany 0309
 Cell 0379
 Ecology 0329
 Entomology 0353
 Genetics 0369
 Limnology 0793
 Microbiology 0410
 Molecular 0307
 Neuroscience 0317
 Oceanography 0416
 Physiology 0433
 Radiation 0821
 Veterinary Science 0778
 Zoology 0472
 Biophysics
 General 0786
 Medical 0760
 EARTH SCIENCES
 Biogeochemistry 0425
 Geochemistry 0996

Geodesy 0370
 Geology 0372
 Geophysics 0373
 Hydrology 0388
 Mineralogy 0411
 Paleobotany 0345
 Paleocology 0426
 Paleontology 0418
 Paleozoology 0985
 Palynology 0427
 Physical Geography 0368
 Physical Oceanography 0415

HEALTH AND ENVIRONMENTAL SCIENCES

Environmental Sciences 0768
 Health Sciences
 General 0566
 Audiology 0300
 Chemotherapy 0992
 Dentistry 0567
 Education 0350
 Hospital Management 0769
 Human Development 0758
 Immunology 0982
 Medicine and Surgery 0564
 Mental Health 0347
 Nursing 0569
 Nutrition 0570
 Obstetrics and Gynecology 0380
 Occupational Health and
 Therapy 0354
 Ophthalmology 0381
 Pathology 0571
 Pharmacology 0419
 Pharmacy 0572
 Physical Therapy 0382
 Public Health 0573
 Radiology 0574
 Recreation 0575

Speech Pathology 0460
 Toxicology 0383
 Home Economics 0386

PHYSICAL SCIENCES

Pure Sciences

Chemistry
 General 0485
 Agricultural 0749
 Analytical 0486
 Biochemistry 0487
 Inorganic 0488
 Nuclear 0738
 Organic 0490
 Pharmaceutical 0491
 Physical 0494
 Polymer 0495
 Radiation 0754
 Mathematics 0405
 Physics
 General 0605
 Acoustics 0986
 Astronomy and
 Astrophysics 0606
 Atmospheric Science 0608
 Atomic 0748
 Electronics and Electricity 0607
 Elementary Particles and
 High Energy 0798
 Fluid and Plasma 0759
 Molecular 0609
 Nuclear 0610
 Optics 0752
 Radiation 0756
 Solid State 0611
 Statistics 0463
 Applied Sciences
 Applied Mechanics 0346
 Computer Science 0984

Engineering
 General 0537
 Aerospace 0538
 Agricultural 0539
 Automotive 0540
 Biomedical 0541
 Chemical 0542
 Civil 0543
 Electronics and Electrical 0544
 Heat and Thermodynamics 0348
 Hydraulic 0545
 Industrial 0546
 Marine 0547
 Materials Science 0794
 Mechanical 0548
 Metallurgy 0743
 Mining 0551
 Nuclear 0552
 Packaging 0549
 Petroleum 0765
 Sanitary and Municipal
 System Science 0790
 Geotechnology 0428
 Operations Research 0796
 Plastics Technology 0795
 Textile Technology 0994

PSYCHOLOGY

General 0621
 Behavioral 0384
 Clinical 0622
 Developmental 0620
 Experimental 0623
 Industrial 0624
 Personality 0625
 Physiological 0989
 Psychobiology 0349
 Psychometrics 0632
 Social 0451



A. C. Susceptibility Measurements on the $\text{Ce}(\text{Fe}_{1-x}\text{Ru}_x)_2$ System

BY

DI WANG

A Thesis submitted to the Faculty of Graduate Studies of the University of Manitoba in partial fulfillment of the requirements for the degree of

MASTER OF SCIENCE

© 1994

Permission has been granted to the LIBRARY OF THE UNIVERSITY OF MANITOBA to lend or sell copies of this thesis, to the NATIONAL LIBRARY OF CANADA to microfilm this thesis and to lend or sell copies of the film, and UNIVERSITY MICROFILMS to publish an abstract of this thesis.

The author reserves other publications rights, and neither the thesis nor extensive extracts from it may be printed or otherwise reproduced without the author's permission.

Abstract

Magnetic behaviour of intermetallic compound $\text{Ce}(\text{Fe}_{1-x}\text{Ru}_x)_2$ is studied through the method of a. c. magnetic susceptibility. Two samples, $\text{Ce}(\text{Fe}_{0.93}\text{Ru}_{0.07})_2$ and $\text{Ce}(\text{Fe}_{0.92}\text{Ru}_{0.08})_2$, are measured in detail. The field and temperature dependence of a. c. susceptibility gives evidence of the existence of sequential phase transitions from paramagnetic to ferromagnetic to antiferromagnetic state. The upper transition (paramagnetic to ferromagnetic) is analyzed with conventional scaling approach, yielding critical exponents δ , γ values close to Heisenberg predictions. The lower transition is studied through non-linear response. For the first time in ferromagnetic-antiferromagnetic transition, an anomaly in the initial slope of χ_t vs. H_i^2 , $a_2(T)$, is observed. Zero field susceptibility has revealed a considerable exchange bond disorder in $\text{Ce}(\text{Fe}_{1-x}\text{Ru}_x)_2$ compounds, increasing with Ru concentration. These facts suggest that CeFe_2 is of a certain kind of instability, thus the magnetic properties are dramatically affected by small level of substitution.

Acknowledgement

I'm grateful to my supervisor, Dr. G. Williams. I also wish to thank H. P. Kunkel for his help throughout the writing of this thesis.

Contents

1	Introduction	1
2	Theoretical Background	5
2.1	The Study of Critical Phenomena: The Power Law Behaviour	5
2.2	The Critical Point Exponents	6
2.3	Scaling Theory	9
2.3.1	The Basic Assumption in Scaling Theory	9
2.3.2	Scaling Predictions	10
2.4	Mean Field Theory	17
2.4.1	The Molecular Field	18
2.4.2	The Non-interacting Magnetic System	18
2.4.3	The Interacting Magnetic System	20
2.4.4	Critical Exponents in MFT	22
2.4.5	Comments on MFT	25
2.5	Interacting Many-particle Systems: the Generalized Heisenberg Model	26
2.5.1	The Exchange Interaction	26
2.5.2	Ising Model, D=1	28
2.5.3	Classical Heisenberg Model, D=3	29
2.5.4	Other Dimensions	29
2.6	S-K Model, Exchange Bond Disorder	30
3	The RFe₂ Series of Compounds	34
3.1	CeFe ₂	35
3.2	Ce(Fe _{1-x} Al _x) ₂	40
3.3	Ce(Fe _{1-x} Co _x) ₂	41
3.4	Ce(Fe _{1-x} Ru _x) ₂	42
4	Experimental Methods	44
4.1	Sample Preparation	44
4.2	Experimental Apparatus	46
4.2.1	The susceptometer	47
4.2.2	Sample Block and Location	51

4.2.3	Biasing Magnetic Field	51
4.2.4	Temperature control	52
4.2.5	Data Collection	53
5	Data Analysis and Results	55
5.1	Correction of Data	55
5.1.1	Zero Correction	55
5.1.2	Background Correction	56
5.1.3	Calibration and Normalization	56
5.1.4	Demagnetization Correction	57
5.2	Data Analysis for $\text{Ce}(\text{Fe}_{0.93}\text{Ru}_{0.07})_2$	61
5.2.1	Zero Field Susceptibility	61
5.2.2	The Ferromagnetic Transition	71
5.2.3	Low Temperature Transition	77
5.3	Data Analysis for $\text{Ce}(\text{Fe}_{0.92}\text{Ru}_{0.08})_2$	84
5.3.1	Zero Field Susceptibility	84
5.3.2	Ferromagnetic Transition	90
5.3.3	Low Temperature Transition	95
6	Discussion and Conclusion	103
6.1	A Summary	103
6.2	Discussion and Conclusion	111
6.2.1	The Ferromagnetic transition	111
6.2.2	The Low Temperature Transition	115
6.2.3	Phase Diagram	115
6.2.4	Conclusion	116
A	Homogeneous Function	118

Chapter 1

Introduction

Magnetic, thermal and transport properties in dilute magnetic systems have been the subject of intense study over the past several decades. Investigations of these random local moment systems have revealed evidence for the existence of sequential magnetic phase transitions from paramagnetic to ferromagnetic to a possible re-entrant (spin-glass) state at lower temperature. While the ferromagnetic transition has been unanimously agreed upon, there has been and continues to be both experimental and theoretical controversy over the occurrence of the second phase transition and the characteristics of the low temperature ground state. A wide range of experimental techniques have been applied in an attempt to provide conclusive evidence for the existence of this state, and hence an understanding of the magnetic structure/ordering, which is thought due ultimately to the $s - d$ interaction between the conduction electrons of the host metal and d electrons of the magnetic impurities (transition metal).

Some of the earliest experiments involving alloys containing transition metals which produced results suggestive of this type of double transition were carried out by Coles *et al* [1] on the AuFe system. At low Fe concentration, the a. c. magnetic susceptibility vs. temperature data exhibits a single sharp cusp [2] typical of a mag-

netic phase transition from the paramagnetic to spin-glass phase; with increasing Fe concentration, the cusp flattens out on the top, increases dramatically in magnitude and forms steep edges at both sides, as shown in figure 1.1, which became an accepted feature indicating a double phase transition. Similar features have been observed in numerous alloys and compounds as well as amorphous systems such as FeZr [5], however this feature is not always a conclusive indication of a reentrant phase, e.g. NiMn, PdMn. The ternary PdFeMn system shows this “classical” behaviour and has withstood the close scrutiny of further examinations by various techniques such as neutron-diffraction, Mössbauer effect, nonlinear response, etc., and continues to be viewed as an example of a true reentrant system. Detailed investigations of both the temperature and field dependence of the susceptibility have been conducted for the above system. These results generally agree with the predictions of, in particular, the most successful of the theoretical approaches, the Sherrington-Kirkpatrick (S-K) model [6].

The rare earth compound $Ce(Fe_{1-x}M_x)_2$, where M represents a transition metal substitution, is among those which display the above mentioned sequential phase transitions. From liquid helium temperature up to the Curie temperature of $240K$, $CeFe_2$ is ferromagnetically ordered, and becomes paramagnetic above $240K$. In $CeFe_2$ based compounds, where doping transition elements take the place of Fe atoms, the ferromagnetic region is considerably reduced on both high and low temperature sides, and a new phase appears at low temperature. Depending on the type and concentration of the substituting metal, the new phase varies from antiferromagnetic to spin-glass and so on. For ruthenium, neutron-diffraction measurements have shown this is in fact an antiferromagnetic ground state.

Based on previous work on $Ce(Fe_{1-x}M_x)_2$ alloys, the present experiment is in-

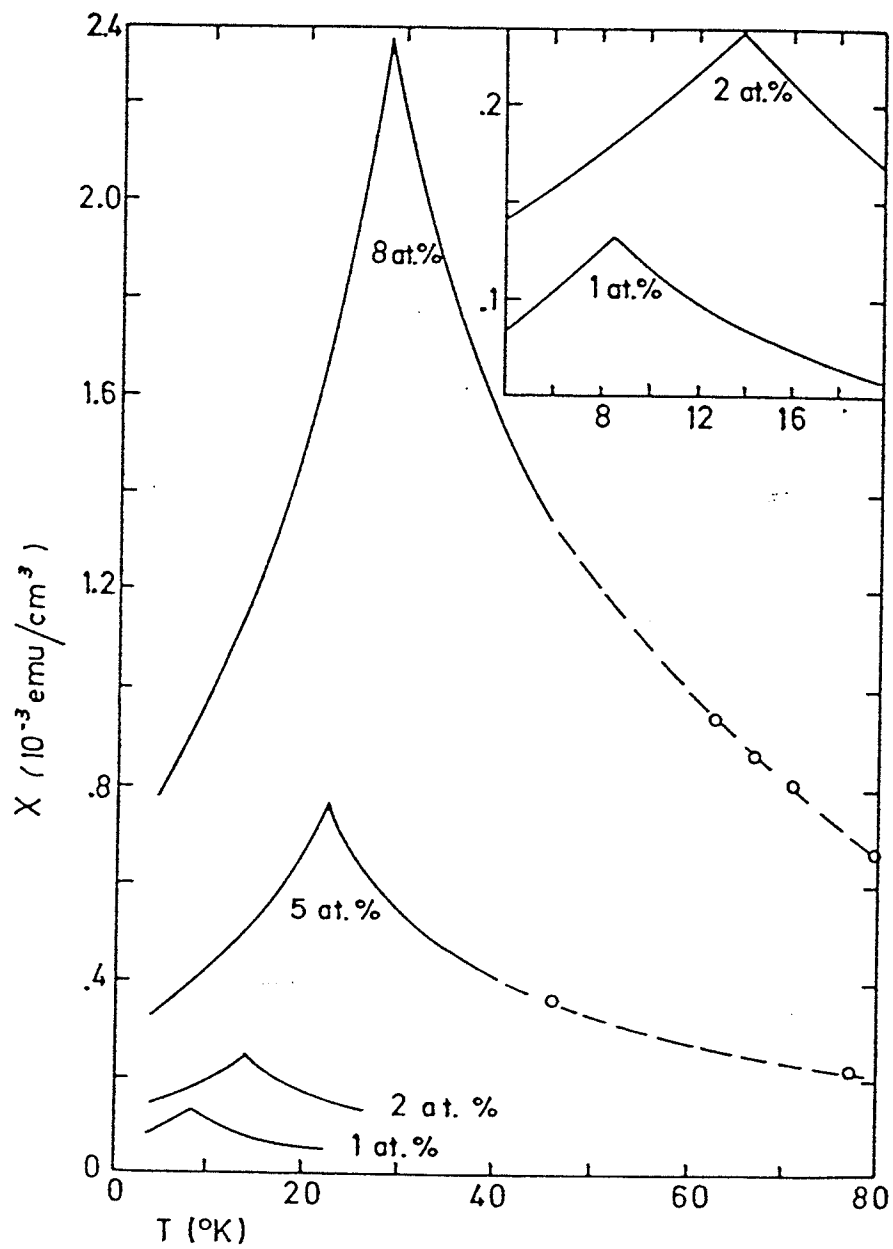


Figure 1.1: Susceptibility of Au-Fe system

tended to search for a more definitive manifestation of the existence of this new low temperature phase through the method of a. c. magnetic susceptibility and non-linear response, and to examine the effect of alloying concentration on both phase boundaries and other relevant parameters, such as the critical exponents and hence the mechanism of the formation of magnetic order.

In the following chapters we will first present the essential elements of some of the theoretical models used to describe and predict the behaviour of these magnetic systems and then turn to an overview of previous experimental results on some of the $\text{Ce}(\text{Fe}_{1-x}\text{M}_x)_2$ series of compounds. Chapter 4 describes the experimental apparatus, which is followed by the data analysis and results in chapter 5. The last chapter contains the discussion and the conclusion.

Chapter 2

Theoretical Background

2.1 The Study of Critical Phenomena: The Power Law Behaviour

The magnetic properties of materials and their variation with temperature and applied field can be very subtle and complicated. However, experiments have shown that for ferromagnets, quantities such as magnetic susceptibility χ , and magnetization M , invariably exhibit a sharp peak or step near the phase transition temperature T_c , and obey simple power laws in the vicinity of T_c of the form

$$\chi \propto t^{-\gamma} \quad (H = 0, T > T_c) \quad (2.1)$$

$$M \propto (-t)^\beta \quad (H = 0, T < T_c) \quad (2.2)$$

for the temperature dependence where $t = (T - T_c)/T_c$ represents the reduced temperature and

$$M \propto H^{1/\delta} \quad (T = T_c) \quad (2.3)$$

for the field dependence. Here γ , β , δ are the critical exponents defining these power law relations, their values can in principle be obtained from experimental data. Study of these critical indices has become a standard method in the process of exploring

critical phenomena in all kinds of systems undergoing a change of state including the magnetic systems to be discussed in this thesis. In this chapter we will review some of the theoretical models on magnetism and magnetic phase transition and in particular their predicted critical exponent values and compare these values with the available results from experimental data.

2.2 The Critical Point Exponents

The study of critical phenomena in general has mainly focused on the set of indices known as critical point exponents, which describe the power law behaviour of various quantities of interest in the vicinity of the critical point. Experimental results suggest that the state function $F(x)$ of a system being considered, where x is the possible state parameter, can be expressed in the following polynomial form (Stanley, 1971)

$$F(x) = F(0) x^a (1 + Ax^{a_1} + \dots) \quad (2.4)$$

where the coefficient A and the exponents a , a_1 , etc. are to be determined; $F(0)$ is simply a normalizing factor. In the neighbourhood of the critical point, $x \rightarrow 0$, and only the leading term is significant, so that

$$\frac{F(x)}{F(0)} = x^a \quad (2.5)$$

thus reducing to a simple power law relation with a being the exponent. Therefore the definition of critical exponents is valid only when the system is sufficiently close to the critical point. A deviation from this simplified relation is expected at larger x .

In a magnetic system, the dimensionless variable

$$t = \frac{T - T_c}{T_c} \quad (2.6)$$

is the reduced temperature generally adopted for convenience as a measure of the difference in temperature of the system from the critical point. The critical exponent is defined according to whether the critical point is approached from above or below, e.g.

$$\chi(T) \propto \begin{cases} (-t)^{-\gamma'} & (T < T_c, H = 0) \\ t^{-\gamma} & (T > T_c, H = 0) \end{cases}$$

defines the zero field susceptibility exponent γ and γ' , where γ and γ' may or may not be the same. Similarly

$$M(H, T = T_c) \propto H^{1/\delta} \quad (2.7)$$

defines the magnetic critical isotherm exponent δ . Definitions of some of the exponents relating to this study are given in table 2.1 [20]. Also listed for the purpose of comparison are predictions from some of the theoretical models as well as the experimental results obtained for typical magnetic systems.

A question can be asked legitimately regarding the amount of attention focused on these critical exponents rather than the complete form of the state function $F(x)$ itself. The answer has three different aspects: Firstly, sufficiently close to the critical point, the behaviour of the leading term dominates, therefore the critical exponent can be easily obtained from experimental data by measuring the asymptotic slope of the double-log plot of $F(x)$ vs. x , while the complete function may be more complicated and hard to quantify; secondly, due to the inherent limitations of present theoretical approaches, accurate predictions of the detailed critical behaviour for comparison with experimental results are still not possible while the critical exponents are readily available, and thus can act as a bridge between theorists and experimentalists; thirdly, despite the substantial variance of the critical temperature from system to system, the rather limited distribution of critical exponents found experimentally have encouraged

Table 2.1: Summary of Critical Exponents

Critical Exponents	γ	γ'	β	δ
Definition	$\chi \propto t^{-\gamma}$	$\chi \propto (-t)^{-\gamma'}$	$M \propto (-t)^\beta$	$M \propto H^{1/\delta}$
Quantity	Zero field isothermal susceptibility	Zero field isothermal susceptibility	Zero field magnetization	Critical isotherm
Conditions	$H = 0$ $T > T_c$	$H = 0$ $T < T_c$	$H = 0$ $T < T_c$	$H \geq 0$ $T = T_c$
Mean Field Theory	1	1	0.5	3
2d Ising	1.75	1.75	0.125	15
3d Ising	1.238	1.25	0.326	4.78
3d Heisenberg	1.388	—	0.367	4.78
3d Spherical	2	—	0.5	5
Experimental Result	1.2 ~ 1.4	—	0.2 ~ 0.4	3 ~ 6

the search for some underlying universality.

A number of theoretical models have been proposed, among them are “classical” theories such as molecular field theory and Landau theory, which give the same predictions for each of the exponents. Scaling theory establishes a theoretical foundation for the critical exponents and also revealed unexpected relations and dependences between them. Ising model, Heisenberg model and several other models have taken into account the direct interactions between magnetic moments in various ways although these can all be regarded as special cases of and unified under the generalized Heisenberg model.

2.3 Scaling Theory

2.3.1 The Basic Assumption in Scaling Theory

Theoretical studies on critical exponents have had basically two objectives: one is to derive the numerical values of the critical indices for various models in order to understand the relevance of model assumptions to the features of critical phenomena;

another objective is to understand how these exponents interrelate with each other.

The scaling approach has been particularly successful in its application to this latter point.

The basic assumption of this approach is that in a magnetic system, the thermodynamic Gibbs potential $G(H, t)$, which has two variables H (external field) and t (reduced temperature), is a generalized homogeneous function (see Appendix A). Consequently we have for the Gibbs potential (using equation A.7)

$$G(\lambda^q H, \lambda^p t) = \lambda G(H, t) \quad (2.8)$$

for any value of the constant λ . This infers that the Gibbs potential has a scale-

independent form, with scale (size) changes by the constant λ factored into the arguments. Consequently, other thermodynamic functions such as internal energy U , Helmholtz free energy F and enthalpy H are also, in general, homogeneous. It showed that the two independent parameters p and q are not specified but rather are determined by details of the particular system of interest. The task of scaling theory is to derive the relationship between the critical exponents and the two scaling parameters and also among the critical exponents themselves.

2.3.2 Scaling Predictions

For a magnetic system, the Gibbs potential is a convenient state function for the derivation of magnetic quantities. From thermodynamics, the magnetization $M(H, t)$ is given by the first derivative of the Gibbs potential with respect to the field

$$M(H, t) = - \left[\frac{\partial G(H, t)}{\partial H} \right]_t \quad (2.9)$$

The behaviour of M under some special conditions, namely $H = 0$ or $t = 0$ respectively, can be deduced with a few additional steps.

Differentiating equation (2.8) with respect to field H gives

$$\lambda \frac{\partial G(H, t)}{\partial H} = \lambda^q \frac{\partial G(\lambda^q H, \lambda^p t)}{\partial (\lambda^q H)} \quad (2.10)$$

i.e.

$$M(H, t) = \lambda^{q-1} M(\lambda^q H, \lambda^p t) \quad (2.11)$$

which is the general form for magnetization. It is obvious that M is also a generalized homogeneous function.

At the critical temperature where $T = T_c$, so that $t = 0$, the above equation becomes

$$M(H, 0) = \lambda^{q-1} M(\lambda^q H, 0) \quad (2.12)$$

Since λ is arbitrary, we are free to choose λ so that $\lambda^q H = 1$ and thus $\lambda = H^{-1/q}$; substituting this into (2.12) yields

$$M(H, 0) = H^{(1-q)/q} M(1, 0) \propto H^{(1-q)/q} \quad (2.13)$$

and a comparison with $M \sim H^{1/\delta}$ then gives

$$\delta = \frac{q}{1-q} \quad (2.14)$$

Similarly, in zero field $H = 0$, and letting $\lambda^p(-t) = 1$, (the minus sign is to give a positive argument for $T < T_c$, also indicating the magnetization is non-zero below T_c) so that

$$M(0, t) = (-t)^{(1-q)/p} M(0, -1) \sim (-t)^{(1-q)/p} \quad (2.15)$$

we obtain

$$\beta = \frac{1-q}{p} \quad (2.16)$$

Now consider the isothermal susceptibility, given by the second derivative of Gibbs energy with respect to the field

$$\chi(H, t) = -\frac{\partial^2 G(H, t)}{\partial H^2} \quad (2.17)$$

which combining with $M(H, t) = -\left(\frac{\partial G}{\partial H}\right)_t$ so that

$$\chi = -\frac{\partial^2 G}{\partial H^2} = \frac{\partial M}{\partial H} \quad (2.18)$$

and differentiating equation (2.11) with respect to H ,

$$\frac{\partial M(H, t)}{\partial H} = \lambda^{2q-1} \frac{\partial M(\lambda^q H, \lambda^p t)}{\partial(\lambda^q H)} \quad (2.19)$$

yields (from the definition of susceptibility χ in (2.18))

$$\chi(H, t) = \lambda^{2q-1} \chi(\lambda^q H, \lambda^p t) \quad (2.20)$$

and setting $H = 0$ and $\lambda^p t = 1$ gives

$$\chi(0, t) = t^{(1-2q)/p} \chi(0, 1) \quad (2.21)$$

which comparing to $\chi \sim t^{-\gamma}$, leads to

$$\gamma = \frac{2q - 1}{p} \quad (2.22)$$

The exponent γ is defined when the critical point is approached from above T_c . Conversely, if $T < T_c$, we consider $H = 0$ and $\lambda^p(-t) = 1$

$$\chi(0, t) = \left(-\frac{1}{t}\right)^{(2q-1)/p} \chi(0, 1) \propto (-t)^{(1-2q)/p} \quad (2.23)$$

comparing with $\chi \sim (-t)^{-\gamma'}$ for $T < T_c$ leads to the relation

$$\gamma' = \frac{2q - 1}{p} \quad (2.24)$$

and we see that $\gamma = \gamma'$; from scaling theory the divergence behaviour of the susceptibility on both sides of T_c are symmetric.

The field dependence of the susceptibility can be expressed in the following manner. Rewriting equation (2.19) gives

$$\chi(H, t) = \lambda^{2q-1} \chi(\lambda^q H, \lambda^p t) \quad (2.25)$$

and setting $\lambda^q H = 1$,

$$\chi(H, t) = H^{(1-2q)/q} \chi(1, H^{-p/q} t) \quad (2.26)$$

or using results obtained before, to substitute for p and q in terms of the exponents δ , γ , β , and denoting $\chi(1, x) = F(x)$ gives

$$\chi(H, t) = H^{1/\delta-1} F\left[\frac{t}{H^{1/(\gamma+\beta)}}\right] \quad (2.27)$$

This result specifies only the argument, while the form of the function $F(x)$ is determined by the specific details of the system.

The general features of the susceptibility can be sketched from (2.23) and (2.27). In static field, a maximum in the susceptibility occurs if

$$\left(\frac{\partial\chi}{\partial t}\right)_H = 0 \quad (2.28)$$

this is satisfied at a temperature t_m , given that

$$\frac{t_m}{H^{1/(\gamma+\beta)}} = c \quad (2.29)$$

where c is a constant. This gives

$$t_m \propto H^{1/(\gamma+\beta)} \quad (2.30)$$

so F is a constant and (2.27) becomes

$$\chi_m(H, t_m) \propto H^{1/\delta-1} \quad (2.31)$$

Thus the scaling theory predicts that the susceptibility is maximized at a reduced temperature t_m which increases with increasing field along the so-called cross-over line described by (2.30), while the peak susceptibility is suppressed by the static field according to the power law given by (2.31). A plot of peak susceptibility against the field on a double logarithmic scale should yield a straight line, the slope of which then yields the δ exponent. The determination of the cross-over exponent, however, is dependent on the choice of T_c . Calculations from the effective field model reproduces the same results, as shown in fig. 2.1. These power relations have been verified to be consistent with experimental results to a high precision, for instance, in PdNi alloys [5] and FeZr glasses [3]. Figure 2.2(a) is the family of curves of the susceptibility $\chi(h, t)$

measured as a function of temperature in different applied fields for FeZr glasses in the vicinity of the ferromagnetic ordering temperature T_c . In fig. 2.2(b),(c) are shown the relationship of χ_m and t_m against H_i , displaying the power relations.

Now combining (2.14), (2.16), (2.22) gives

$$\gamma = \beta(\delta - 1) \quad (2.32)$$

the so-called Widom equality. It is apparent that only two out of the three static critical indices are independent. This is the inevitable consequence of the scaling assumption and not related to the details of the specific system considered. The Widom equality is, however, a special case of a more general inequality

$$\gamma \geq \beta(\delta - 1) \quad (2.33)$$

It can be shown, in a manner similar to that used above, that transport properties such as magnetoresistance and the SRA (Spontaneous Resistance Anisotropy) [5] also obey similar power law relations, with exponents depending only on p and q . As a corollary, the primed and unprimed exponents for the same quantity defined above and below the critical point are always equal in the scaling approach.

To summarize, scaling theory predicts that the system will obey the following power law relations

$$\chi_m \propto H^{1/\delta-1} \quad (H \neq 0, T > T_c) \quad (2.34)$$

$$t_m \propto H^{1/(\gamma+\beta)} \quad (H \neq 0, T > T_c) \quad (2.35)$$

$$\chi(0, t) \propto t^{-\gamma} \quad (H = 0, T > T_c) \quad (2.36)$$

Fundamental to the scaling theory is that all the results are based on just two scaling parameters, namely p and q , which is apparent throughout this brief discussion.

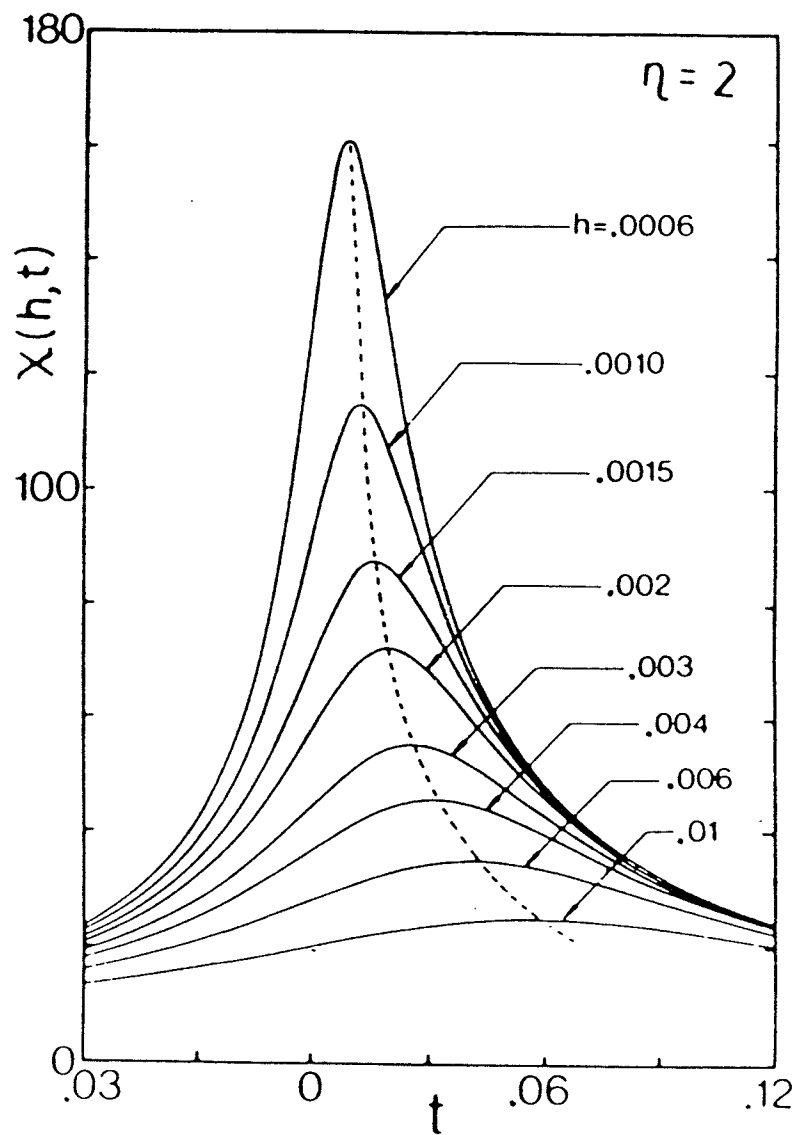


Figure 2.1: Theoretical evidence of the scaling theory: Calculation from the effective field model for $\eta = 2$

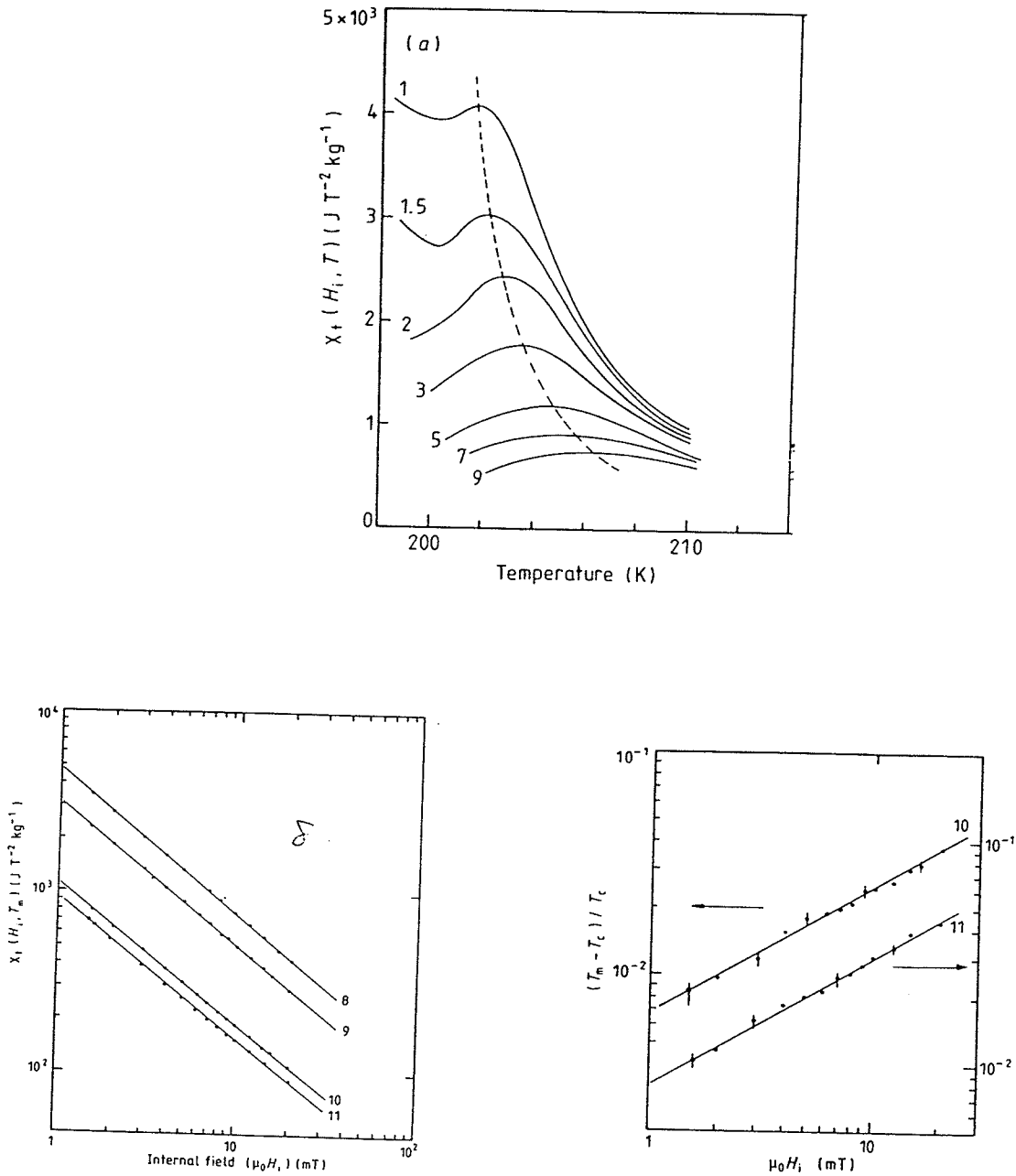


Figure 2.2: Experimental evidence of the scaling theory: Power law behaviour exhibited in amorphous alloy FeZr. After Ma (1991). (a) The susceptibility $\chi(h, t)$ in various static biasing fields. (b) Peak susceptibility plotted against internal field, agree with $\chi_m \sim H_i^{1/\delta-1}$. (c) Reduced temperature plotted against internal field, agree with $t_m \sim H_i^{1/(\gamma+\beta)}$

Their values are intrinsic to the particular system and consequently not provided by the scaling theory itself. This has its origin in the fact that only two variables, H and t , enter into the Gibbs potential with no further constraints (e.g. the detailed type and strength of the interactions) included other than the homogeneity. Thus this approach is less specific to details than most other theories. It should be noted that the homogeneity is an unproven assumption, but the predictions are supported by numerous experimental studies.

2.4 Mean Field Theory

The experimental study of ferromagnetism was pioneered by Pierre Curie about one century ago. He discovered that for a ferromagnet there exists a characteristic temperature T_c , now known as the Curie temperature, above which the ferromagnetism is lost, but retrievable upon subsequent cooling. He also showed that for $T > T_c$ the material is paramagnetic and the susceptibility is inversely proportional to the temperature

$$\chi = \frac{c}{T} \quad (2.37)$$

which is called Curie's law [22], where c is the Curie constant. Later experiments found that not all paramagnetic materials obey Curie's law, some of them can be fitted by a more generalized form

$$\chi = \frac{c}{T - \theta} \quad (2.38)$$

where θ is a constant called the paramagnetic Curie temperature that in many cases is equal or close to the Curie temperature T_c (more accurately referred to as the ferromagnetic Curie temperature). This equation is known as the Curie-Weiss law¹.

¹The Curie-Weiss law is, in fact, a special case of eqn. 2.36 when γ coincides with mean-field prediction and found in some ferromagnet materials.

In order to explain this phenomena Pierre Weiss proposed a phenomenological theory of ferromagnetism called the “Mean Field Theory” (MFT), also referred to as “Molecular Field Theory”, based primarily upon Van der Waals’ theory of non-ideal gases, by drawing an analogy between the interactions prevalent in these two distinct systems.

2.4.1 The Molecular Field

The main postulate of the mean field theory is that the interactions in magnetic materials — of known or unknown origins — may be considered to be equivalent to a single effective internal molecular field H_m proportional to the spontaneous magnetization M , i.e.

$$H_m = \alpha M \quad (2.39)$$

where α is the molecular field constant. The equivalent internal binding field H_m in some very common magnets is of an order of 10^7 Oe, which is much larger than any applied field normally available in the laboratory, indicating the strong exchange coupling that exists between magnetic moments in ferromagnetic materials. The total magnetic field H experienced by a magnetic moment in the presence of an applied field H_a is then the summation of the applied external and the molecular field

$$H = H_i + \alpha M \quad (2.40)$$

H is the effective field, and H_i is the applied field corrected for demagnetization (section 5.1.4).

2.4.2 The Non-interacting Magnetic System

Suppose a system consists of N non-interacting magnetic moments, each with a magnitude $\mu = -g\mu_B\mathbf{J}$ (\mathbf{J} is the angular momentum). In the presence of an external

magnetic field \mathbf{H} , the Hamiltonian is

$$\mathcal{H} = \sum_{i=1}^N \boldsymbol{\mu} \cdot \mathbf{H} \quad (2.41)$$

In the following derivation of magnetization, we assume that all atoms, characterized by total angular momentum quantum number J , occupy the ground state. When an external field is applied to the system, each atom has a quantum number M_J , and the corresponding total angular momentum is $M_J g \mu_B$ in the direction of the field where g is the gyromagnetic ratio. The energy of the magnetic moment in a field is $\varepsilon = -M_J g \mu_B H_a$, and the probability that a particular state M_J is filled is described by the Boltzmann distribution.

According to statistical mechanics, the average magnetization is

$$M = \langle M_z \rangle = N \frac{\sum_{-J}^J M_J g \mu_B e^{-M_J g \mu_B H_a / k_B T}}{\sum_{-J}^J e^{-M_J g \mu_B H_a / k_B T}} \quad (2.42)$$

where N is the number of atoms per unit volume, and μ_B , k_B are the conventional physical constants, the Bohr magneton $\mu_B = e\hbar/(2mc)$ and the Boltzmann constant, respectively.

After some detailed calculation, the result obtained is

$$M(T, H) = N g \mu_B J B_J(x) = M_0 B_J(x) \quad (2.43)$$

where $M_0 = M(T = 0, H_a = 0) = N g \mu_B J$ is the maximum value of the magnetization and B_J is the Brillouin function

$$B_J(x) = \frac{2J+1}{2J} \coth \frac{2J+1}{2J} x - \frac{1}{2J} \coth \frac{x}{2J} \quad (2.44)$$

where

$$x = \frac{J g \mu_B H_a}{k_B T} \quad (2.45)$$

If the system consists of Ising spins with $J = S = 1/2$, then

$$B_{1/2}(x) = \frac{e^x - e^{-x}}{e^x + e^{-x}} = \tanh(x) \quad (2.46)$$

In the case when $J = \infty$, $B_\infty = \coth x$.

The Brillouin function gives the thermodynamic predictions of the reduced magnetization as a function of temperature and field. Figure 2.3 shows plots of the predicted reduced magnetization corresponding to several different J values.

2.4.3 The Interacting Magnetic System

From the calculation for the non-interacting system it is apparent that $M = 0$ when $H = 0$, as illustrated in figure 2.3, which means the spontaneous magnetization is zero. However, interaction-free systems do not exist, and the molecular field must be taken into account. The procedure to be followed for this calculation is identical to the previous one, and all the derivations remain valid except that the molecular field is incorporated by using the effective field of equation (2.40), therefore

$$x = \frac{Jg\mu_B(H_a + \alpha M)}{k_B T} \quad (2.47)$$

consider the applied field is zero, $H_a = 0$, and the equation $M = M_0 B_J(x)$ becomes

$$M = M_0 B_J \left(\frac{Jg\mu_B \alpha M}{k_B T} \right) \quad (2.48)$$

this is an implicit equation of M . The value of M can be determined graphically as illustrated in fig. 2.4. In this figure, $M(J)/M(0)$ and $B_J(bM)$ (where $b = Jg\mu_B \alpha / k_B T$) are plotted against M , and clearly the intersections represent the possible solutions. The zero magnetization is always a solution, but the non-trivial solution corresponds only to non-zero x . To see this, let $x \rightarrow 0$, the Brillouin function $B_J(x)$ becomes

$$B_J(x) = \frac{J+1}{3J} x - \frac{J+1}{3J} \cdot \frac{2J^2 + 2J + 1}{30J^2} x^3 \quad (2.49)$$

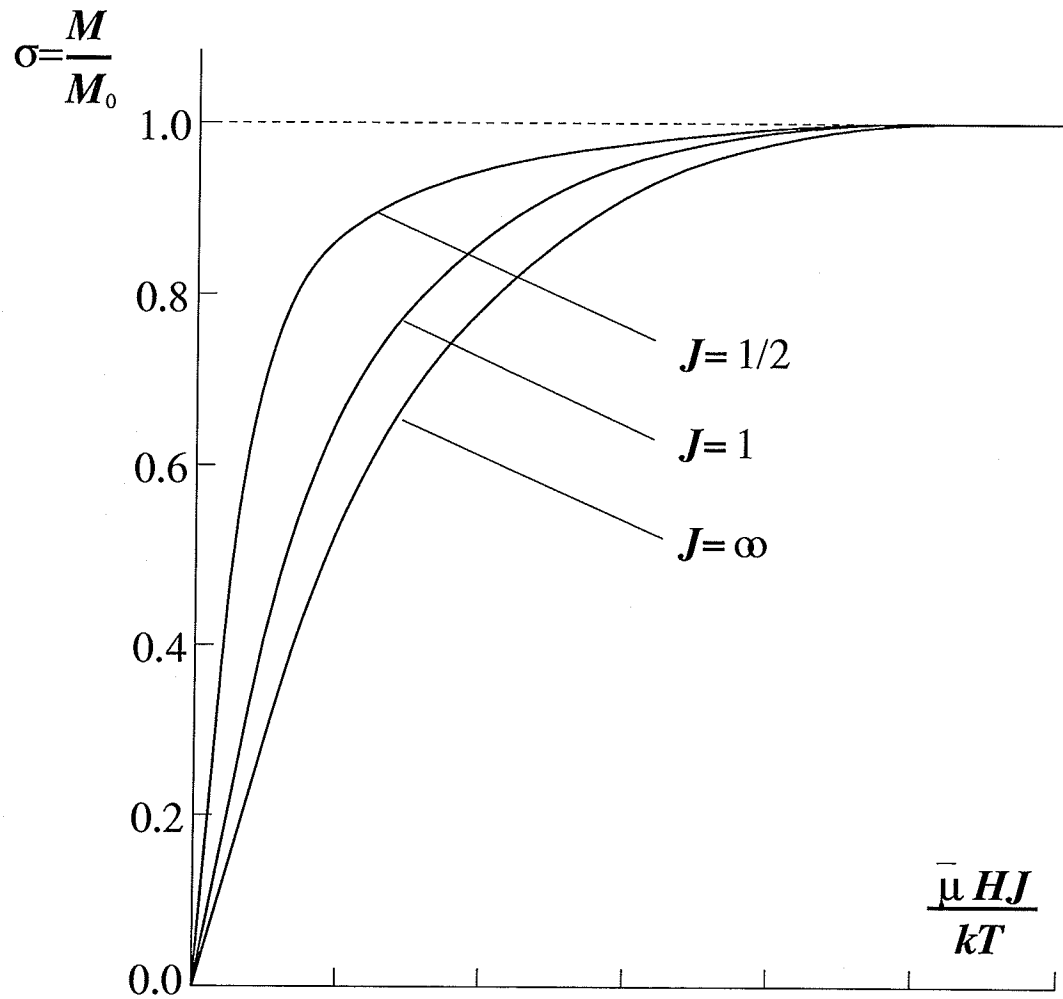


Figure 2.3: Dependence of the reduced magnetization, i.e. the Brillouin function upon x for different J values

thus obtain

$$T = \frac{\alpha N g^2 \mu_B^2 J(J+1)}{3k_B} = C \quad (2.50)$$

Hence we can conclude that the critical temperature predicted by MFT is $T_c = C$, where C is given by equation (2.50). For $T > T_c$, there is no spontaneous magnetization, and the material is paramagnetic; while $T < T_c$, ferromagnetic order sets in and $M(T)$ approaches the saturation magnetization when the temperature is lowered towards zero. The fact that T_c is proportional to the interaction strength α is reasonable since the stronger the correlation between moments, the more stable the ferromagnetic binding and thus higher the transition temperature. When $\alpha = 0$, this recovers the result for the non-interacting paramagnetic system.

2.4.4 Critical Exponents in MFT

Mean field theory was one of the earliest theories that predicted numerical values for the set of critical exponents. Although these results are not very consistent with experiments, they do reflect the right order of magnitude, which in itself is quite an achievement for such a simple theory. Suppose $g\mu_B H/k_B T \ll 1$ which is normally satisfied when T is near the Curie temperature T_c ; equation (2.43) may then be expanded as follows

$$M = a_1 \frac{H}{T} - a_3 \left(\frac{H}{T}\right)^3 + a_5 \left(\frac{H}{T}\right)^5 + \dots \quad (2.51)$$

Where the numbers a_1 , a_2 and a_3 are coefficients with proper units. Substituting the mean field expression for H (2.40) into the above equation gives

$$M = a_1 \frac{H_a + \alpha M}{T} - a_3 \left(\frac{H_a + \alpha M}{T}\right)^3 + \dots \quad (2.52)$$

For temperature above the Curie point, the spontaneous magnetization is zero, and the induced magnetization is of the same order as H_a and thus considered small.

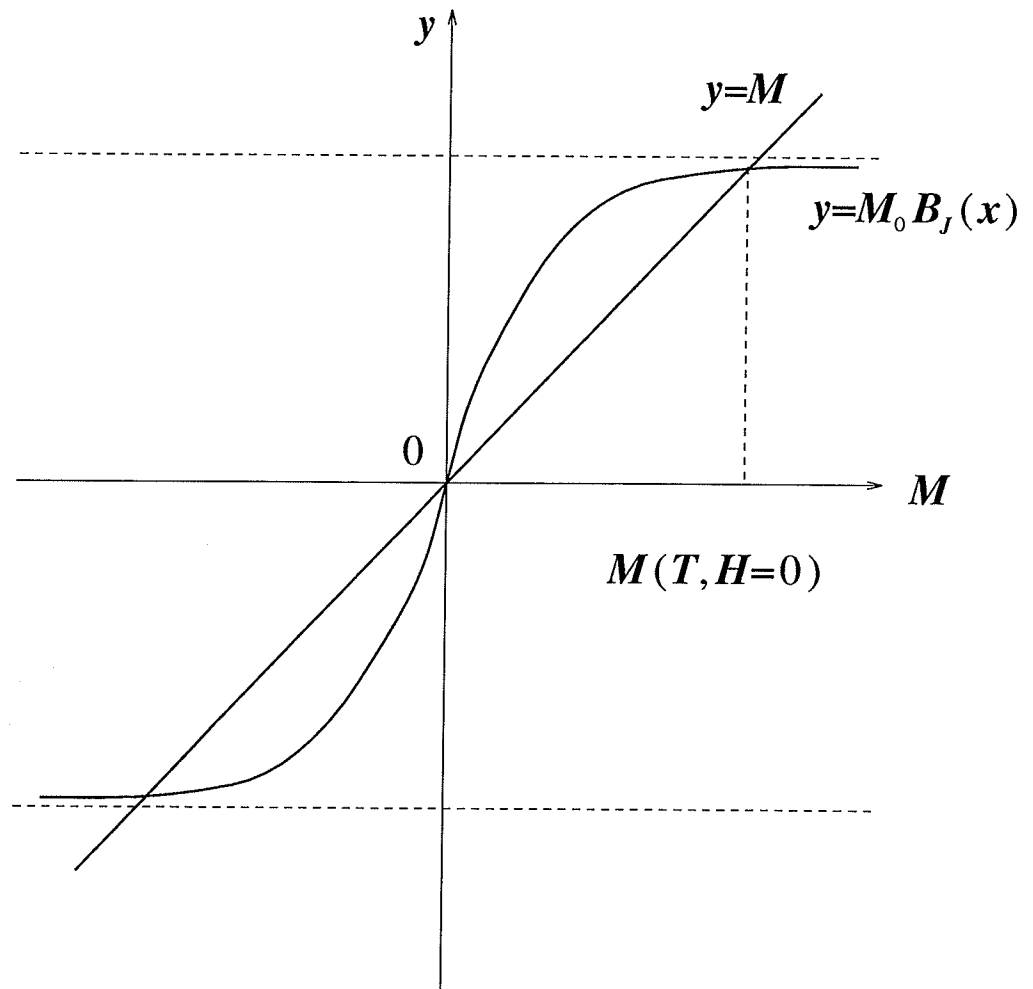


Figure 2.4: Graphic solution to eqn. (2.48) to solve for M

Dropping the third-order term in (2.52), and rearranging yields

$$M \cdot \left(\frac{T - a_1 \cdot \alpha}{T} \right) = \frac{H_a}{T} \quad (2.53)$$

so that

$$\chi = \frac{M}{H_a} \sim (T - a_1 \cdot \alpha)^{-1} \quad (2.54)$$

thus deriving the Curie-Weiss law (2.38). Setting $a_1 \cdot \alpha = T_c$, its physical meaning being the Curie critical temperature, and since $t = (T - T_c)/T_c$, eqn. (2.54) becomes

$$\chi(0, t) \sim t^{-1} \quad (2.55)$$

In small applied field, when $T = T_c = a_1 \cdot \alpha$, and using (2.52) yields

$$M = a_1 \frac{H_a}{T_c} + M - a_3 \left(\frac{H_a}{T_c} + \frac{M}{a_1} \right)^3 \quad (2.56)$$

so that

$$M(H, t = 0) \sim H_a^{1/3} \quad (2.57)$$

and when $H_a = 0$, and again starting with (2.52) yields

$$M = \frac{T_c}{T} M - a_3 \left(\frac{T_c}{a_1 T} M \right)^3 \quad (2.58)$$

from which one obtains

$$M^2 \sim \left(\frac{T_c}{T} \right)^2 \left(\frac{T_c - T}{T_c} \right) \quad (2.59)$$

i.e.

$$M(H = 0, t) \sim t^{1/2} \quad (2.60)$$

Comparing equations (2.55), (2.60) and (2.57) with equations (2.1), (2.1) and (2.3), derives the critical exponent predictions from mean field theory

$$\gamma = 1.0 \quad \beta = 0.5 \quad \delta = 3.0 \quad (2.61)$$

and the Widom equality $\gamma = \beta(\delta - 1)$ is evidently satisfied.

2.4.5 Comments on MFT

As one of the pioneering theories on ferromagnetism, MFT was a tremendous success, accounting not only for the basic properties of ferromagnetism at all temperatures not too close to T_c , but also predicting critical exponents that differ amazingly little from experimental results. It must also be recognized, however, that due to its very simple and crude assumption about the effective field, this theory fails to reflect experimental facts in several aspects:

(1) In the derivation of magnetization M from statistical mechanics the magnetic moments are assumed to be free particles described by Boltzman distribution, while in real magnetic systems interaction is omnipresent, and varying in type, range and strength. In MFT, the interaction between moments is treated in too simple a way to be realistic: the uniform effective field is essentially an infinite range interaction in which each moment experiences exactly the same interaction with all its neighbours; this is certainly not true in dilute magnetic systems, particularly with materials possessing considerable anisotropy.

(2) MFT treats magnetic systems without any considerations of either dimensionality or lattice structure. Although real systems are mostly three dimensional for which the bulk concept is applicable, there exist two-dimensional systems such as thin films.

(3) MFT completely ignores the existence of short range magnetic ordering above T_c as well as statistical fluctuation in the state functions from their thermal equilibrium values (correlations) in the vicinity of T_c .

In view of the above facts, such a "universal" model does not suffice for all systems/conditions. A detailed discussion of more realistic models would be desirable.

The Ising and Heisenberg models are intended to simulate such systems in a more realistic manner, although in their usual forms they deal only with points (1) and (2), leaving the very important point (3) to other methods — renormalization group approach, Landau theory, Pade approximation, etc..

2.5 Interacting Many-particle Systems: the Generalized Heisenberg Model

It is suggested by Stanley [20] that the Hamiltonian of a magnetic many-particle interacting system can be comprehensively expressed as

$$\mathcal{H}^{(D)} = - \sum_{i < j}^N J_{ij,n} \mathbf{S}_i^{(D)} \cdot \mathbf{S}_j^{(D)} \quad (2.62)$$

where the superscript (D) stands for the dimensionality of the spin space, the spin $\mathbf{S}_i^{(D)}$ is a D -dimensional unit vector satisfying the normalization condition $\sum_{n=1}^D S_{in}^2 = 1$ (for $1 \leq i \leq N$), in which $(S_{i1}, S_{i2}, \dots, S_{iD})$ are the Cartesian coordinates of $\mathbf{S}_i^{(D)}$; $J_{ij,n}$ denotes the effective pair-wise exchange interaction between spins located at site i and j in the n th Cartesian direction which can vary both in magnitude and sign. The minus sign is to indicate that the lower energy state (by convention $J_{ij,n}$ is positive for the parallel configuration of \mathbf{S}_i and \mathbf{S}_j) is favoured, and the summation is over all sites in the system. A large variety of specific models can be discussed in the framework of this Hamiltonian.

2.5.1 The Exchange Interaction

In a most straightforward simplification of equation (2.62), we assume that the pair-wise exchange interaction, $J_{ij,n}$, is independent of the subscripts, i.e. $J_{ij,n} = J$ for any i, j and n , and vanishes if sites i and j are not nearest neighbours, so that it can

be taken out of the summation; then the Hamiltonian is reduced to

$$\mathcal{H}^{(D)} = -J \sum_{\langle i < j \rangle}^N \mathbf{S}_i^{(D)} \cdot \mathbf{S}_j^{(D)} \quad (2.63)$$

In general, the exchange $J_{ij,n}$ can assume a distribution of various forms to simulate a wide range of types of specific interaction configurations, e.g. the usually studied near-neighbour exchange, a Gaussian distribution simulating bond disorder (S-K model) and infinite range (mean field) interactions (Stanley, 1971).

(1) Non-nearest-neighbour Interaction

In the previous section we assumed two spins interact only when they are immediate neighbours on the lattice. A modification of this is to allow the range of the interaction to extend beyond the nearest-neighbours to include the second, third nearest-neighbours and up to infinite range. Exact solutions are not available for this type of calculation but numerical calculations for the Ising model have shown that the critical exponents start to deviate from nearest neighbour results only when the exchange interaction is extended over a long range. In the limit of infinite range, the result approaches mean field (infinite range) predictions.

(2) Non-uniform Interactions

Another more sophisticated consideration of the interaction is to modify the unrealistic assumption of a uniform $J_{ij,n}$ by one that is dependent on sites i and j but independent of n . The critical behaviour of the cases $D = 1$ and $d = 1$ (linear chain) and $d = 2$ (square lattice) for Ising model with arbitrary positive coupling $J_{i,i+1}$ showed no dependence on the choice of J .

(3) Anisotropic Interaction

The subscript n in equation (2.62) denotes a Cartesian coordinate in a spin space of dimension D . As determined by the symmetry group of the lattice structure, J_n may,

in fact, represent an anisotropic interaction. Numerical studies of Jasnow and Wortis on the anisotropic classical Heisenberg model ($D = 3$) have found that the critical point exponents jump discontinuously from $D = 3$ values as soon as the slightest amount of anisotropy occurs.

2.5.2 Ising Model, $D=1$

The simplest version of equation (2.63) is when $D = 1$, thus corresponds to the so-called Ising model. The spins are reduced to one-dimensional vectors capable of only two orientations, up(+) and down(-), and a spin of $S = \pm 1$ is assigned to each of the N sites of the lattice; thus the Hamiltonian (in the presence of external field H) becomes

$$\mathcal{H} = -J \sum_{i < j}^N S_i S_j + \sum_i^N H_i S_i \quad (2.64)$$

Based on Ising's calculation for one-dimensional (linear chain) nearest neighbour exchange bonds, this model does not show ferromagnetic behaviour at finite temperature as expected. The ground state at absolute zero is ferromagnetically ordered with all spins parallel, but this long range order collapses for any finite positive temperature and is taken over by a paramagnetic state.

Although the work on the one-dimensional Ising model was not very encouraging, Peierls recognized that the two or three dimensional cases do give rise to a ferromagnetic ground state and a phase transition is predicted by Onsager's exact solution for the thermodynamic properties of the two-dimensional (2D) Ising model in the absence of an external field. Despite these encouraging successes, prospects of obtaining solutions of the 2D Ising model with the external field, as well as the 3D model, remains uncertain.

2.5.3 Classical Heisenberg Model, $D=3$

The case of three-dimensional spins in equation (2.62) corresponds to the Heisenberg model. It allows the spins to assume arbitrary orientations like a vector in the physical space, and can be considered as the ($S \rightarrow \infty$) classical limit of the quantum mechanical Heisenberg model. The Hamiltonian written in the component form, is

$$\mathcal{H} = - \sum_{i < j} J_{ij} (S_{ix} S_{jx} + S_{iy} S_{jy} + S_{iz} S_{jz}) \quad (2.65)$$

Phenomenally more sophisticated than the Ising model, the 3D Heisenberg model is also analytically unsolvable and various approximation methods have been devised. As the interactions will affect the alignment of the spin moments, a physically appealing approach is to replace the interactions by an effective field whose properties are determined by consistency with the spin orientations.

2.5.4 Other Dimensions

The case when $D = 2$ results in the planer Heisenberg model. This Hamiltonian describes a system of mutually coupled two-dimensional unit spins. It has been considered to be a lattice model for the superfluid transition in a Bose fluid. If $D > 3$, there is no physical system that can actually be described by this Hamiltonian, but the case when $D \rightarrow \infty$ is analytically soluble.

It can be seen that equation (2.62) is very versatile, being able to incorporate a wide range of exchange interaction types into different lattice structures and spin dimensions, thus with some caution in the form of equation (2.62) selected, it can represent some real physical systems fairly well. However, because inherent in its notation is the spin at lattice sites the spins are implicitly assumed to be both ordered and well localized. This is clearly not the case for the random distributions of spins

found in dilute magnetic alloys.

2.6 S-K Model, Exchange Bond Disorder

Primarily based on the Ising model, Sherrington and Kirkpatrick [6] examined a spatially random spin system with infinite range interactions. By assuming the translational invariance of the spin sites and transforming space (site) disorder into exchange bond disorder, they analyzed a model in which the spins are coupled by interactions J_{ij} distributed with a Gaussian probability given by

$$P(J_{ij}) = \frac{1}{J\sqrt{2\pi}} e^{-\frac{(J_{ij}-J_0)^2}{2J^2}} \quad (2.66)$$

here J_0 and J are the first and second moments of this distribution, and are scaled so that they are intensive quantities

$$J_0 = \tilde{J}_0/N, \quad J = \tilde{J}/N^{1/2} \quad (2.67)$$

Calculating the free energy yields a set of simultaneous equations

$$m = \frac{1}{\sqrt{2\pi}} \int dz e^{-z^2/2} \tanh \left(\frac{\sqrt{q}\tilde{J}}{kT} z + \frac{m\tilde{J}_0}{kT} \right) \quad (2.68)$$

$$q = 1 - \frac{1}{\sqrt{2\pi}} \int dz e^{-z^2/2} \text{sech}^2 \left(\frac{\sqrt{q}\tilde{J}}{kT} z + \frac{m\tilde{J}_0}{kT} \right) \quad (2.69)$$

The physical significance of the parameters m and q can be interpreted as

$$m = \langle \langle S_i \rangle \rangle_J \quad (2.70)$$

$$q = \langle \langle S_i^2 \rangle \rangle_J \quad (2.71)$$

where $\langle S_i \rangle$ represents the thermal average of the spin at site i , and $\langle \rangle_J$ represents the average over the exchange distribution. The quantities m and q function as order

parameters for characterising magnetic states. A nonzero q indicates the existence of a magnetic order, while a nonzero m indicates that the order is ferromagnetic. When both m and q are zero, there is no magnetic order and the state is paramagnetic; when $q \neq 0$ and $m = 0$, the state is called a spin-glass. These relations are illustrated in figure 2.5.

Solving the coupled equations numerically results in the phase diagram, shown in figure 2.6 with axes in terms of the dimensionless quantities kT/\tilde{J} and \tilde{J}_0/\tilde{J} . As expected, if kT is greater than \tilde{J}_0 and \tilde{J} , the thermal excitation exceeds the ordering interaction and paramagnetism results. When kT is reduced below the greater of \tilde{J}_0 or \tilde{J} , magnetic ordering occurs. If $\tilde{J}_0/\tilde{J} < 1$, the ordering is spin-glass, while if $\tilde{J}_0/\tilde{J} > 1$, the ferromagnetic state ensues.

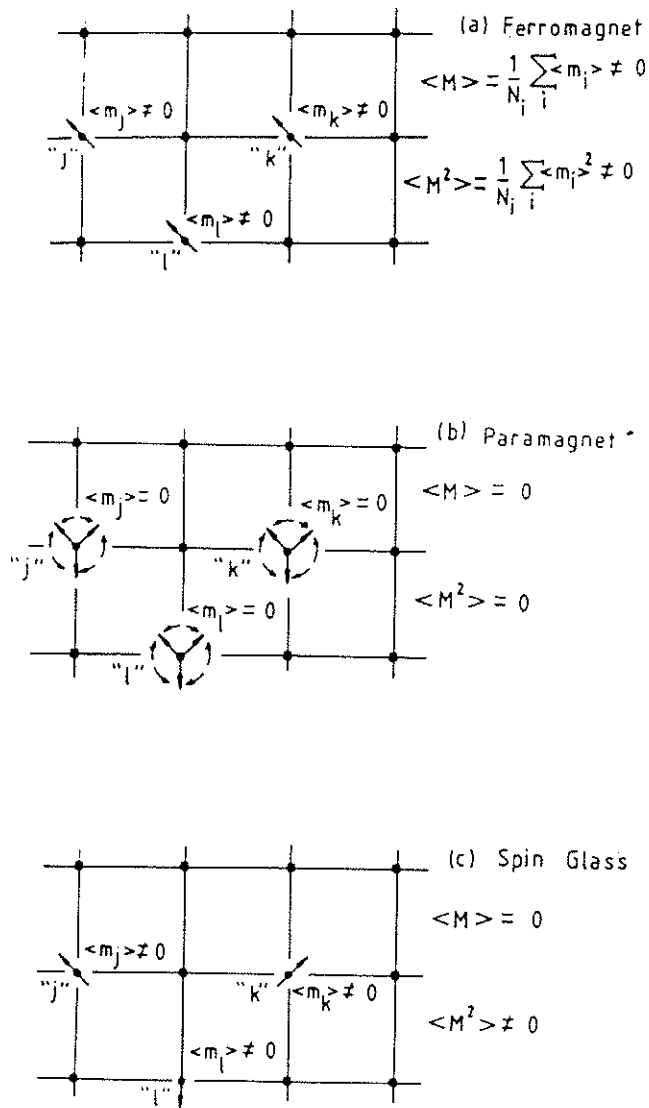


Figure 2.5: the order parameters m and q

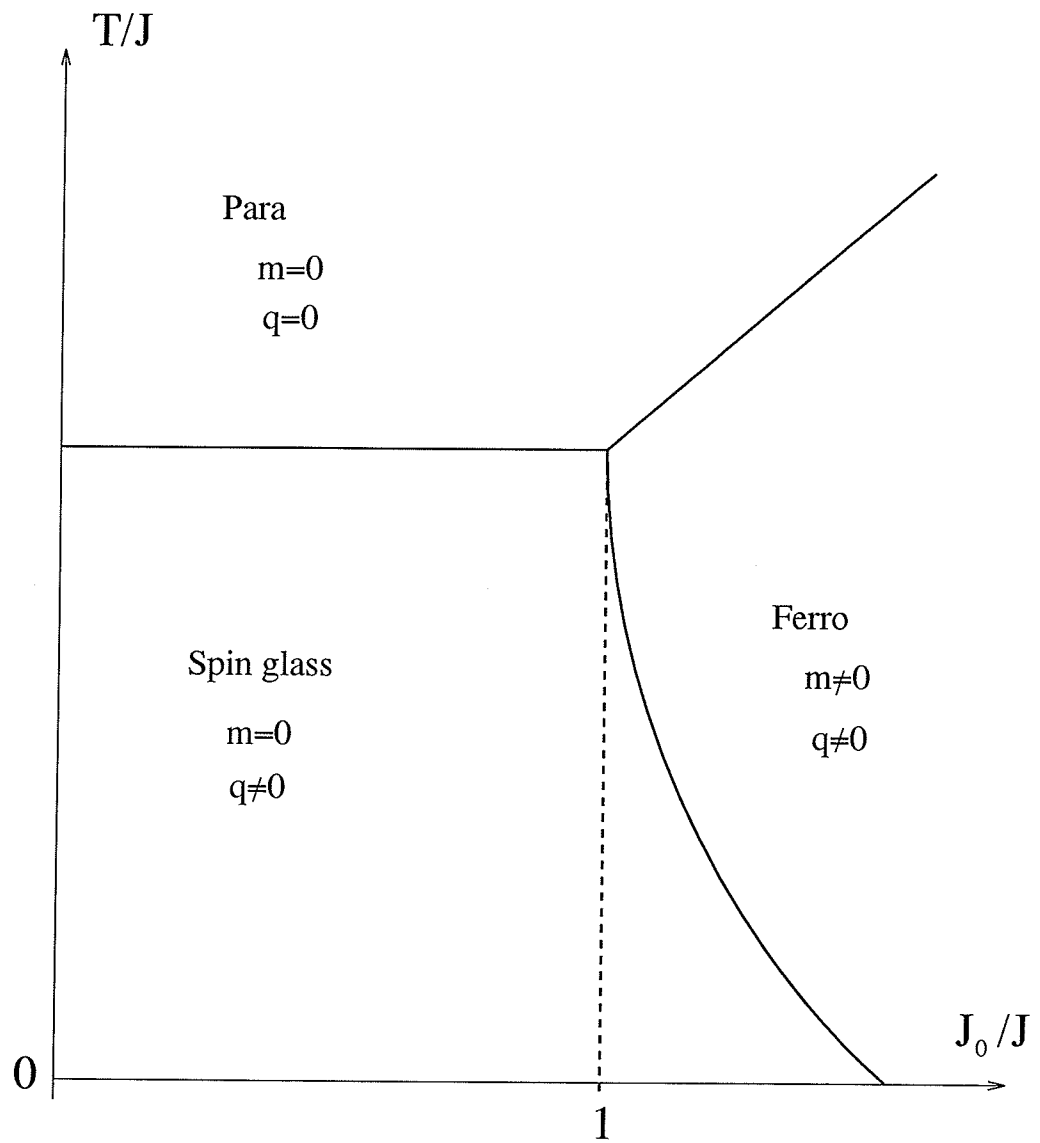


Figure 2.6: S-K model phase diagram

Chapter 3

The RFe_2 Series of Compounds

Among the binary intermetallic compounds containing magnetic transition metals, the series of Laves phase compounds denoted RFe_2 [9], where R is a $3d$ (Sc, Ti), $4d$ (Zr, Nb, Y) or $5d$ (Hf) transition metal, an actinide (U) or a rare earth element, have attracted much attention due to the various types of magnetic order that occurs with the different R elements. The uncoupled (conduction) d electrons, through R-R and/or R-Fe interactions, give rise to the magnetic moment in these compounds. In the hexagonal Laves phase (C14) structure, $ScFe_2$ exhibits ferromagnetic, $TiFe_2$ antiferromagnetic and $NbFe_2$ shows various ferromagnetic and antiferromagnetic behaviour in various temperature regions. On the other hand, the iron compounds where R is either an actinide (U) or a rare earth element have cubic Laves phase (C15) structure and are well known for their interesting magnetic and magnetostrictive properties. In addition, alloying effects in these compounds have revealed more interesting magnetic behaviour in the rare earth compounds, such as a spin glass or a reentrant phase.

Table 3.1 lists the saturation moment μ and the ferromagnetic Curie temperature T_c for the series of RFe_2 compounds where R is a rare earth element.

Table 3.1: Magnetic Properties of Rare-Earth-Iron Compounds

Compound	$\mu(\mu_B)$	$T_c(K)$
CeFe ₂	2.38 - 2.59	221 - 240
SmFe ₂	2.50 - 2.8	676 - 700
GdFe ₂	2.8 - 3.75	785 - 810
TbFe ₂	3.68 - 5.8	696 - 711
DyFe ₂	4.9 - 7.31	633 - 638
HoFe ₂	5.1 - 6.67	597 - 614
ErFe ₂	4.75 - 5.85	590 - 595
TmFe ₂	2.52 - 2.7	566 - 610
YbFe ₂	1.8 - 2.3	
LuFe ₂	2.70 - 2.97	558 - 610
YFe ₂	2.78 - 3.1	535 - 554

3.1 CeFe₂

Cerium [23] in rare earth family has been of particular interest because of its dual valence of either 3 or 4 originating from its variable electronic structure: the energy of the inner $4f$ level and that of the outer $5d$ valence electrons are nearly the same, therefore a transition between these two energy levels is likely to take place. As a consequence, cerium is one of the most reactive element of the rare-earth metals.

Among the series of RFe₂ compounds, ferromagnetic CeFe₂ [7] has been given considerable attention due to its significantly lower magnetic moment per Fe atom ($1.2\mu_B$) as well as ordering temperature ($T_c = 227K$), compared to other compounds in this series with values typically of $3.4\mu_B$ and $600K$, respectively (see Table 3.1). Ferromagnetic order in CeFe₂ covers a wide range from the critical temperature T_c down to helium temperature. Kunkel *et al* [7] have performed detailed measurements on this compound using the method of the a. c. magnetic susceptibility. Figure 3.1(a) shows the temperature dependence of the a. c. susceptibility in zero biasing field.

The graph indicates a rapid increase in the susceptibility as the sample is cooled from the paramagnetic region at high temperature towards the ferromagnetic ordering temperature T_c . The susceptibility then drops abruptly after reaching a maximum at the Hopkinson peak, forming a sharp peak at a temperature slightly lower than T_c . This is followed by a relatively moderate decrease of susceptibility until helium temperature, which is evidence of strong ferromagnetic correlation of the material. At low temperature region between $20 \sim 60K$ there is shown an anomaly in the form of a small plateau. This is assumed to be a precursor to the inherent instability of this system.

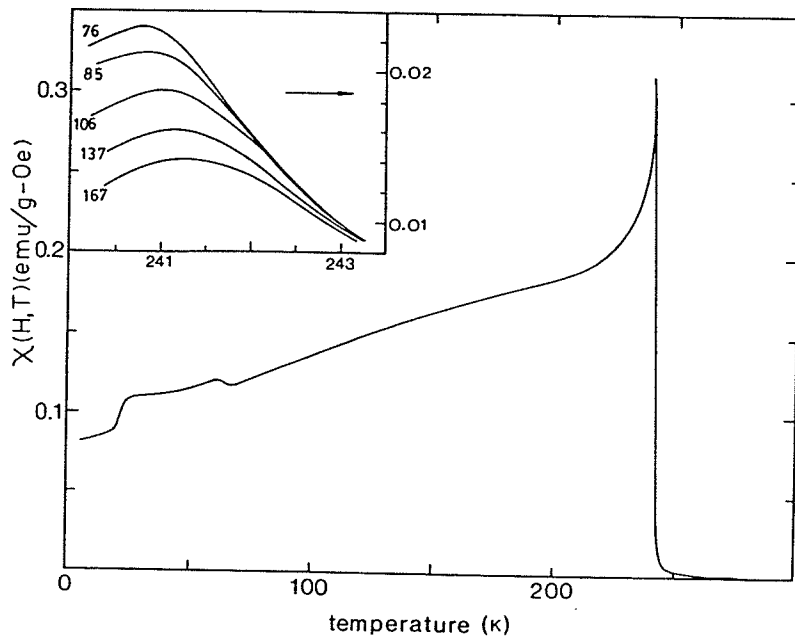
Figure 3.1(b) is a plot of the effective Kouvel-Fisher susceptibility exponent $\gamma^*(t)$ [26], defined by

$$\gamma^*(t) = \frac{d \ln[\chi(0, t)]}{d(\ln t)} \quad (3.1)$$

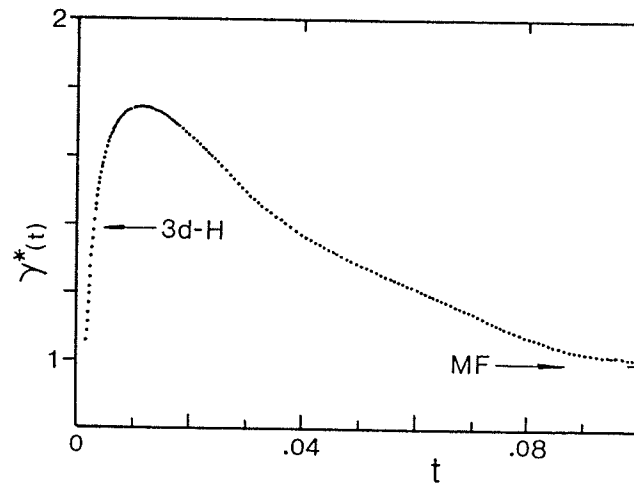
against reduced temperature. With increasing reduced temperature t , $\gamma^*(t)$ increases rapidly to a maximum value 2.0 before decreasing asymptotically towards the mean field value of 1. This non-monotonic variation, which in itself is in disagreement with both mean field and Heisenberg model predictions where γ is simply a constant, is thought to be a characteristic of systems with considerable exchange bond disorder.

As observed in other ferromagnetic systems, when subjected to an external magnetic field, the Hopkinson peak will decrease rapidly in amplitude and will shift towards lower temperature. This enables the observation of a secondary peak to be made and its change with increasing fields to be studied, as shown in the inset of fig. 3.1(a). The peak height and the peak temperature obey the scaling law (section 2.3.2)

$$\chi_m(H_i, t_m) \propto H_i^{1/\delta-1} \quad (3.2)$$



(a)



(b)

Figure 3.1: (a) Temperature dependence of zero field susceptibility of CeFe_2 . The inset shows the susceptibility in d. c. biasing fields near the transition temperature. The numbers marked against each curve indicates the corresponding field in Oersted. (b) Kouvel-Fisher exponent $\gamma^*(t)$ plotted against reduced temperature.

$$t_m = \frac{T_m - T_c}{T_c} \propto H_i^{1/(\gamma+\beta)} \quad (3.3)$$

The exponent δ , obtained from a double-logarithmic plot of peak susceptibility vs. internal field in fig. 3.2(a) is estimated to be $\delta = 3.0 \pm 0.15$, which is close to the mean field value. The inability to resolve critical peaks in low fields is interpreted as an indication of the presence of considerable anisotropy effects and magnetic coercivity as these effects prevent the regular contribution to the response from saturating in low fields. The plot of t_m vs. H_i , again on a double-log scale, in fig. 3.2(b), showed good linearity but the cross-over exponent $(\gamma + \beta)$ obtained is unable to distinguish between mean field and three dimensional Heisenberg predictions, due to uncertainties introduced ultimately by anisotropy effects resulting from spin-orbit coupling.

While the Hopkinson region is confirmed to host a paramagnetic to ferromagnetic transition around $T_c = 240K$, the low temperature anomalies have been investigated through a study of the nonlinear response in the field dependent susceptibility which represent the critical/divergent contributions to the total susceptibility at a pure ferromagnetic-spin-glass transition. Similar studies for such candidate re-entrant systems as PdFeMn have shown an anomalous peak in the non-linear response in the low temperature region, strongly suggestive of a reentrant transition to a spin-glass phase. No such anomaly was observed for pure CeFe₂ however.

The study of CeFe₂ is also made especially interesting since its ferromagnetic state is unstable, as confirmed by small levels of substitution for Fe by a variety of elements. It is reported by various authors [8] [15] that a small amount of substitution for Fe by Ru, Co, Al, etc., effectively suppresses the magnetic response and narrows the ferromagnetic region; thus an abrupt drop in magnetic response in the low temperature region which is not observed in the pure CeFe₂ susceptibility measurements

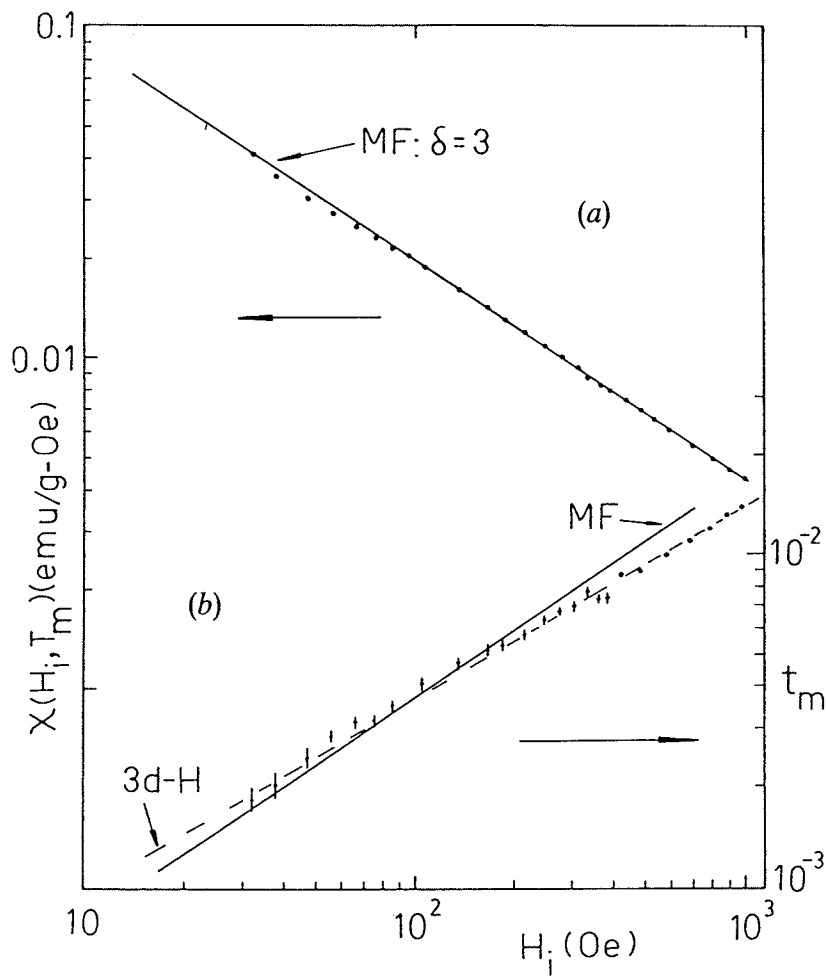


Figure 3.2: (a) Peak susceptibility plotted against the internal field on a double-log scale, correspond to $\delta = 3.0$. (b) The reduced peak temperature plotted against the internal field on a double-log scale. The solid and dashed line represent the mean field predictions and 3D-Heisenberg predictions, respectively.

appears in these pseudobinary intermetallic compounds, which is believed to be an indication of a phase transition of some kind. While the upper transition is agreed to be from paramagnetic to ferromagnetic with decreasing temperature, this second magnetic phase transition at lower temperature has been of both experimental and theoretical controversy. The question that arises is what type of ground state does the system assume with these substitutions, antiferromagnetism and spin-glass being possible candidate states. Measurements using a number of different experimental techniques have shed some light on the ordering in this type of system.

3.2 $\text{Ce}(\text{Fe}_{1-x}\text{Al}_x)_2$

Aluminum is a non-magnetic metal. The polycrystalline alloys $\text{Ce}(\text{Fe}_{1-x}\text{Al}_x)_2$ have been intensively studied due to its sensitivity to small levels of Al substitution at the Fe site. Upon the background of the ferromagnetism of the parent compound CeFe_2 , $\text{Ce}(\text{Fe}_{1-x}\text{Al}_x)_2$ undergoes a new transition at $T_f < T_c$, below which the ferromagnetic ordering no longer exists.

As a possible structure of the low temperature state almost every magnetic state known has been proposed at one time or another. Nishihara *et al* [11] concluded it to be a first order phase transition from the antiferromagnetic to ferromagnetic state at 100K (for $x = 0.05$) based on magnetization and Mössbauer measurements. Magnetostriction measurements by Kido *et al* [12] showed a discontinuous increase in unit cell volume in the low temperature regime which was concluded to be a metamagnetic transition from an antiferromagnetic to ferromagnetic state, in agreement with Nishihara, and attributed to lattice distortion. Later work of Eynon and Ali [13] using resistivity, a. c. susceptibility, magnetisation and thermal expansion techniques over a broad temperature range of $4 \sim 290\text{K}$, however, gave a different result. They

concluded that the low temperature phase was the result of spin-glass freezing and that the transition is NOT of first order, which is in contradiction with the conclusion of Nishihara *et al.* A recent study by Yang *et al* [14] using small-angle neutron scattering on samples with Al concentration of $x = 0, 0.06$ and 0.14 has examined the state both above and below T_f and asserted that the low temperature phase is ferrimagnetic in origin, and the feature of the phase transitions qualitatively relies on Al concentration.

3.3 $\text{Ce}(\text{Fe}_{1-x}\text{Co}_x)_2$

Another compound of interest in the CeFe_2 family is $\text{Ce}(\text{Fe}_{1-x}\text{Co}_x)_2$ because of the following significant feature of CeCo_2 . Although Co itself is magnetic, the compound CeCo_2 , unlike CeFe_2 , does not show magnetic order. This makes $\text{Ce}(\text{Fe}_{1-x}\text{Co}_x)_2$ an appropriate system for the study of how the randomly distributed moments interact and magnetically order.

Various experimental methods yield a general understanding concerning a double transition from paramagnetic–ferromagnetic–antiferromagnetic for the entire concentration range $0 < x < 0.3$. Ali and Zhang [15] reported, on the alloy $\text{Ce}(\text{Fe}_{0.8}\text{Co}_{0.2})_2$, measurements of the magnetization as function of temperature and applied field, as well as temperature dependent a. c. susceptibility, electrical resistivity and thermal expansion measurements. The susceptibility behaviour is similar to that with 4% Al substitution ($x = 0.04$), except that the dropoff is much steeper. An $H - T$ phase diagram determined the low temperature phase to be antiferromagnetic, and the transition is of first order. Study of structural effects [16] in the vicinity of the lower transition attributed the transition to a distortion of the lattice and a resulting discontinuity in the temperature dependence of the cell volume. This long range an-

tiferromagnetic order is also confirmed by neutron diffraction measurements. These alternative methods study different aspects of the magnetic behaviour of these pseudobinary alloys thus improving the understanding of the associated thermodynamic properties, the interaction mechanism involved and the band and lattice structure.

3.4 $\text{Ce}(\text{Fe}_{1-x}\text{Ru}_x)_2$

A. C. susceptibility measurements on CeFe_2 with Ru substitutes at the Fe site were initiated by Roy and Coles [8] [9] on compositions of $x = 0.02, 0.04, 0.06$ and subsequently on additional samples with x ranging from 0.01 to 0.15; figure 3.3 summarizes their results. For small values of x (~ 0.01), the susceptibility essentially retains the features of pure CeFe_2 , but a change in the slope of the dropoff at low temperature sets in above $x = 0.03$, resembling that in $\text{Ce}(\text{Fe}_{1-x}\text{Al}_x)_2$ at a composition of $x = 0.03$. With increasing Ru concentration, the slope of the dropoff of χ vs. T at the low temperature edge becomes increasingly steep and its position T_f shifts in the high temperature direction, indicating very drastic canting of spins. This low temperature phase has been identified as antiferromagnetic by recent neutron diffraction studies by Kennedy *et al* [10]. Also with increasing Ru concentration, T_c decreases, making the plateau region narrower. This trend persists until the concentration reaches 0.09, at which point the peak susceptibility drops drastically and the curve shape becomes distinct from that for lower x values, and T_c cannot be defined.

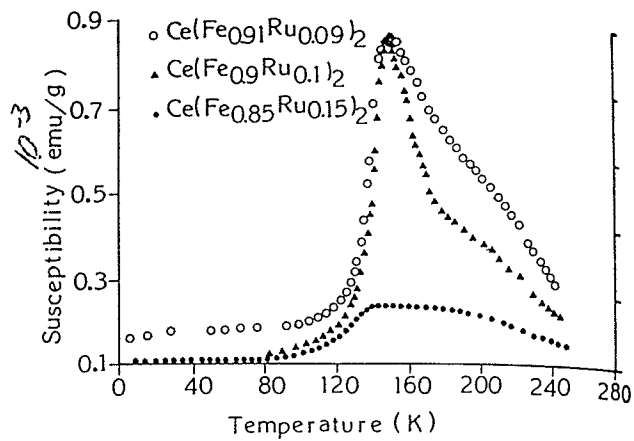
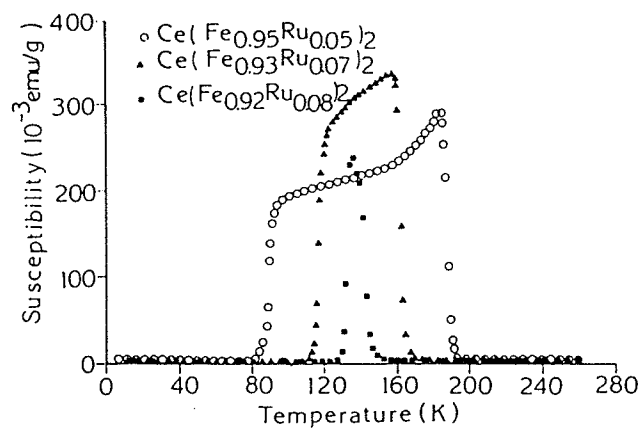
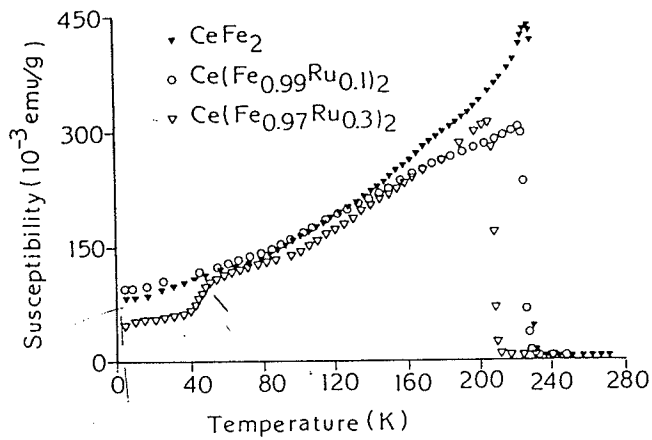


Figure 3.3: Effect of substitution of Ru for Fe in CeFe_2 alloy

Chapter 4

Experimental Methods

Detailed measurements of the temperature and external field dependent a. c. magnetic susceptibility have been carried out on two samples: $\text{Ce}(\text{Fe}_{0.93}\text{Ru}_{0.07})_2$ and $\text{Ce}(\text{Fe}_{0.92}\text{Ru}_{0.08})_2$. This chapter gives a detailed description of the experimental procedure, including sample preparation and discussions on the apparatus and the experimental techniques used.

4.1 Sample Preparation

The two original samples of $\text{Ce}(\text{Fe}_{1-x}\text{Ru}_x)_2$, with $x = 0.07$ and $x = 0.08$ were obtained from Roy and Coles [8] who prepared the sample by argon arc melting from constituent metals of at least 99.99% purity and chill casting into copper molds to produce rods of approximately square cross-section. In our laboratory the samples were sealed separately in "Vycor" tubes (Vycor is a Corning product which has a high softening temperature of about 1000°C) and annealed in an argon atmosphere following the sequence [9] of 600°C for two days, 700°C for five days, 800°C for two days, 850°C for one day and then cooled down at room temperature. This will enhance the homogeneity and thus improve the quality of the samples. Temperature variance during the annealing was about $\pm 10^\circ\text{C}$; the response time of the furnace ($3 \sim 4$

hrs) in setting the sequence of annealing temperatures must also be considered, but this is relatively short compared to the annealing time of one or more days per step. The samples after annealing were silvery, with obvious evidence of grain growth, thus indicating good heat treatment.

The dimensions (measured by a travelling microscope of type 2152, the Precision Tool and Instrument Company, Surrey, England) and mass (measured by Mettler microbalance) of the rectangular samples after annealing were $(5.09 \times 1.55 \times 1.50)\text{mm}^3$, 94.8mg for $\text{Ce}(\text{Fe}_{0.93}\text{Ru}_{0.07})_2$ and $(5.30 \times 1.59 \times 1.54)\text{mm}^3$, 102.8mg for $\text{Ce}(\text{Fe}_{0.92}\text{Ru}_{0.08})_2$. The dimensions measured was an average of several measurements since the sides of the samples were not perfectly square. The geometry (form factor) of the sample will affect the bulk magnetic properties of the specimen through demagnetization effects (this will be discussed in the next section). Although it is experimentally more desirable to prepare the samples in long, thin strips in order to reduce the demagnetization effect, the brittleness of the samples makes this difficult thus these two samples were prepared using the chill casting technique resulting in the aforementioned rectangular shape. The mass, on the other hand, is quite accurate and reliable, and is required to determine the true intrinsic value of the susceptibility.

For both samples, the alloys are solid solutions where Ru atoms are regarded to randomly substitute for Fe sites in the lattice structure. The density of $\text{Ce}(\text{Fe}_{1-x}\text{Ru}_x)_2$ can be calculated as follows: Considering there are 8 stoichiometric molecules per unit cell, we have

$$\text{Density} = 8 \times \frac{M_{\text{Ce}} + 2 \cdot [(1-x) \cdot M_{\text{Fe}} + x \cdot M_{\text{Ru}}]}{6.023 \times 10^{23} \cdot a^3} \quad (4.1)$$

where a is the lattice constant, M_R denotes the molar weight of element R and x is the atomic concentration of Ru.

From x-ray diffraction measurements [9], $\text{Ce}(\text{Fe}_{1-x}\text{Ru}_x)_2$ alloys are found to maintain the C15 Laves phase structure of the parent compound CeFe_2 with the lattice constant slightly increasing with Ru concentration. For $\text{Ce}(\text{Fe}_{0.93}\text{Ru}_{0.07})_2$ and $\text{Ce}(\text{Fe}_{0.92}\text{Ru}_{0.08})_2$, the lattice constants are given to be $7.315 \pm 0.005 \text{ \AA}$ and $7.320 \pm 0.005 \text{ \AA}$, respectively; thus using the above formula, with the molar weights

$$M_{\text{Ce}} = 140.12 \text{ g/mol}$$

$$M_{\text{Fe}} = 55.85 \text{ g/mol}$$

$$M_{\text{Ru}} = 101.07 \text{ g/mol}$$

the densities are:

$$x = 0.07 \quad \text{Density} = 8.76 \pm 0.02 \text{ g/cm}^3$$

$$x = 0.08 \quad \text{Density} = 8.77 \pm 0.02 \text{ g/cm}^3$$

The densities will be used to determine the demagnetization factor (per unit mass from the per unit volume value calculated, section 5.1.4).

Some of the properties of the two samples are summarized in table 4.1. The calibration factor and the demagnetization factor are explained in section 5.1.3 and section 5.1.4, respectively. Two numbers are listed for the demagnetization factor, with the first one being the demagnetization factor after adjustments (55% reduction) and the values in the parenthesis are results from ellipsoidal calculation.

4.2 Experimental Apparatus

The measurements are carried out with a phase locked susceptometer operational over a wide temperature range. Figure 4.1 is a schematic illustration of the cryostat system which can provide a temperature as low as 1.5 K (with liquid helium). The

Table 4.1: Sample Description

Sample	Ce(Fe _{0.93} Ru _{0.07}) ₂	Ce(Fe _{0.92} Ru _{0.08}) ₂
Dimensions (mm ³)	5.09 × 1.55 × 1.50	5.30 × 1.59 × 1.54
Weight (mg)	94.8	102.8
Density (g/cm ³)	8.76 ± 0.02	8.77 ± 0.02
Lattice Constant (Å)	7.315 ± 0.005	7.320 ± 0.005
Demagnetization factor	4.765 (10.478)	4.692 (10.300)
Calibration factor	0.00054	0.00055

sensing coils are part of the pick-up circuits of the susceptometer, the external field coils provide a static biasing field required in the experiment. Temperature can be increased with the nichrome heater. The whole system is cooled by an external liquid nitrogen dewar.

4.2.1 The susceptometer

The a.c. magnetic susceptibility was measured with a modified linear phase-locked susceptometer [18] consisting of a phase detector, an oscillator, a voltage reactance and two *RCL* circuits. Figure 4.2 is the block diagram of the susceptometer.

A series *RCL* circuit has a resonant frequency of $\omega_0 = 1/\sqrt{LC}$. When it is activated by an external signal with frequency $\omega \neq \omega_0$, the complex voltage \tilde{U} measured over the reactance as compared to the driving signal \tilde{U}_0 is

$$\tilde{U} = \tilde{U}_0 e^{i\phi} \quad (4.2)$$

where

$$\phi = \arctan \frac{\omega L}{R(1 - \omega^2 LC)} \quad (4.3)$$

is the phase difference between input and output signals. At fixed frequencies, the phase shift changes with the component values.

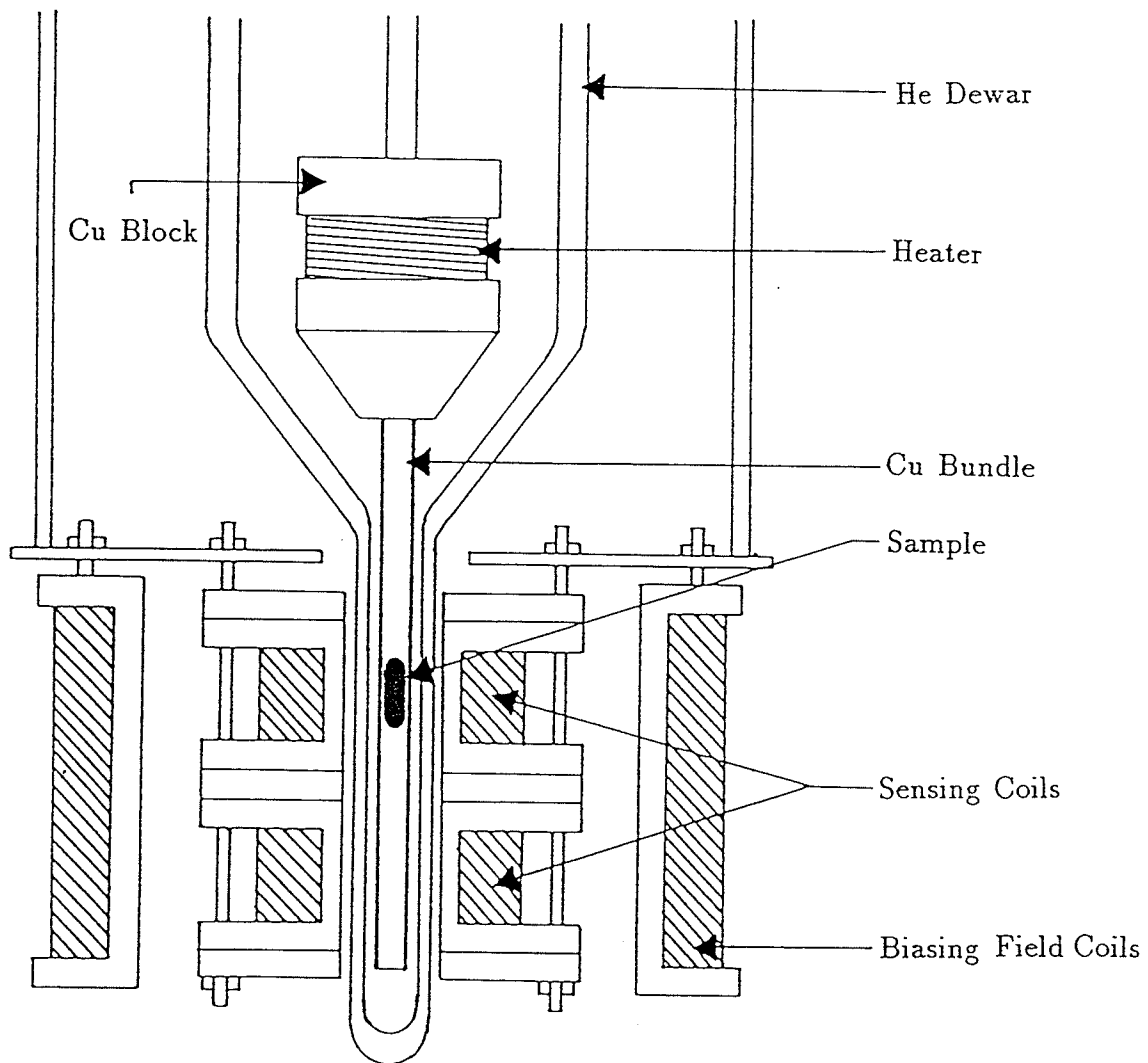


Figure 4.1: The cryostat system

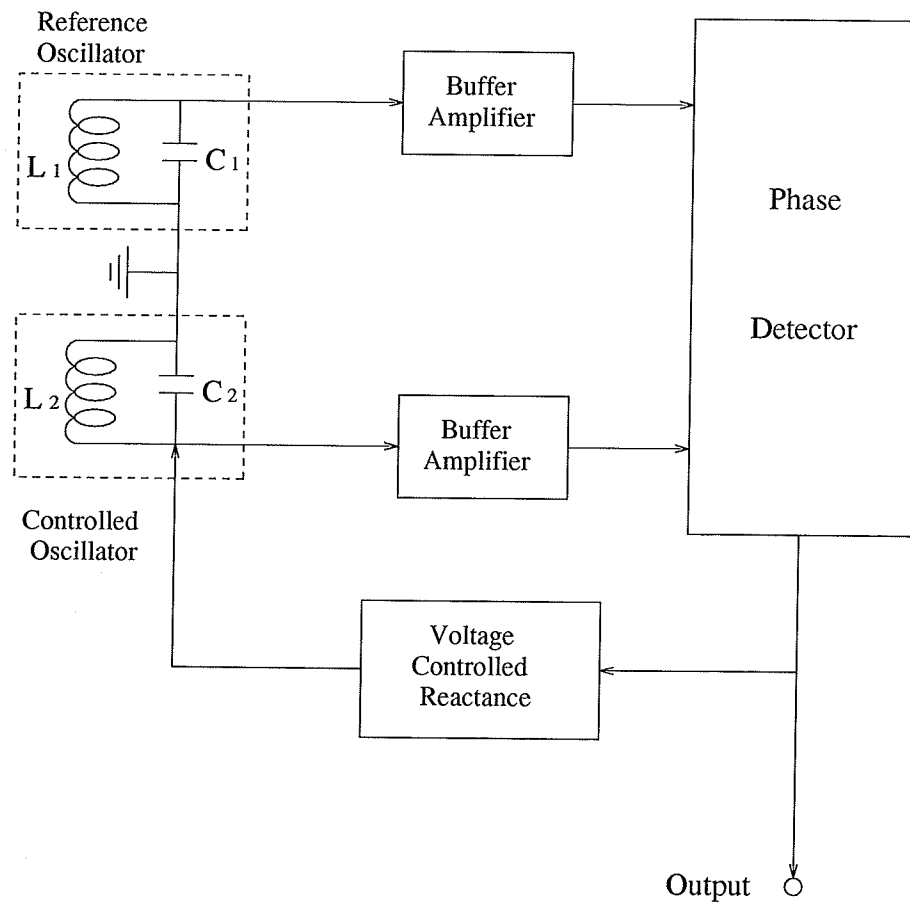


Figure 4.2: Block diagram of the circuit

The detecting system consists of two identical counter-wound coils, both of which are components of separate RCL oscillators. The detecting coils, for increased stability and sensitivity, are mounted in the liquid nitrogen dewar and maintained at $77K$. Each coil is 4000 turns of 35 gauge enamelled copper wire, with inductances of 205mh and 202mh [19], respectively. The two circuits are reference coil and controlled coil, acting as reference (circuit 1) and detection (circuit 2, sensing coil) oscillators, respectively. If the components in the two circuits are not identical, the resonant frequencies may not be the same. Both the signal generated in the reference oscillator (from circuit 1) and the output signal (from circuit 2) are compared in the phase detector; an error signal generated by the phase detector, which is proportional to the phase difference of the two input signals, is used to compensate for the frequency discrepancy by means of a voltage-dependent reactance element in the detection circuit, thus keeping the the effective LC product of the two oscillators the same.

When both coils are empty, the voltage reading reflects the component differences in the two circuits; this offset is called the zero reading. In the experiment, when a magnetic sample is placed in the inductor of circuit 2 and thus changing its inductance, a measure of its effect is given by the corresponding correction voltage needed to adjust the control reactance and bring the LC product back to its original value. The difference between this voltage and the zero reading then gives a signal which is proportional to the magnetic susceptibility of the sample.

The a. c. susceptibility of the sample is measured with a driving field of a frequency of 2400Hz and amplitude¹ of 35 mOe applied parallel to the long axis of the sample. The driving field is continuously variable up to 500 mOe, but for these measurements

¹Changed to 125mOe for the latter part of the experiment for an improved S/N ratio in the measurement, this proved not to result in a change of the susceptibility since the phase detector is only phase sensitive.

was set at 35 mOe which is the smallest setting that allows the oscillator to drive the *RLC* circuits. Time constant and sensitivity of the susceptometer are also adjustable with nominal values of 1 second and $\times 1$, respectively.

4.2.2 Sample Block and Location

The sample is located in a copper wire bundle soft soldered to the OFHC copper block around which the heater wire is wound; this keeps the sample in good thermal contact with the copper bundle and allows it to be heated uniformly and yet allows good penetration of the a.c. driving field of the susceptometer, i.e. the diameter of the wires is much less than the skin depth. The copper bundle and block are attached to a thin-walled stainless steel rod which can be lifted and lowered vertically to allow adjustments of the sample position in the sensing coil. The distance between the sample position and the end of copper block is approximately 8.4 cm. Additional fine adjustments are made using an adjustment screw on the top of the stainless steel rod to maximize the signal. The copper bundle is inserted into the tail section of the inner dewar and also extends through the center of both detecting coils to keep them balanced. The sample is also electrically insulated from the copper wires by wrapping it with a single layer of masking tape.

4.2.3 Biasing Magnetic Field

The static biasing field is supplied by a solenoid mounted coaxially with the detecting system and again maintained at 77K. It consists of two coaxial coils, each wound with 22 gauge enamelled copper wire providing fields of 215 Oe/amp and 186 Oe/amp along the length of the sample, respectively. For zero and low field temperature sweeps, only one solenoid (215 Oe/amp) is used, when a higher field is needed, both are connected

in series so they carry the same current and can generate a field up to 1 KOe at 401 Oe/amp. A Lambda LK344A FM Model current regulated power supply provides a current of moderate stability. Zero field is often needed when cooling the sample from above T_c and in zero field runs; a constant current source provides a preset current of 2.43 mA to back off the local 0.52 Gauss vertical component of the Earth's field. The current is monitored by a DANA multimeter for possible field drifts.

4.2.4 Temperature control

Since the temperature range of interest for the samples is entirely above liquid nitrogen temperature, the sweeps are mostly done from 100K to 200K. Temperature can be controlled by keeping the inner dewar surrounded by liquid nitrogen and warming the sample with the electric heater. The heater can carry a current up to 500 mA, but during data collection a current of 180mA is never exceeded so the sample can be slowly warmed with an average warming rate of 3.5 ~ 4 min/K, this is realized by increasing the heater current in small steps from 80 mA to 150 mA (at 100 K ~ 200 K, heating current increases with sample temperature) and simultaneously pumping the vacuum space of the inner dewar with a diffusion pump through a cold-trap to control the thermal contact to the liquid nitrogen jacket.

Temperature readings are taken using a calibrated Chromel vs. Au+0.03at.%Fe thermocouple with one junction of the thermocouple immersed in an ice bath. Due to the magnetic properties of the Au-Fe in the thermocouple, it is located at the top of the copper bundle to avoid inducing a false signal in the sensor coil and thus is not located at exactly the same point as the sample. Problems arising from a possible difference between the sample temperature and the thermocouple temperature can be minimized by the small heating current, the low warming rate and also the high

thermal conductivity of the copper assembly. Effort is also made to keep the heating current for different runs in same temperature range comparable to add consistency to the overall data.

4.2.5 Data Collection

Data collection was controlled by a computer program referred to as RALPH². RALPH takes readings of thermocouple temperature in microvolts and susceptibility in volts; it also keeps track of the time taken between consecutive readings so that adjustments of heating current can be made accordingly.

Temperature sweeps (temperature dependent susceptibility in applied static biasing fields) are carried out in external fields from zero to 1KOe. The procedure adopted is as follow:

(1) The sample is warmed well above the Curie temperature and then cooled in zero field to a temperature below the Hopkinson peak where the susceptibility has dropped abruptly to near zero. Cooling in zero field over the entire range from above T_c to below T_f (where the magnetic response is negligible) ensures that each measurement begins with the sample in the same magnetic state, so that the measurements are reproducible, which otherwise may not be the case in the presence of considerable magnetic hysteresis.

(2) The current in the solenoid is then adjusted (increase in one direction only to avoid hysteresis effect by driving the sample around minor hysteresis loop) at a constant stabilized temperature to a preset value so that it produces the desired biasing field.

(3) The heater is turned on and the temperature starts to increase.

²Reference written by J. Schachter, U. of Manitoba, 1991.

(4) The data are taken during warming at intervals of every $0.28K$ ($\sim 5\mu V$), this will give sufficient number of data points throughout the temperature range of interest and particularly in the transition regions.

(5) During the temperature sweep, zero readings are taken intermittently for the purpose of correcting the signal for any systematic shift of the zero reading. This is done by using the supporting rod to extract the sample from the pick-up coil, however, with the copper bundle still linking both sensing coils. After a zero reading is taken the sample is lowered back to its original position and normal data collection resumes.

Chapter 5

Data Analysis and Results

5.1 Correction of Data

As mentioned in the previous chapter, the raw data recorded from the susceptometer is proportional to the susceptibility of the sample; however, several steps need to be taken to correct for background and demagnetizing effects as well as the sample mass and susceptometer calibration in order to obtain the true susceptibility, the latter is an intrinsic property of the material, thus permitting these results to be compared with previous works on similar systems. The design of the experiment has taken into account these requirements and provides the necessary means for accomplishing these steps. The zero and background corrections are made with respect to the inherent signals from the apparatus (i.e. with the sample removed), while the calibration (length), normalization (mass) and demagnetizing (geometry) corrections are with respect to the individual samples.

5.1.1 Zero Correction

Due to a small temperature and applied magnetic field dependence, resulting from eddy currents induced within the OFHC copper block and bundle, the zero reading changes, hence the output signal of the susceptometer should be corrected for this

shift in the zero reading. Although ideally one should keep track of the susceptibility signal as well as the zero signal simultaneously, the fact that the sample has to be removed in order to take zeroes makes this impossible. Furthermore, taking too many zero readings is not desirable because it may affect the sample temperature as well as the warming rate which we wish to keep as constant as possible. In any event, the corrected signal should then be the difference between the reading and the corresponding zero. We do the correction by taking 6 ~ 10 zeroes over the range of $100K \sim 200K$ and estimating the zeroes in between these zero points by linear interpolation. More zeroes are taken when the signal level is low, thus making the zero shifts more significant.

5.1.2 Background Correction

The background amounts to a small temperature and applied magnetic field dependent diamagnetic signal due to an imbalance of the diamagnetism of the copper bundle linking both pick-up coils. The background is measured by removing the sample from the bundle and measuring the susceptibility and the corresponding zeroes. The true signal is then the difference between the measured signal and the background detected in the absence of the sample. With a typical magnitude of about $-0.025V$ at $4.2K$, this background, though, vanishes above nitrogen temperature and can be taken as zero in the temperature range where all the present measurements are made.

5.1.3 Calibration and Normalization

The output voltage of the susceptometer after zero and background correction, and after taking into account the mass of the sample (normalization), is proportional to the measured susceptibility with a constant of proportionality referred to as the

calibration factor. The sesquioxide of gadolinium Gd_2O_3 [21] is used as the calibration substance for the susceptometer because of its simple Curie-Weiss behaviour, high value of susceptibility and well-defined moment ($J = 7/2$). Experimental results have shown that within a temperature range of $20\text{K} \sim 300\text{K}$, the susceptibility can be fitted by the Curie-Weiss law within experimental accuracy (better than 0.5% relative and 1% absolute [21]).

$$\chi = \frac{N\mu_{eff}^2}{3k_B(T - \theta)} = \frac{Ng^2\mu_B^2J(J + 1)}{3k_B(T - \theta)} \quad (5.1)$$

where N is the number of Gd atoms per gram, and θ is the paramagnetic Curie temperature which has a value determined by experiments to be -13K [21], and $\mu_{eff} = g\mu_B\sqrt{J(J + 1)}$ is the effective moment.

Samples of 99.999% pure Gd_2O_3 powder are packed into cylindrical glass tubes of various diameters and lengths. The magnetic susceptibility is measured for all these configurations at the liquid nitrogen temperature of 77K ; the ratio of the susceptometer output voltage/gram of the material and the calculated susceptibility is found to be dependent on the length of the powder sample but not on the diameter. Figure 5.1 is the calibration curve thus obtained.

5.1.4 Demagnetization Correction

In the presence of an external magnetic field, a magnetic material is magnetized, and the generation of net uncompensated magnetic poles on the ends give rise to a magnetic field in the sample volume opposing the external field, therefore reducing the effective internal magnetic field; this is called demagnetization and the induced field is the demagnetizing field.

For samples with finite length (along the direction of the applied field), the demagnetizing field, H_d , is determined by the magnetization M in the sample and the

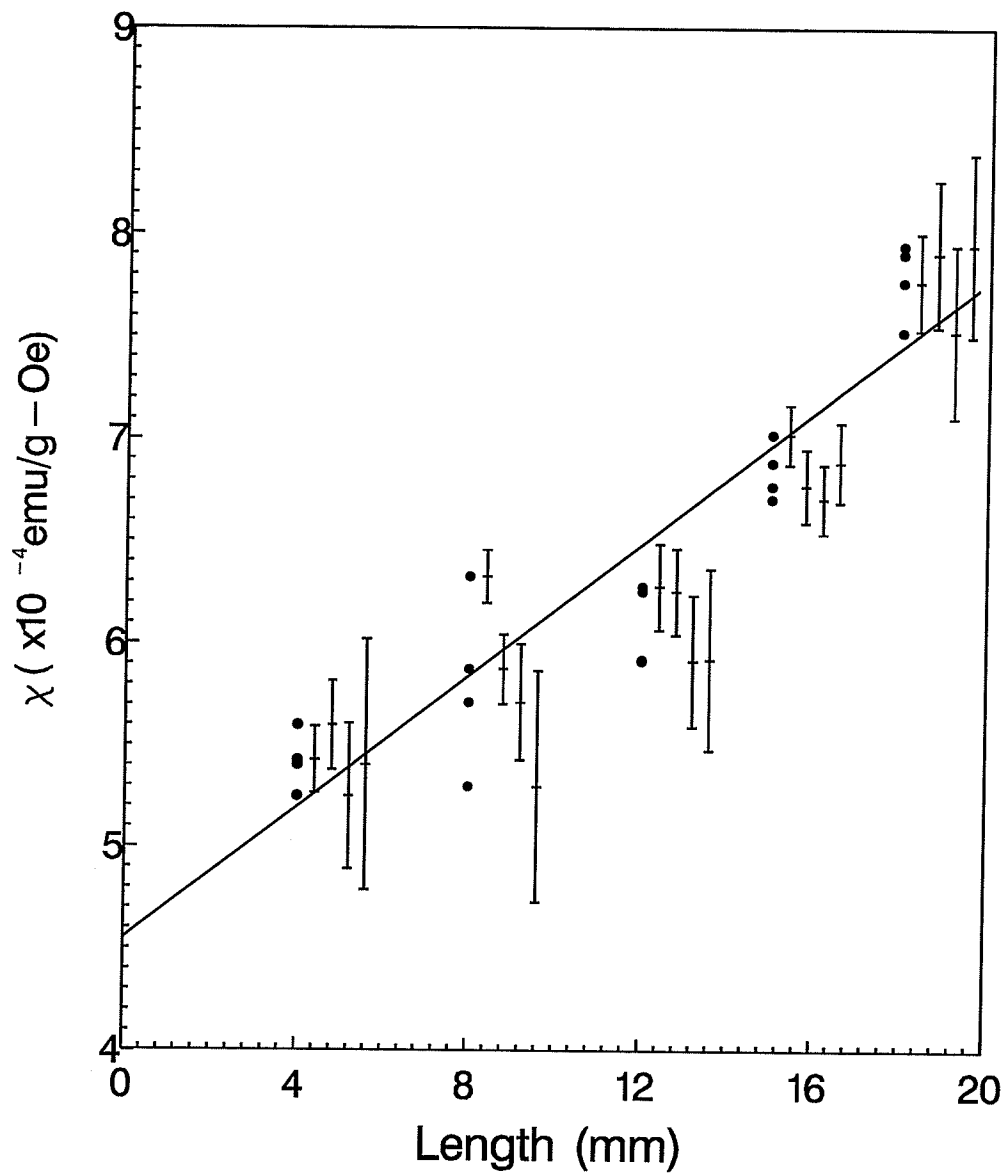


Figure 5.1: Calibration curve for the susceptometer. The errorbars are centered at the data point and offset to the right for clarity. The data points for a given sample length (abscissa) correspond to the four selected sample diameters. To within error there is no dependence of the calibration factor on the diameter of the sample.

demagnetizing factor N , which is dependent solely on the sample geometry; this is given by the expression

$$H_d = N \cdot M \quad (5.2)$$

The resulting effective internal field H_i within the bulk material is thus

$$H_i = H_a - N \cdot M \quad (5.3)$$

where H_a is the applied external field. This internal field varies with position but is uniform in ellipsoids and spheres¹.

The correction for the demagnetizing effect will affect not only the internal field, but also the true susceptibility χ_t , defined as the derivative of the magnetization with respect to the effective internal field, viz.,

$$\chi_t(H, t) = \frac{\partial M(H, t)}{\partial H_i} \quad (5.4)$$

compared to the measured susceptibility, χ_m , which is defined with respect to the applied field,

$$\chi_m = \frac{\partial M(H, t)}{\partial H_a} \quad (5.5)$$

and is the reading obtained from the susceptometer after calibration and normalization. To derive the relation between χ_t and χ_m , one needs only to combine equations (5.3) and (5.4) to give

$$\chi_t = \frac{\chi_m}{1 - N \cdot \chi_m} \quad (5.6)$$

where χ_t is the true susceptibility after the demagnetization correction, its unit being emu/g·Oe.

¹If the length of the material is much larger than the other two dimensions, e.g. a long flat strip, the demagnetization effect is negligible.

In order to obtain the magnetization M , it is necessary to integrate the measured susceptibility, i.e.

$$M = \int_0^{H_a} \chi_m \cdot dH_a \quad (5.7)$$

which is, in fact, equivalent to the integration $M = \int_0^{H_i} \chi_t \cdot dH_i$.

Due to the demagnetizing effect, it is experimentally desirable to make the samples in a shape that has a small demagnetizing factor. This is, unfortunately, not possible in this experiment for the samples $\text{Ce}(\text{Fe}_{0.93}\text{Ru}_{0.07})_2$ and $\text{Ce}(\text{Fe}_{0.92}\text{Ru}_{0.08})_2$, which are too brittle to be made in long strips at the present time, thus larger demagnetizing factors have to be accepted and considered in the analysis.

An exact analytical calculation for N is available only for certain sample shapes, i.e. spheres and ellipsoids; approximations and numerical methods have to be used for samples of general shape. Here, calculations of the demagnetizing factor for the samples of $\text{Ce}(\text{Fe}_{0.93}\text{Ru}_{0.07})_2$ and $\text{Ce}(\text{Fe}_{0.92}\text{Ru}_{0.08})_2$ are made based on the assumption that they are approximately ellipsoidal in shape with principal axes equal to the measured dimensions. In actual fact the irregular shape (approximately rectangular in this case) tends to reduce the demagnetizing effect [22], consequently the calculated result was multiplied by an adjustment factor that was found necessary in previous work with similarly shaped samples, namely for the a. c. susceptibility measurements on CeFe_2 by Kunkel *et al* [7]; the demagnetizing factor was taken to be 2.7 g·Oe/emu, which was 45% of the value obtained from the ellipsoidal calculation. We employed the same adjustment factor for both $\text{Ce}(\text{Fe}_{0.93}\text{Ru}_{0.07})_2$ and $\text{Ce}(\text{Fe}_{0.92}\text{Ru}_{0.08})_2$. Although the absolute reliability of this demagnetizing factor, and thus the susceptibility, is of some uncertainty, the relative accuracy of the susceptibility exceeds 0.1% [24].

5.2 Data Analysis for $\text{Ce}(\text{Fe}_{0.93}\text{Ru}_{0.07})_2$

The a. c. magnetic susceptibility of $\text{Ce}(\text{Fe}_{0.93}\text{Ru}_{0.07})_2$ was measured as a function of temperature in a number of static external biasing fields ranging from zero field (Earth's field backed off) up to 1K Oersted. Fig. 5.2 and fig. 5.3 display the temperature dependence of the a. c. magnetic susceptibility in zero field and in various applied fields, respectively. The application of static biasing fields result in the suppression of the magnetic response as well as the shift of both the Hopkinson and the secondary/critical peaks. The Hopkinson peak (or the principal maximum) and the critical peak (evident near 150K in fields > 200 Oersted in fig. 5.3) have different dependences on the applied field. In zero field and low applied fields, the critical peak is dominated by the Hopkinson peak and thus not resolvable; with increasing field, however, the magnitude of the Hopkinson peak is suppressed much more rapidly than the critical peak², and their peak temperatures shift in opposite directions with increasing field so that they move further apart. This enables the observation of the secondary peak near 150K with the application of sufficiently large external biasing fields, as is apparent in fig. 5.3.

5.2.1 Zero Field Susceptibility

Figure 5.2 shows the susceptibility data of $\text{Ce}(\text{Fe}_{0.93}\text{Ru}_{0.07})_2$ in zero field, i.e. with a small field of approximately 0.52 Gauss applied to back off the vertical component of the Earth's field. Upon cooling from above T_c , the susceptibility increase rapidly near T_c and reaches a maximum at the so-called Hopkinson peak. The susceptibility is then roughly constant until at a temperature T_f it drops steeply to near zero, the

²From the measurements of $\text{Ce}(\text{Fe}_{0.93}\text{Ru}_{0.07})_2$, for instance, $\chi_{\text{Hopkinson}} \sim H^{-2.6}$, while $\chi_{\text{critical}} \sim H^{-0.7}$, approximately.

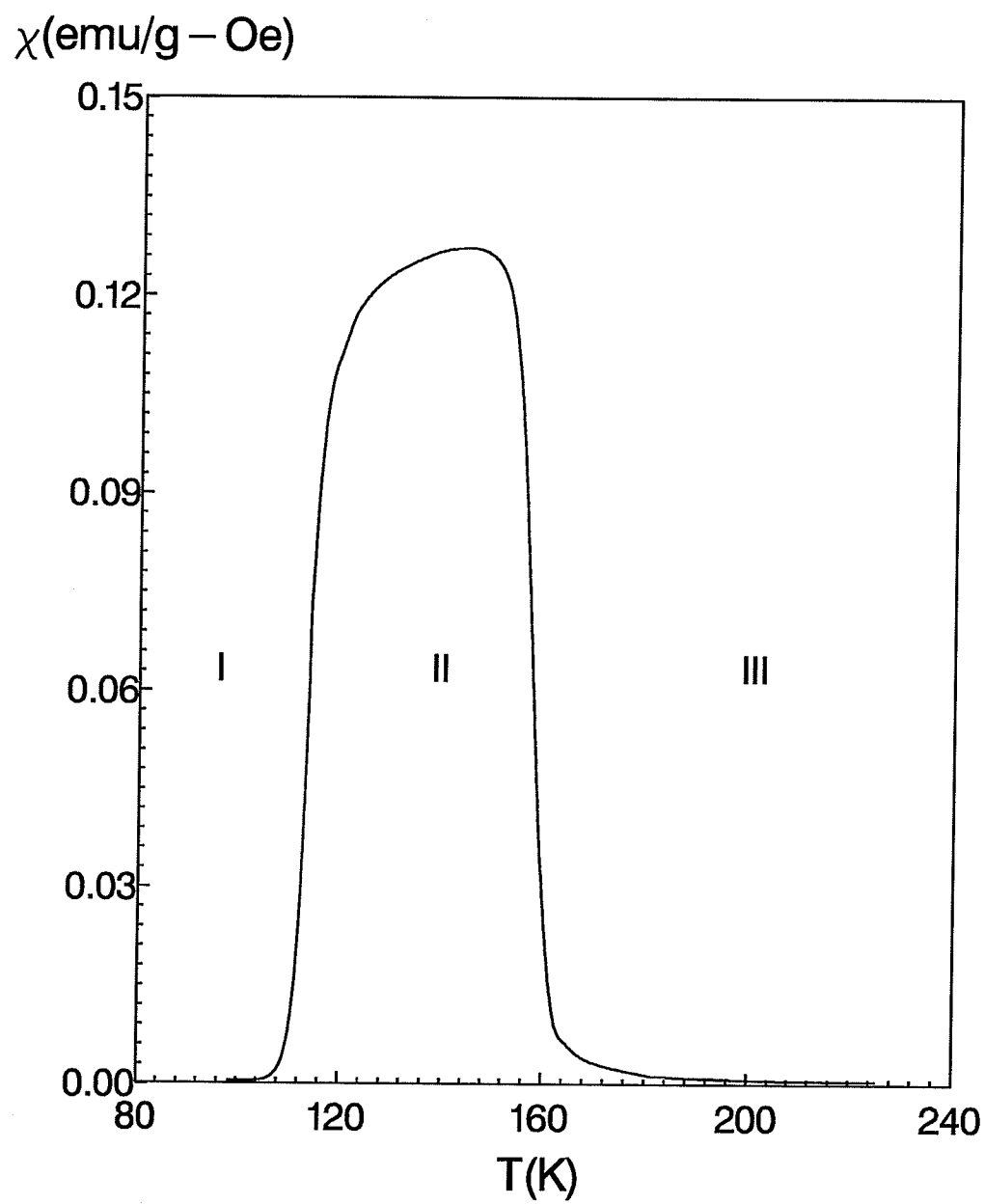


Figure 5.2: Zero field a. c. magnetic susceptibility vs. temperature for $\text{Ce}(\text{Fe}_{0.93}\text{Ru}_{0.07})_2$

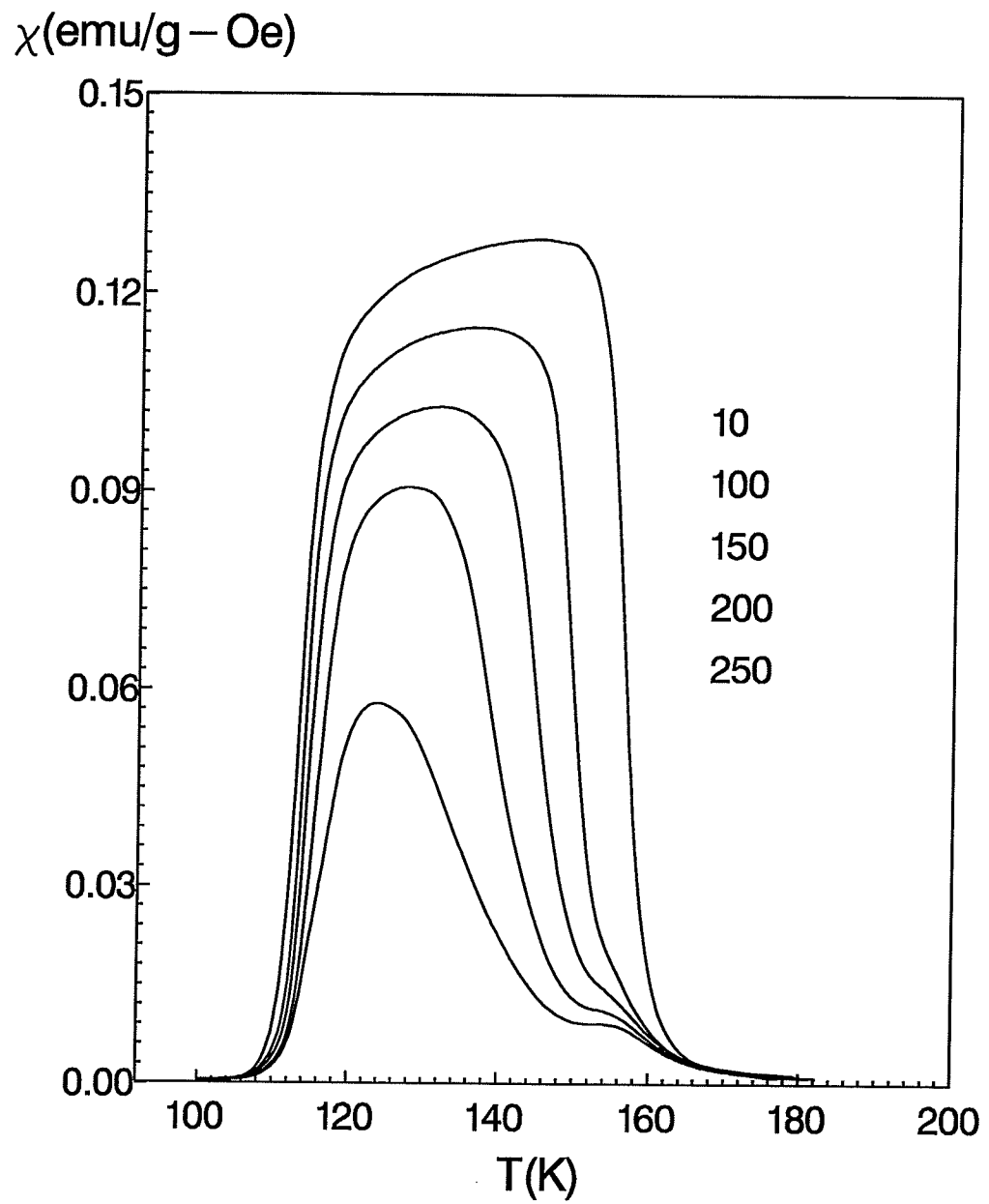


Figure 5.3: (a) a. c. magnetic susceptibility of $\text{Ce}(\text{Fe}_{0.93}\text{Ru}_{0.07})_2$ in a number of applied external fields ranging from 10 ~ 250 Oersted and labelled from top to bottom, respectively

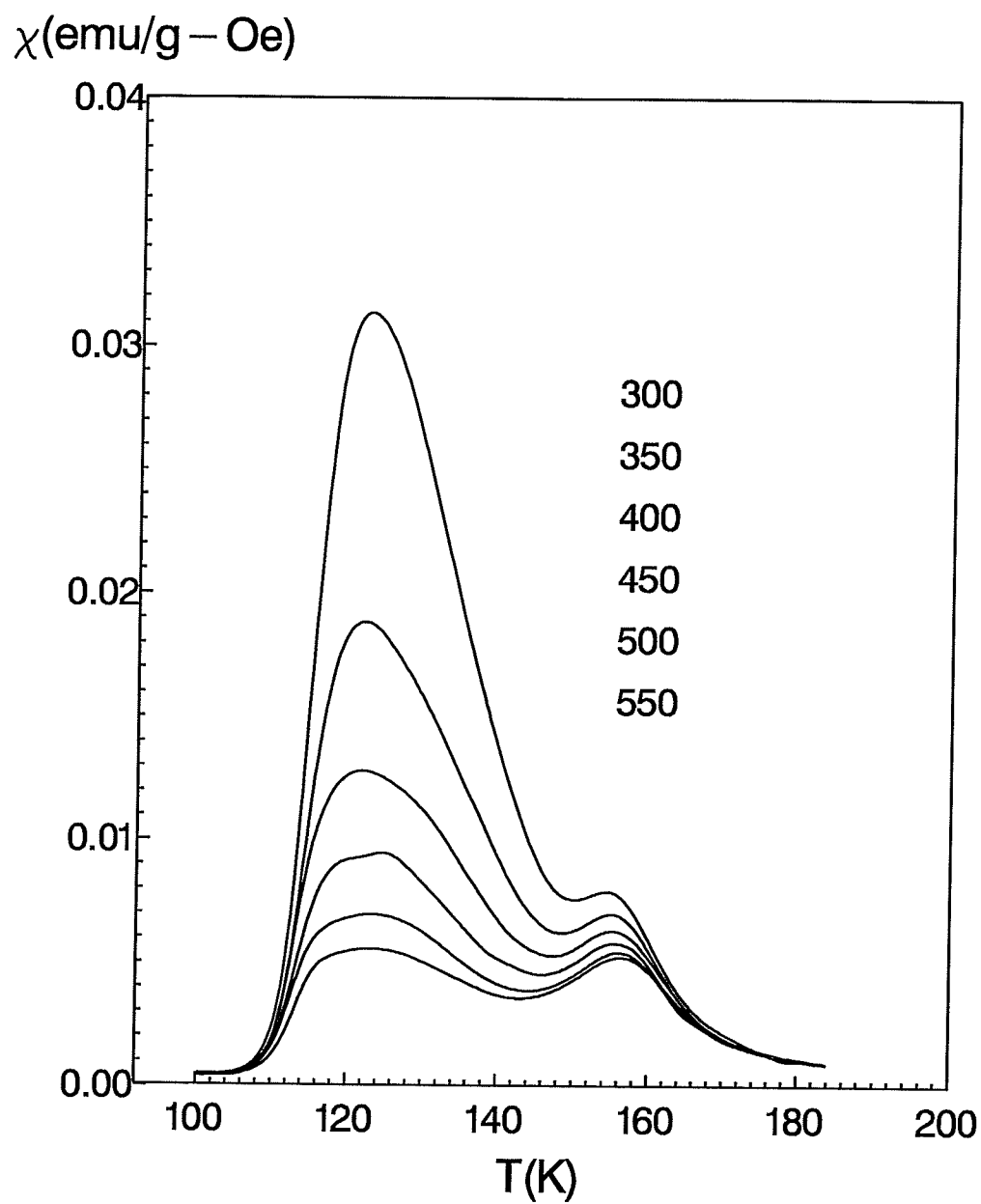


Figure 5.3: (b) a. c. magnetic susceptibility of $\text{Ce}(\text{Fe}_{0.93}\text{Ru}_{0.07})_2$ in applied external fields ranging from 300 ~ 550 Oersted, labelled from top to bottom, respectively

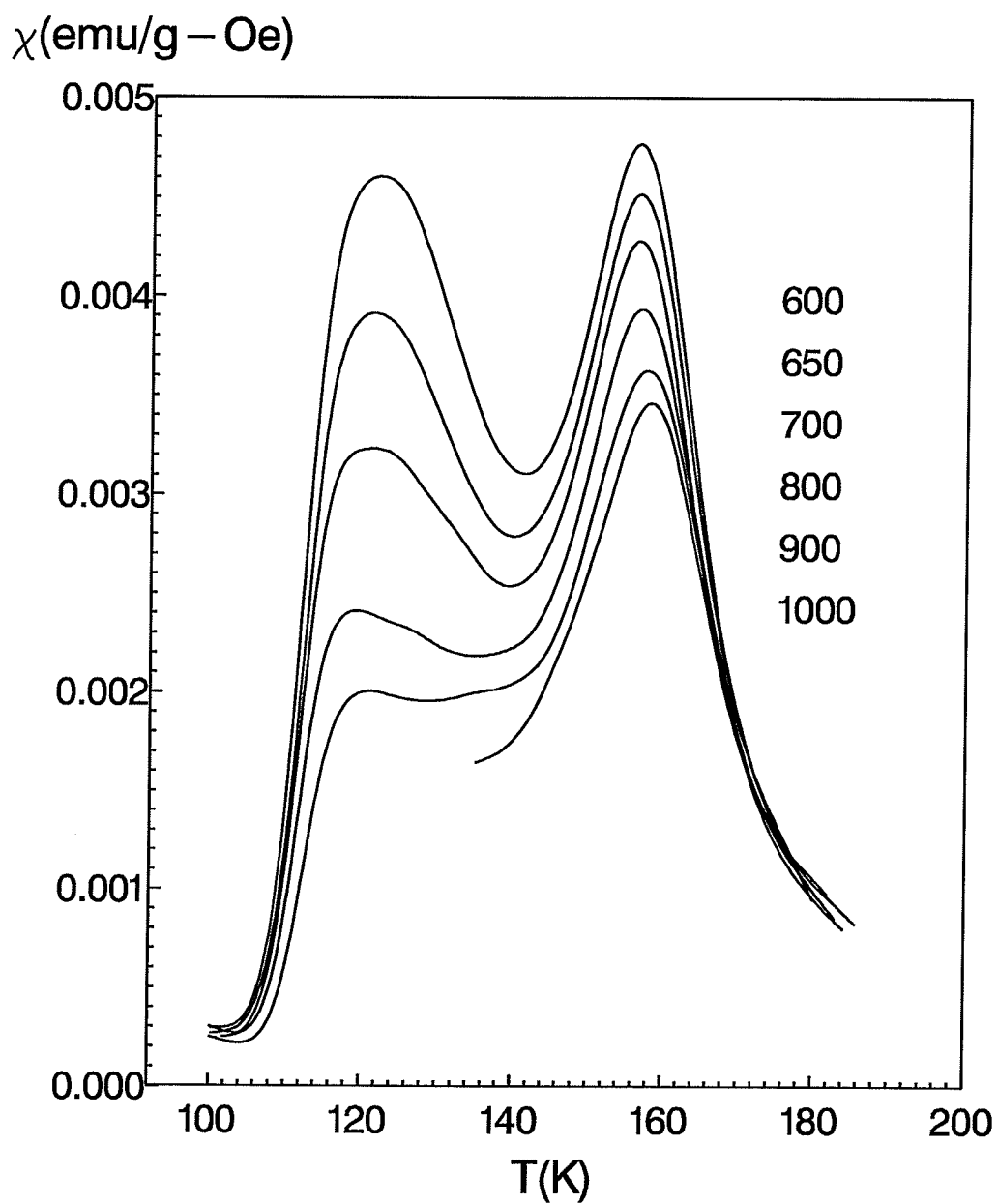


Figure 5.3: (c) a. c. magnetic susceptibility of $\text{Ce}(\text{Fe}_{0.93}\text{Ru}_{0.07})_2$ in applied external fields ranging from 600 ~ 1000 Oersted, labelled from top to bottom, respectively

signal is below the noise level thereafter. One prominent feature of the curve is that it clearly exhibits three distinct regions, marked as I, II and III on the graph. Region II, bounded by the temperatures above $130K$ and below $150K$, is characterized by a strong plateau-like magnetic response inclined slightly towards the low temperature side, a possible indicator of long range magnetic order. Outside this range (region I: below $130K$, region III: above $150K$), the signal falls drastically and approaches zero. This is the characteristic feature of a sequential phase transition going from paramagnetic to ferromagnetic to possibly an antiferromagnetic or spin-glass ground state with decreasing temperature, with the critical temperatures reasonably well defined by the sudden change in susceptibility. It is apparent that at the low temperature side the signal drops to zero (within the sensitivity of the apparatus) below a certain temperature, while at the high temperature side (region III) a measurable signal persists to quite high temperature while diminishing with decreasing slope. These features are discussed in more detail below:

Figure 5.4 is a plot of the zero field susceptibility (above T_c) against the reduced temperature on a double-logarithmic scale, while the so-called effective susceptibility exponent $\gamma^*(t)$, defined by

$$\gamma^*(t) = \frac{d \ln[\chi(0, t)]}{d(\ln t)} \quad (5.8)$$

which is the local slope of fig. 5.4, is plotted in fig. 5.5 against the reduced temperature t (the critical temperature T_c is determined in the next section). $\gamma^*(t)$ increases rapidly with increasing reduced temperature at small t , reaches a maximum of $\gamma_{max}^*(t) = 2.5$ at $t \simeq 0.1$ before gradually falling towards the asymptotic mean field value of 1.

$\gamma^*(t)$ approaches zero at small t , this is because the susceptibility fails to reach the demagnetizing limit at the critical temperature; i.e., the susceptibility fails to

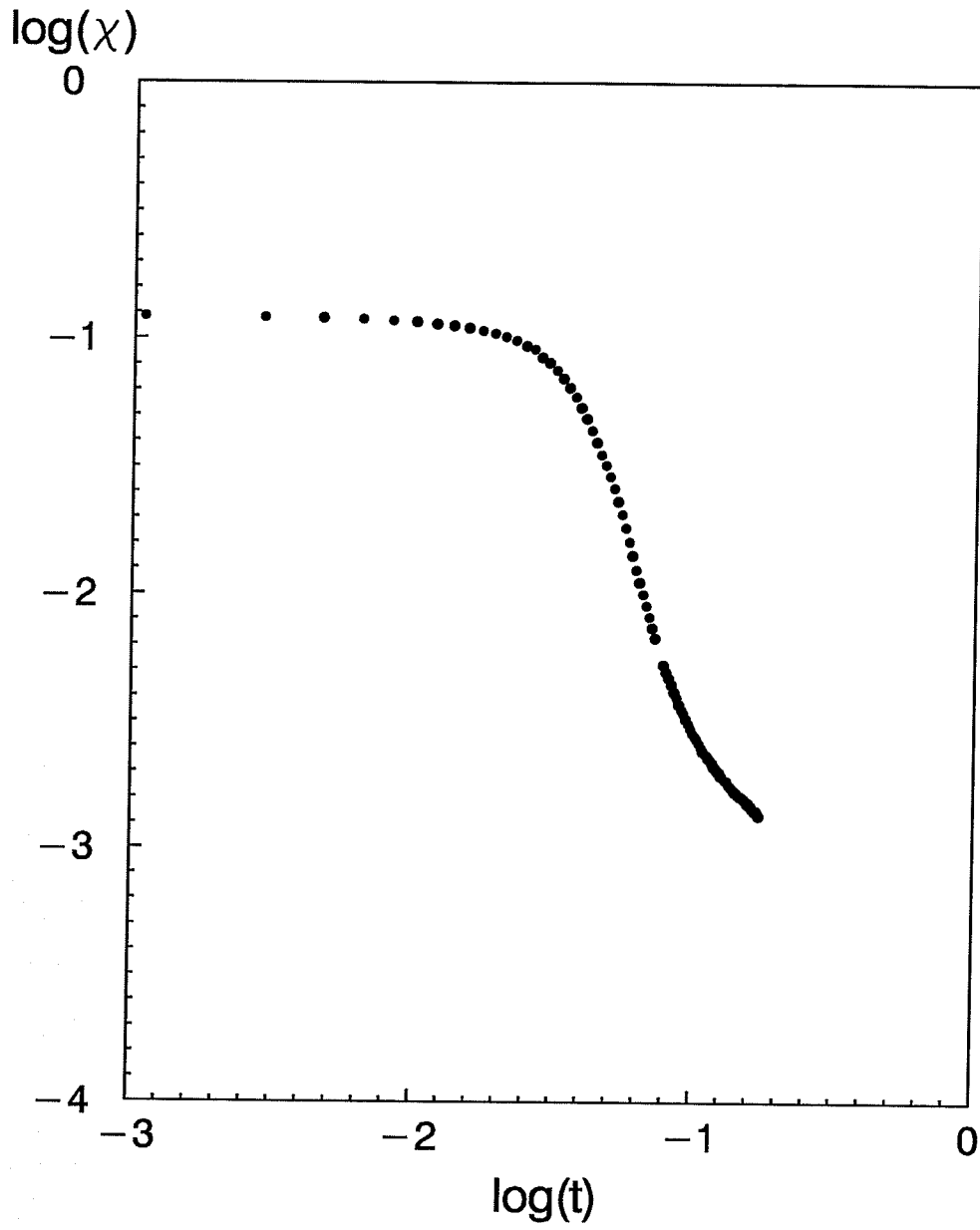


Figure 5.4: Zero field a. c. susceptibility of $\text{Ce}(\text{Fe}_{0.93}\text{Ru}_{0.07})_2$ vs. reduced temperature plotted on a double-logarithmic scale (above T_c)

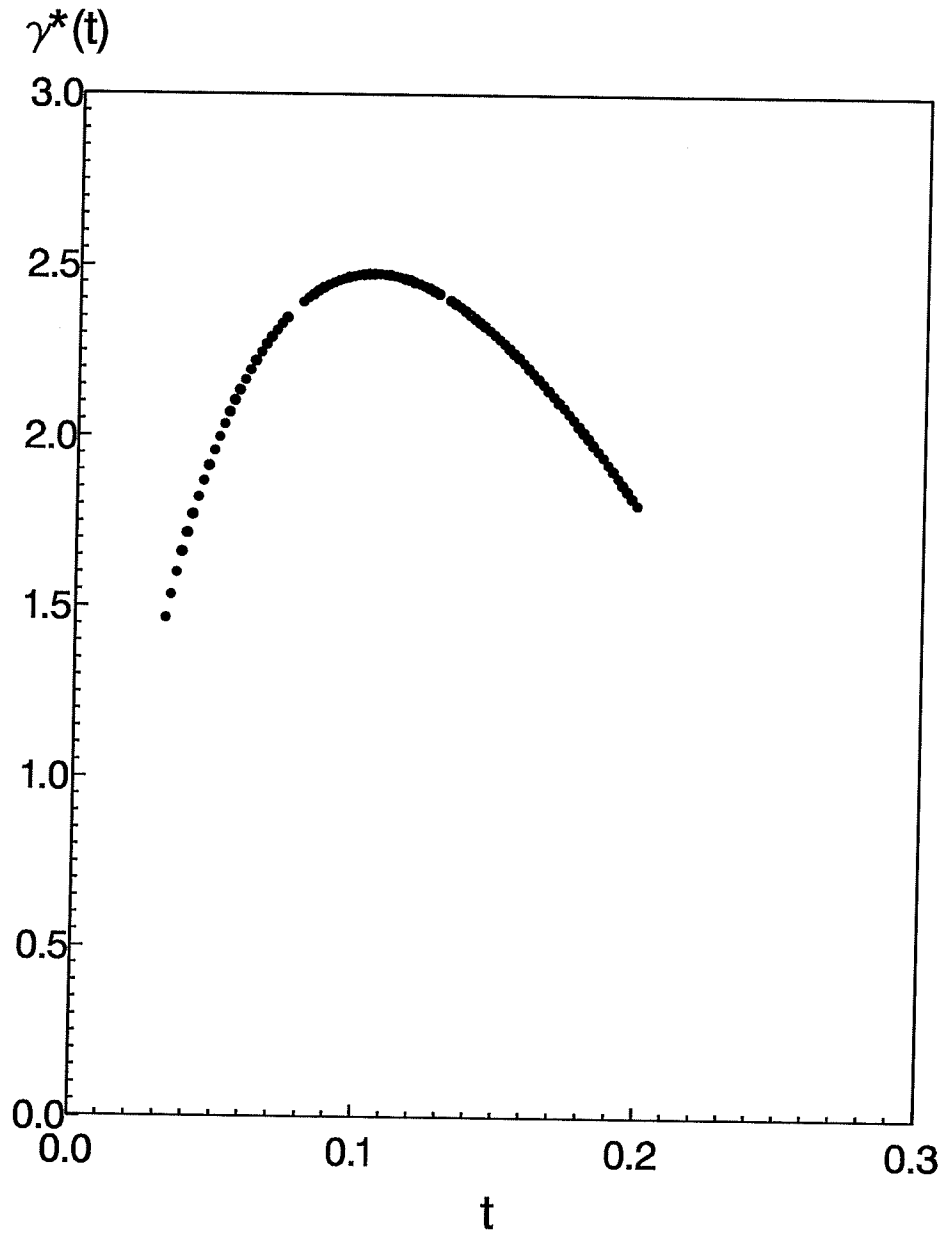


Figure 5.5: Effective susceptibility exponent $\gamma^*(t)$ vs. reduced temperature for $\text{Ce}(\text{Fe}_{0.93}\text{Ru}_{0.07})_2$, the peak occurs at $t_{max} = 0.1, \gamma^*_{max}(t) = 2.5$

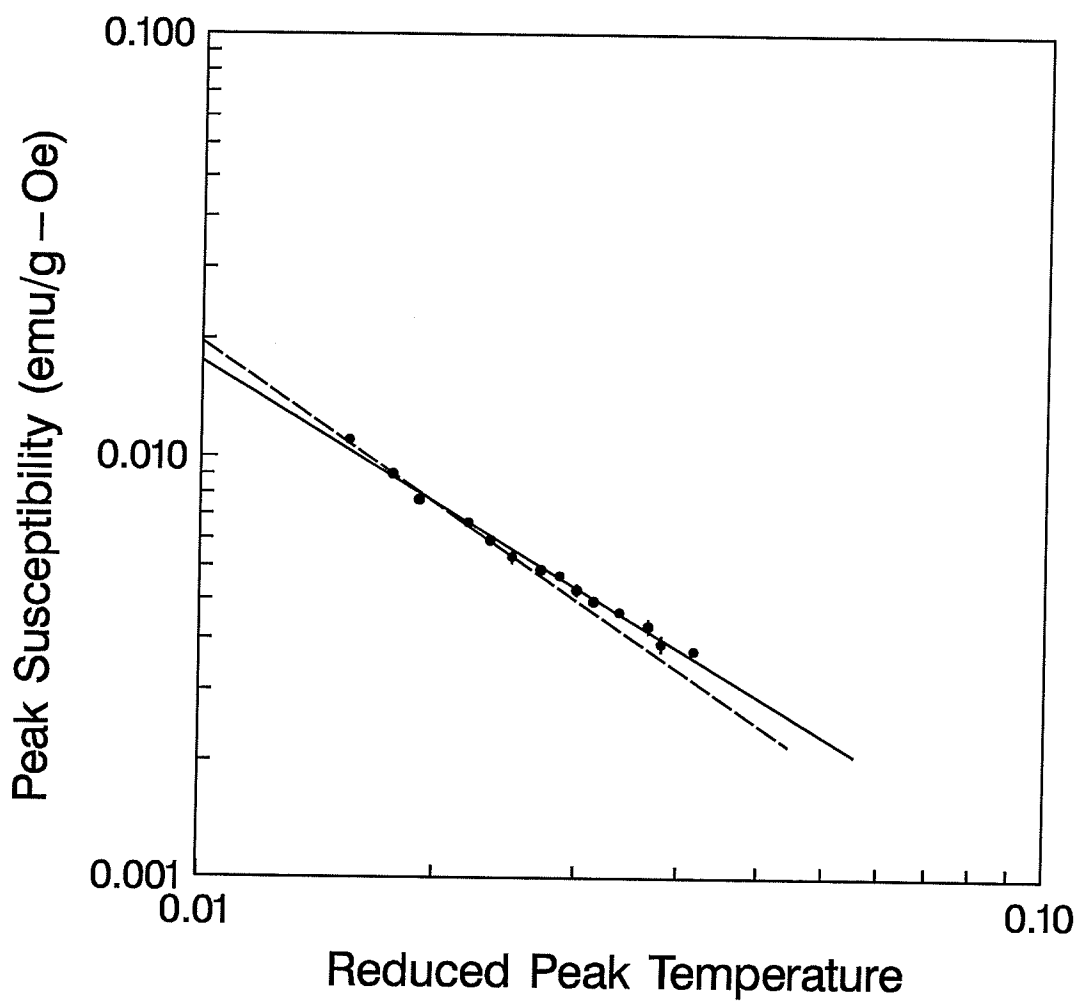


Figure 5.6: Peak susceptibility plotted against the reduced peak temperature for $\text{Ce}(\text{Fe}_{0.93}\text{Ru}_{0.07})_2$ on a double-log scale, the slope of the solid line yields $\gamma = 1.20 \pm 0.03$, the low temperature value of the exponent γ given by the dashed line, is $\gamma = 1.38 \pm 0.03$, a result consistent with Heisenberg prediction.

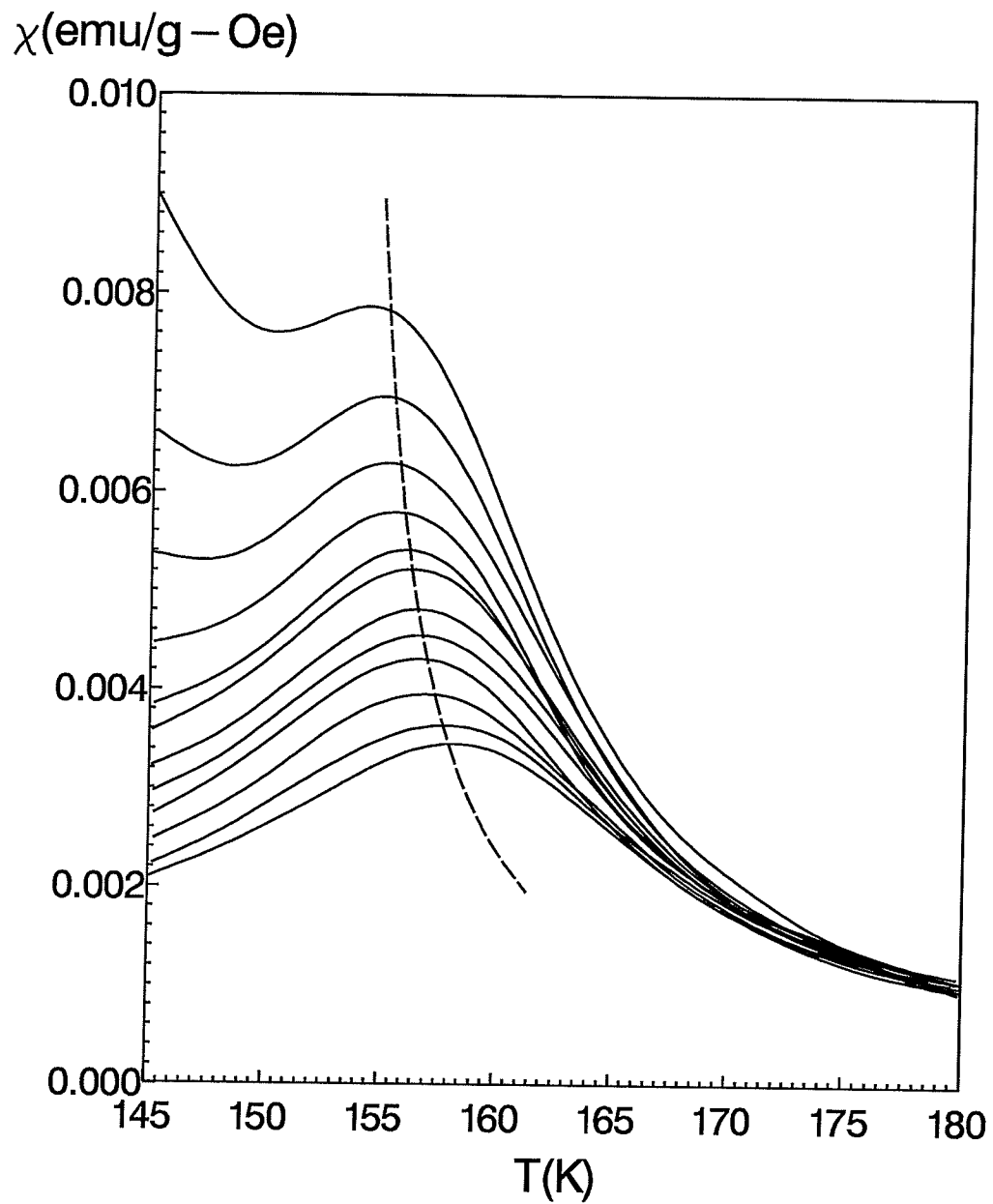


Figure 5.7: D. C. biasing field dependence of a. c. susceptibility of $\text{Ce}(\text{Fe}_{0.93}\text{Ru}_{0.07})_2$ near the critical temperature. The solid lines are temperature sweeps in different external fields and the dashed cross-over line illustrates the $\chi_m \sim t_m^{-\gamma}$ relation.

diverge due to anisotropy effect³. However, there is an alternative method to study the critical behaviour above the transition temperature. In section 2.3.2 we discussed the scaling relations for the critical peaks (the high temperature peaks in fig. 5.3); using eqn. (2.30) ($t_m \sim H_i^{1/(\gamma+\beta)}$) and (2.31) ($\chi_m(H, t_m) \sim H_i^{1/\delta-1}$), along with the Widom equality $\gamma = \beta(\delta - 1)$, yields

$$\chi_m(H, t_m) \sim t_m^{-\gamma} \quad (5.9)$$

To interpret this equation: the peak height and peak temperature of the secondary peak are related by a simple power law. Fig. 5.6 is the plot of χ_m vs. t_m on a double-logarithmic scale, and the slope yields an average γ -value of 1.20 ± 0.03 . The slight upward curvature in the plot at low temperature can increase the value of γ to 1.38 ± 0.05 very close to T_c , in agreement within experimental error with the 3D-Heisenberg prediction 1.388. This low temperature fit is represented by the dashed line in the figure 5.6. This clearly Heisenberg-like result, in comparison to the mean-field result of unity, strongly suggests the existence of short range exchange coupling between spin moments which is the essential difference between the mean-field and Heisenberg models. This relation can be best illustrated as in fig. 5.7, where the solid lines represent the temperature dependence near the transition temperature for several applied fields (isochamps), and the broken line, known as the cross-over line, illustrates the corresponding behaviour of the critical peaks.

5.2.2 The Ferromagnetic Transition

Scaling theory (Section 2.3.2) establishes a set of power laws describing the critical behaviour of the susceptibility in the vicinity of the transition temperature, namely

$$\chi_m(H_i, T_m) \sim H_i^{1/\delta-1} \quad (5.10)$$

³Since $\chi_t = \chi_m/(1 - N \cdot \chi_m)$, the measured susceptibility is limited to $\chi_m < 1/N$.

$$t_m = \frac{T_m - T_c}{T_c} \sim H_i^{1/(\gamma+\beta)} \quad (5.11)$$

$$\chi(H, t_m) \sim t_m^{-\gamma} \quad (5.12)$$

here t_m is the reduced peak temperature, T_c is the critical temperature, T_m is the temperature at which the critical peak occurs, H_i is the internal field and χ_t is the true susceptibility. These relations can be tested with experimental data.

Figure 5.8 plots the peak susceptibility χ_m against the internal field H_i on a double-logarithmic scale for $\text{Ce}(\text{Fe}_{0.93}\text{Ru}_{0.07})_2$. The well defined straight line agrees with eqn. (5.10) and yields the value for the exponent $\delta = 3.08 \pm 0.08$, which is close to the MFT value. The slight upward curvature at low field indicates δ may asymptotically approach the 3D-Heisenberg value; in fact, a linear fit to the points in the low field region yields a value of $\delta = 3.8 \pm 0.1$. Such deviations (upward curvature) from a straight line has been observed, for instance, in PdMn [25] for concentrations of Mn higher than 2.5at.%Mn (these samples have very small demagnetizing factors), where the local δ -value decreases from 4.2 to 4.0 when the field increases. Numerical calculations based on the generalized effective field approach (Kaneyoshi 1975 and Southern 1976) by Roshko and Williams [25] also reproduces the systematics of these experimental data, and this feature has been adopted as a guideline for estimating the demagnetizing factor for samples with unconventional shapes (section 5.1.4). For the CeFe_2 sample, the plot of χ_m vs. H_i on a double-logarithmic scale showed a virtually linear relation with zero demagnetizing correction (i.e. $N = 0$), but curves downwards when a demagnetizing factor based on an ellipsoidal calculation is used. By reducing the demagnetizing factor, it is found that $0.45N$ is the minimum reduction in the demagnetizing factor that can eliminate the unphysical downward curvature. Such a reduction is consistent with the expectation that for samples of this geometry the

ellipsoidal calculation will overestimate the demagnetizing factor [22]. Subsequently a similar reduction factor was employed for the $\text{Ce}(\text{Fe}_{0.93}\text{Ru}_{0.07})_2$ and $\text{Ce}(\text{Fe}_{0.92}\text{Ru}_{0.08})_2$ samples.

The fact that the critical peak structure cannot be resolved below a field of 200Oe indicates the presence of a considerable anisotropy which prevents the regular/technical contributions to the response from saturating, thus precluding an asymptotic (low field) estimate of δ from being made.

The cross-over exponent $(\gamma + \beta)$ can be obtained by plotting t_m vs. H_i on a double-logarithmic scale and calculating the slope of the fitted straight line. However, this requires the prior knowledge of T_c , which according to eqn. (5.11) could be obtained from the intercept of the plot of T_m vs. $H_i^{1/(\gamma + \beta)}$ if $(\gamma + \beta)$ is known. The approach taken is to first assume $(\gamma + \beta)$ has a value near that predicted by the 3D-Heisenberg model (1.755) to derive the T_c value, and then adjust $(\gamma + \beta)$ and T_c by small amount until a self consistent set of parameters is obtained.

Fig. 5.9 and fig. 5.10 give the resulting set of plots from such a self-consistent approach. It is often true for this kind of dilute magnetic systems that T_c is near the inflection point at the high temperature edge, however for both samples examined in this experimental work, the T_c thus determined is closer to the Hopkinson peak. This gives rise to an abnormally large γ , as seen in the previous section. Fig. 5.9 yields $(\gamma + \beta) = 1.79 \pm 0.03$, and the fitted straight line in fig. 5.10 extrapolates to $T_c = (152.3 \pm 0.3)\text{K}$.

As a simple check of the critical exponents obtained, we have the following relations from the Widom equality $\gamma = \beta(\delta - 1)$:

$$\gamma + \beta = \frac{\delta\gamma}{\delta - 1} \quad (5.13)$$

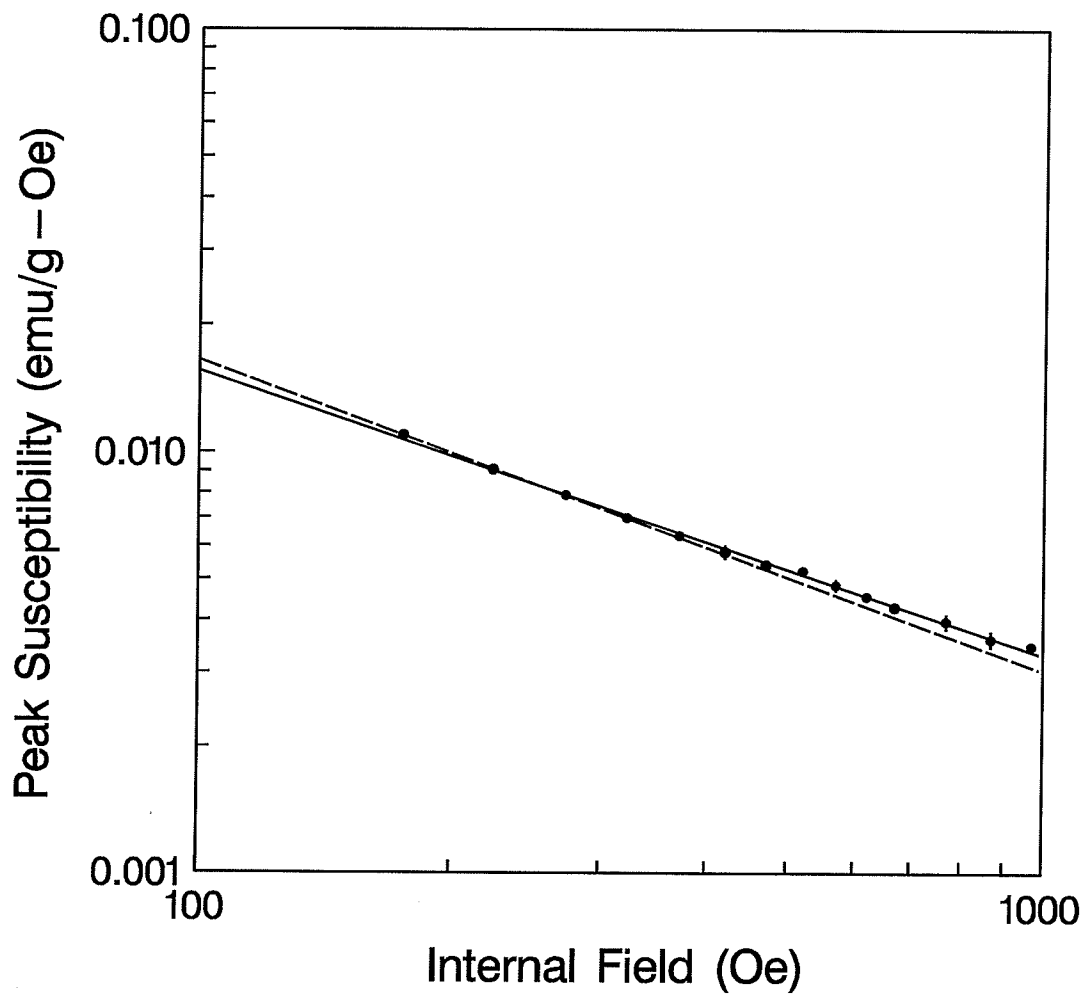


Figure 5.8: Peak susceptibility plotted against internal field on a double-logarithmic scale for $\text{Ce}(\text{Fe}_{0.93}\text{Ru}_{0.07})_2$ — the δ -plot. Where the error bars are not shown, they are within the size of the dot. The solid line yields $\delta = 3.08 \pm 0.08$, and the broken line is a fit to low field points and yields a δ -value of 3.8 ± 0.1

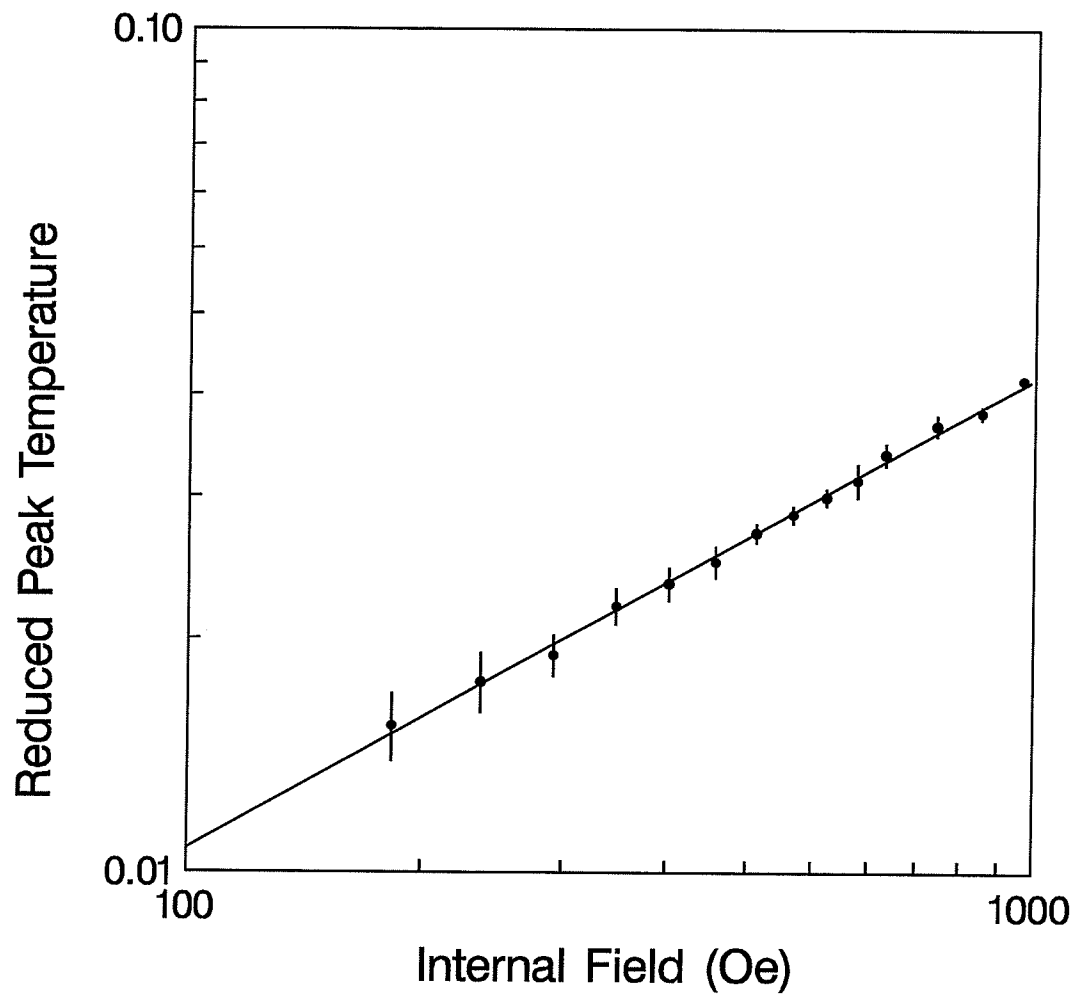


Figure 5.9: Reduced peak temperature plotted against internal field on a double-logarithmic scale for $\text{Ce}(\text{Fe}_{0.93}\text{Ru}_{0.07})_2$ — the cross-over plot. The corresponding cross-over exponent is given by the slope, thus $(\gamma + \beta) = 1.79 \pm 0.03$, which is consistent with the Heisenberg value.

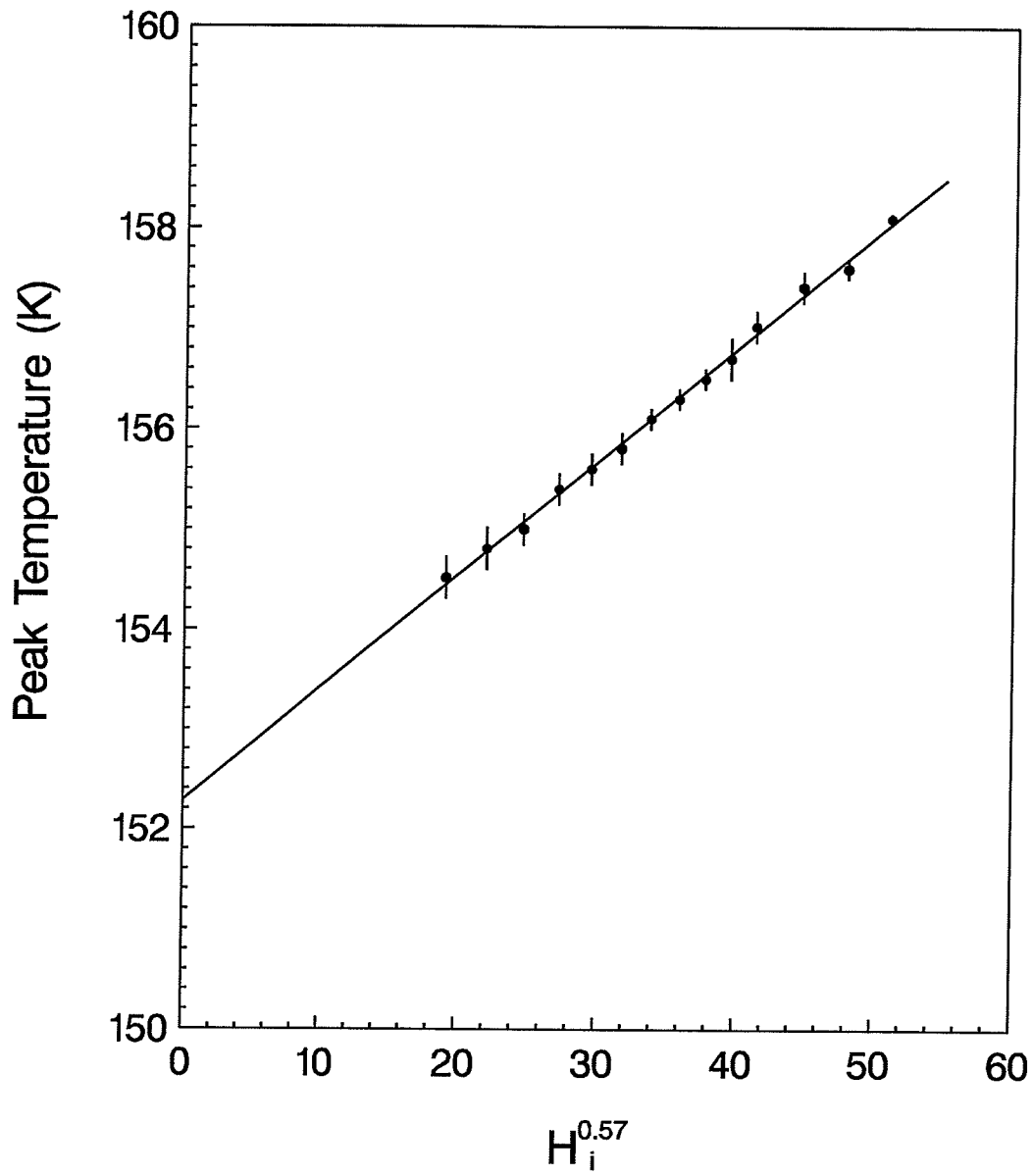


Figure 5.10: Peak temperature plotted against $H_i^{0.57}$ (where the Heisenberg value for the cross-over exponent has been assumed) on linear scale for $\text{Ce}(\text{Fe}_{0.93}\text{Ru}_{0.07})_2$. The intercept at zero field is $T_c = (152.3 \pm 0.3)K$

Incorporating the numerical values, we have $\delta\gamma/(\delta - 1) = 1.78 \pm 0.16$, satisfying the relation within error.

It is evident that for $\text{Ce}(\text{Fe}_{0.93}\text{Ru}_{0.07})_2$, the system undergoes a transition from the paramagnetic to ferromagnetic state with decreasing temperature. This is a common feature in many types of systems including alloys such as PdMn, PdFe, etc..

5.2.3 Low Temperature Transition

At the low temperature edge the susceptibility also displays a steep drop, which may be an indication of a second phase transition. There has been much controversy concerning the characteristic of this potential low temperature phase. The total and abrupt loss of magnetic response suggests that the new phase must be something completely different from the ferromagnetic phase, be it antiferromagnetic or spin-glass. Recent neutron diffraction experiments by Kennedy *et al* [10] have indicated that this is in fact an antiferromagnetic state for the $\text{Ce}(\text{Fe}_{1-x}\text{M}_x)_2$ compounds where M is either Ru, Al, or Co.

While there is no obvious anomaly (peak structure) in the a. c. susceptibility curve to identify this candidate phase transition explicitly, this candidate transition can also be studied by the examination of the nonlinear response. This can be illustrated as follows: In the vicinity of the critical temperature, we can write the susceptibility as a series expansion of the field, at least for sufficiently small fields. Taking into account the necessary symmetry under reversal of the field, the odd terms should not appear, therefore

$$\chi = \chi_0 + a_2H^2 + a_4H^4 + \dots \quad (5.14)$$

The coefficients a_2 , a_4 , etc. decrease in magnitude geometrically and alternate in sign, thus guaranteeing the series will converge for small H . At sufficiently low field, the

higher terms are negligible, and thus

$$\chi \simeq \chi_0 + a_2 H^2 \quad (5.15)$$

to a good approximation. By plotting χ_t vs. H_i^2 one obtains a curve which asymptotically approaches a straight line at sufficiently low field, the slope of which is the coefficient a_2 . This is done in fig. 5.11 for several temperatures in the vicinity of the low temperature edge. It is evident that the initial slope of the curves displays a continuous increase as the low temperature edge is approached from both above and below, i.e., a peak is observed in the plot of the coefficient a_2 (slope) against the temperature in the vicinity of the low temperature dropoff. At the same time, the range of the linear fit decreases as the slope increases, again from both above and below the edge, i.e., the range displays a minimum in the vicinity of the low temperature dropoff. Table 5.1 lists the coefficient $a_2(T)$ for a number of temperatures, several typical values indicating the range of the linear fit are also tabulated. The temperature dependence of a_2 is plotted in fig. 5.12; the plot clearly exhibits a peak (magnitude $7 \times 10^{-6} \text{emu/g}\cdot\text{Oe}^3$) at a temperature $T_f \simeq 117\text{K}$. The peak is not divergent as expected for a phase transition in a very strict sense. T_f is the critical temperature for the second transition.

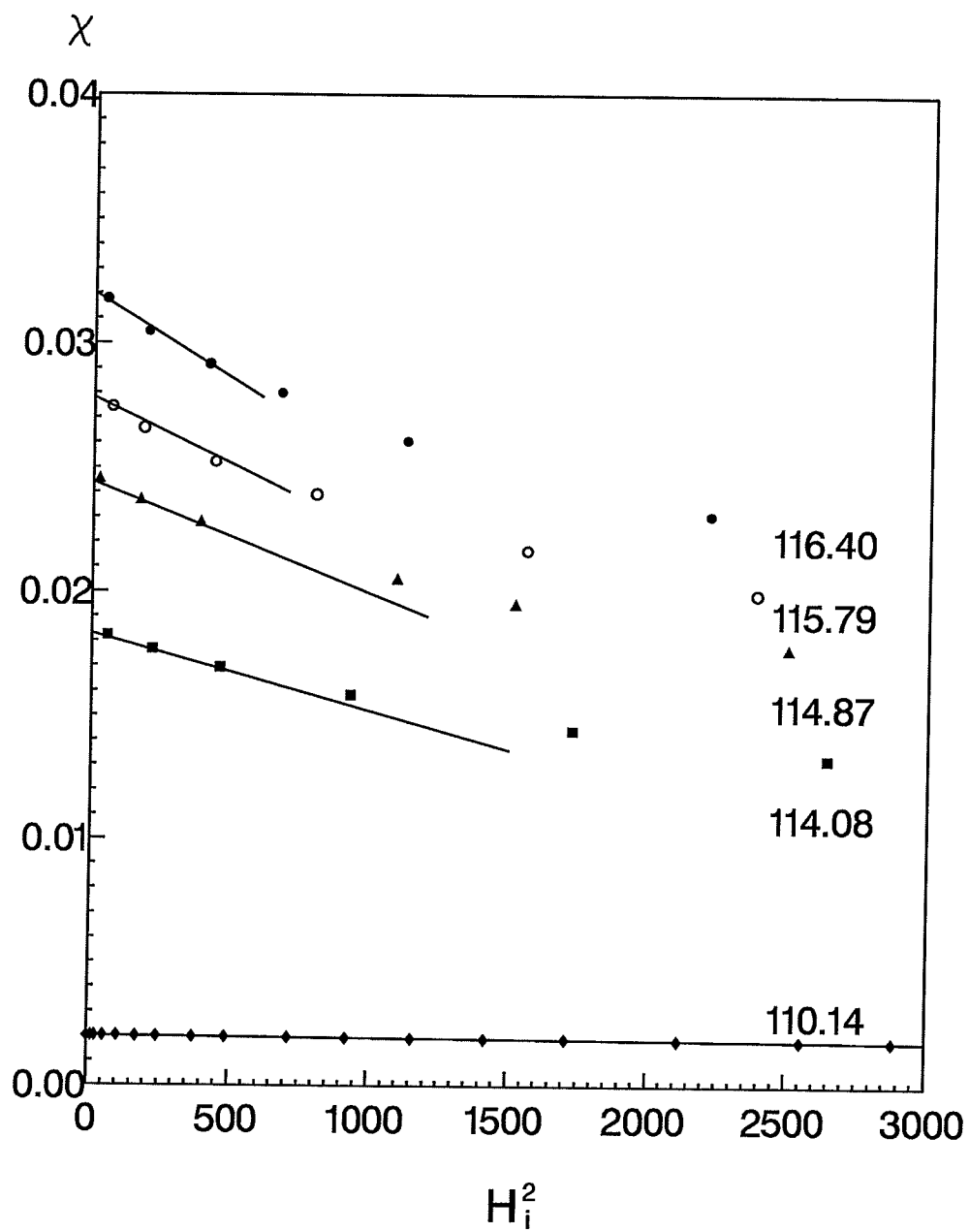


Figure 5.11: (a) Plot of susceptibility χ_t vs. H_i^2 for $\text{Ce}(\text{Fe}_{0.93}\text{Ru}_{0.07})_2$ at several different temperatures near the low temperature transition point in the range 110 ~ 117K. Errorbars are the size of the points.

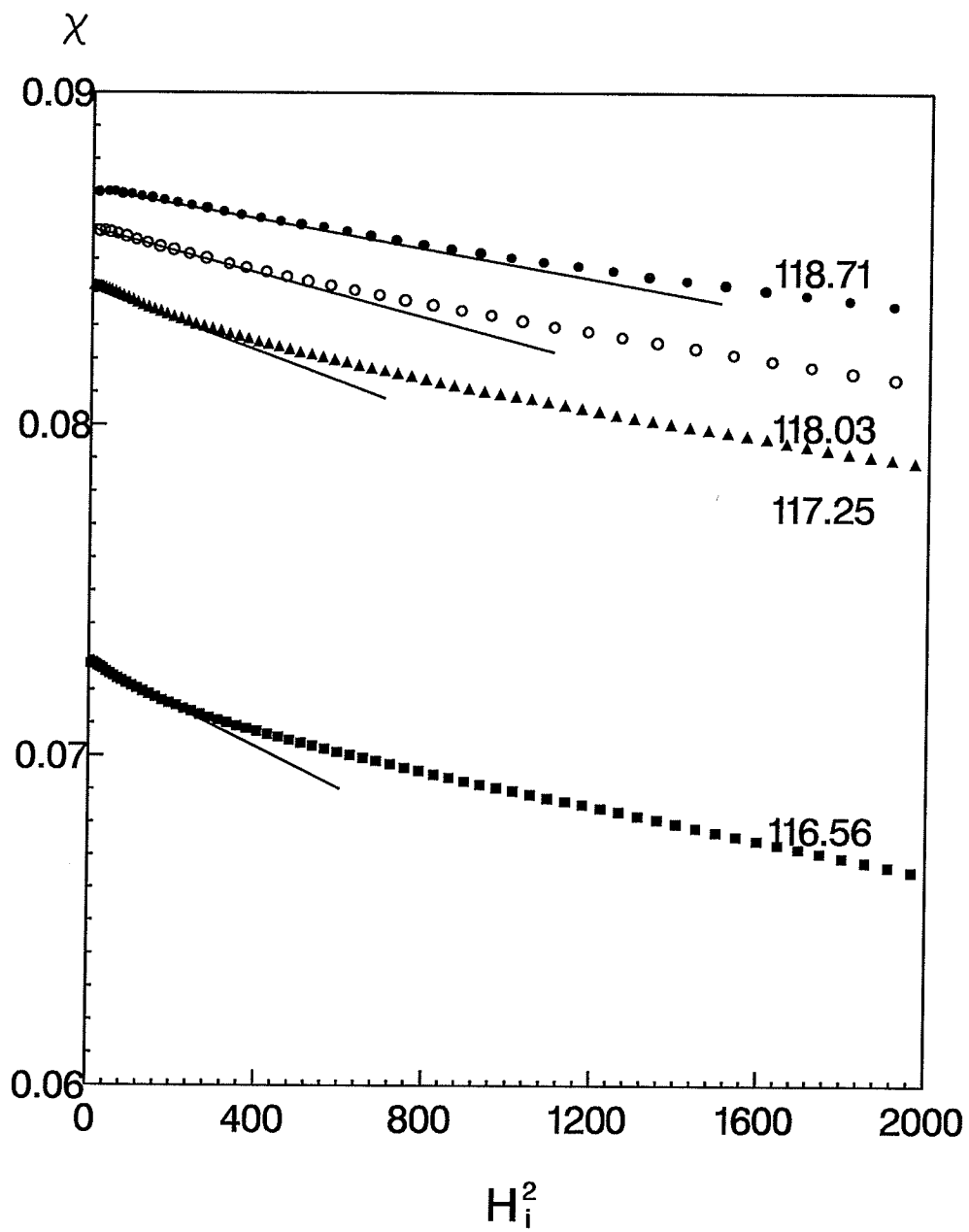


Figure 5.11: (b) Plot of susceptibility χ_t vs. H_i^2 for $\text{Ce}(\text{Fe}_{0.93}\text{Ru}_{0.07})_2$ at several different temperatures near the low temperature transition point in the range 116.5 ~ 120K. Errorbars are the size of the points.

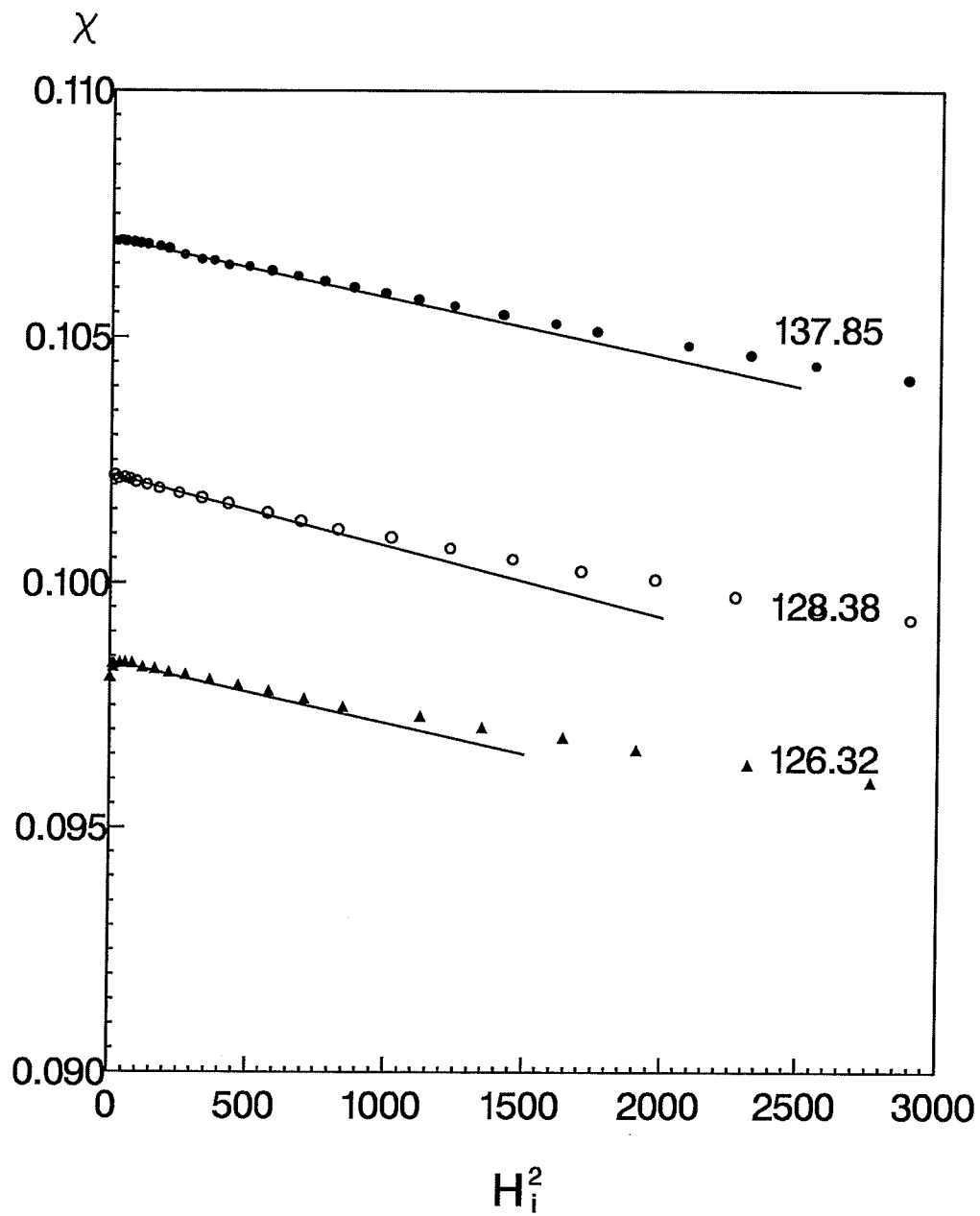


Figure 5.11: (c) Plot of susceptibility χ_t vs. H_i^2 for $\text{Ce}(\text{Fe}_{0.93}\text{Ru}_{0.07})_2$ at several different temperatures near the low temperature transition point in the range 126 ~ 140K. Errorbars are the size of the points.

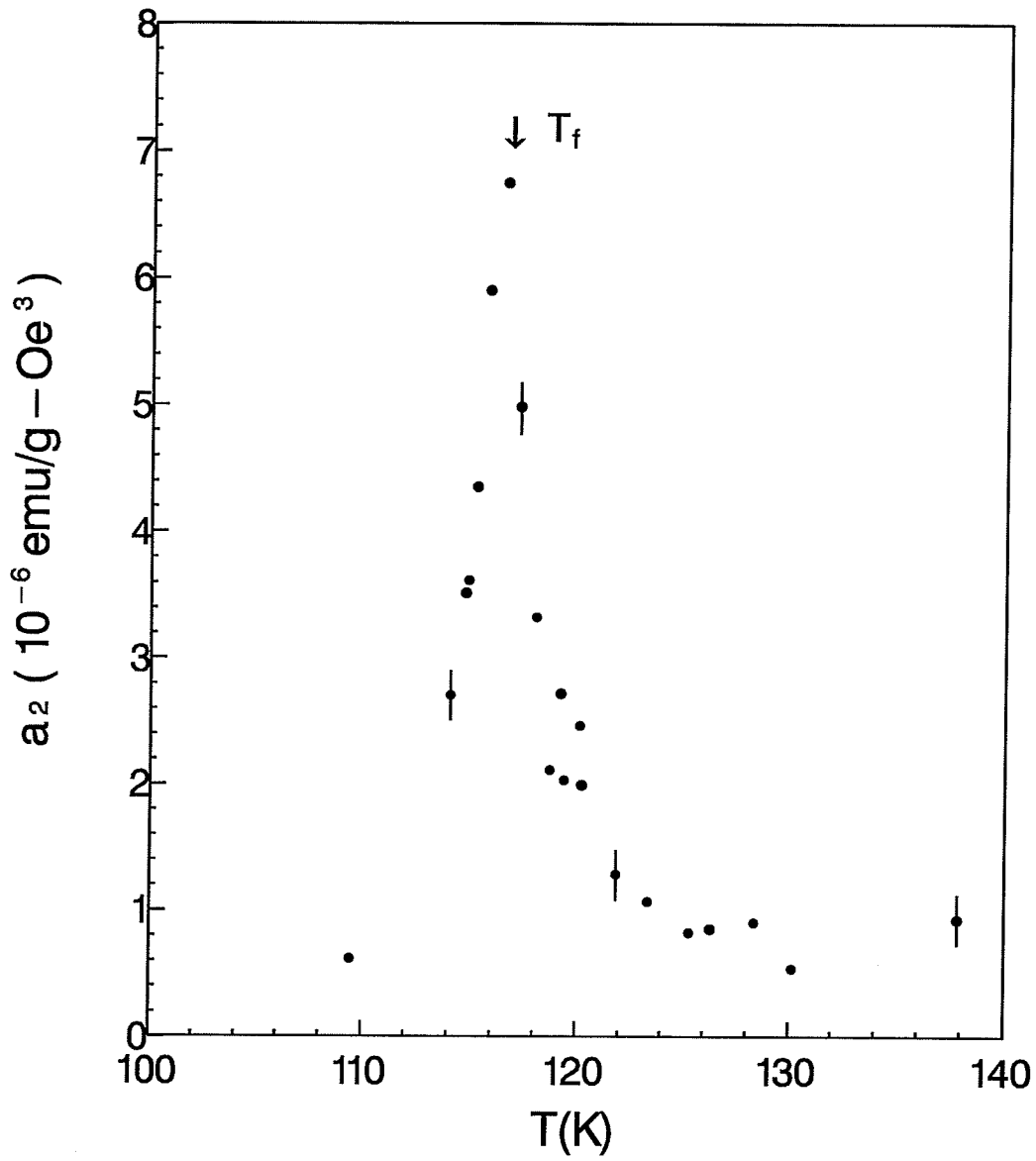


Figure 5.12: Temperature dependence of non-linear coefficient a_2 for $\text{Ce}(\text{Fe}_{0.93}\text{Ru}_{0.07})_2$

Table 5.1: Nonlinear response of $\text{Ce}(\text{Fe}_{0.93}\text{Ru}_{0.07})_2$: $a_2(T)$ vs. T

Temperature T(K)	Slope $a_2(T)$ $\times 10^{-8}(\text{emu/g}\cdot\text{Oe}^3)$	Range (Oe ²)
140.9	113	
137.8	93	1500
130.2	54	
128.4	90	1000
126.3	86	800
125.3	82	
123.4	107	
121.8	128	
120.2	199	
120.1	246	
119.4	203	
119.2	271	
118.7	211	
118.0	332	600
117.2	498	400
116.6	675	300
115.8	590	700
115.3	435	
114.9	362	700
114.8	352	
114.1	270	800
110.1	07	3000
109.4	62	

5.3 Data Analysis for $\text{Ce}(\text{Fe}_{0.92}\text{Ru}_{0.08})_2$

A similar analysis, as described for the $\text{Ce}(\text{Fe}_{0.93}\text{Ru}_{0.07})_2$ sample, was carried out for $\text{Ce}(\text{Fe}_{0.92}\text{Ru}_{0.08})_2$ as well. Figure 5.13 and 5.14 show the susceptibility measurements in zero field and several non-zero external fields, respectively. Generally speaking, $\text{Ce}(\text{Fe}_{0.92}\text{Ru}_{0.08})_2$ displays similar features to that of $\text{Ce}(\text{Fe}_{0.93}\text{Ru}_{0.07})_2$, but some differences also exist.

5.3.1 Zero Field Susceptibility

The zero field susceptibility of $\text{Ce}(\text{Fe}_{0.92}\text{Ru}_{0.08})_2$ also undergoes a rise and a sharp dropoff upon cooling. But the rising edge (high temperature) is much more gradual compared to that of $\text{Ce}(\text{Fe}_{0.93}\text{Ru}_{0.07})_2$; thus the three distinct regions, discussed in the previous section for $\text{Ce}(\text{Fe}_{0.93}\text{Ru}_{0.07})_2$ and representing three sequential magnetic states and two phase transitions, are not as clearly defined. The behaviour in the paramagnetic region is examined in fig. 5.15 and fig. 5.16, which show plots of the zero field susceptibility against the reduced temperature on a double-logarithmic scale, and the effective susceptibility exponent vs. reduced temperature, respectively. Fig. 5.16 shows that the maximum of $\gamma^*(t)$ reaches a value of $\gamma_{max}^*(t) = 3.8$ which is surprisingly large. The reduced temperature at which this maximum occurs is $t = 0.18$, also larger compared to similar systems, including the $\text{Ce}(\text{Fe}_{0.93}\text{Ru}_{0.07})_2$ sample. This abnormally large γ^* , however, has been partly attributed to the determination of T_c : higher T_c corresponds to a smaller $\gamma_{max}^*(t)$ and lower T_c to a larger $\gamma_{max}^*(t)$, thus the value of $\gamma_{max}^*(t)$ can be effectively reduced if the Curie temperature is higher⁴. This suggestion can find its justification in the fact that the regular/non-critical contribution to the

⁴From the definition of $\gamma^*(t)$ in eqn. (5.8), $\gamma = \frac{d \ln[\chi(0,t)]}{d(\ln t)} = \frac{t}{\chi} \frac{d\chi}{dt}$, thus for a given temperature, if T_c is decreased then t and consequently $\gamma^*(t)$ is increased.

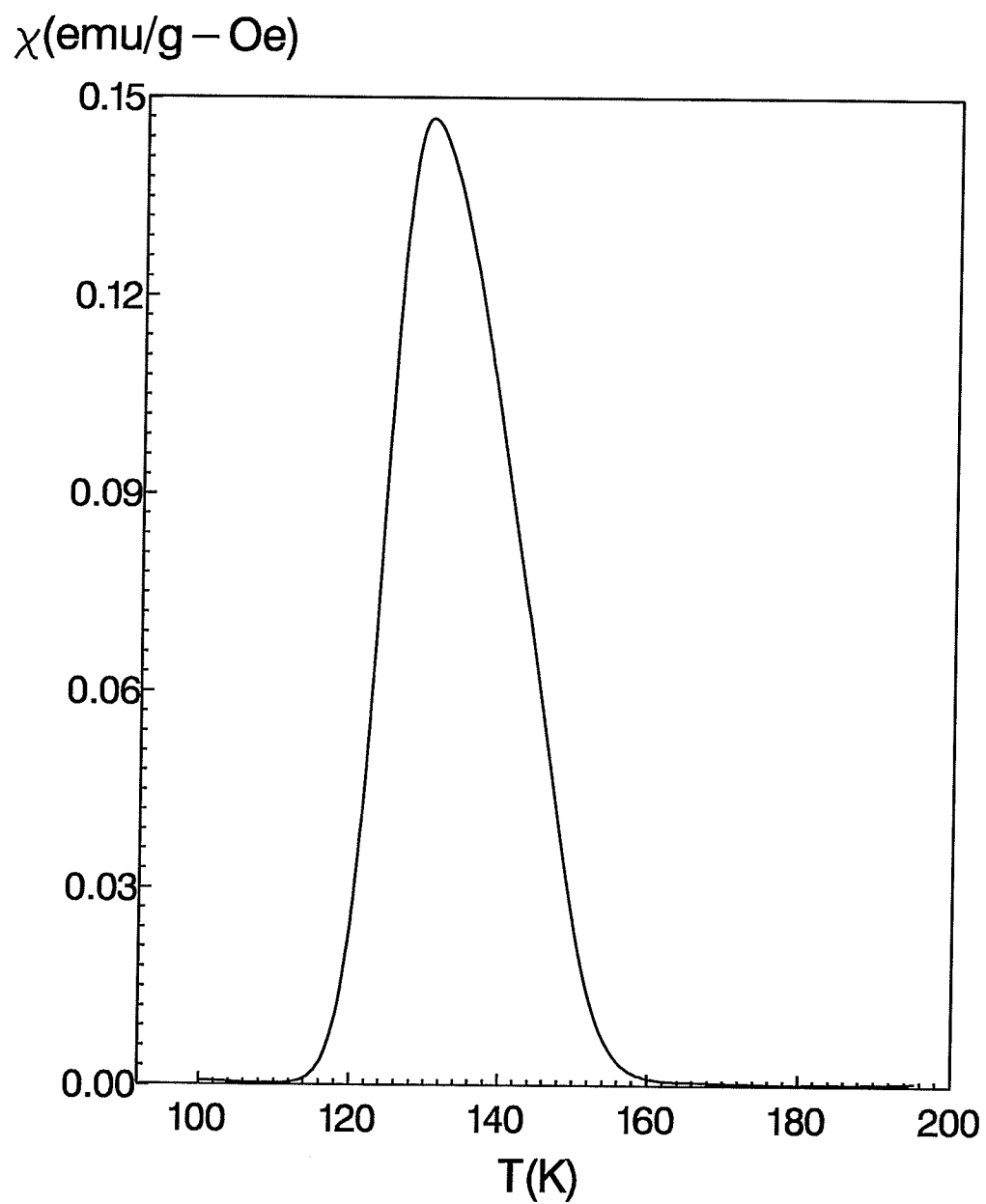


Figure 5.13: Zero field a. c. magnetic susceptibility vs. temperature for $\text{Ce}(\text{Fe}_{0.92}\text{Ru}_{0.08})_2$

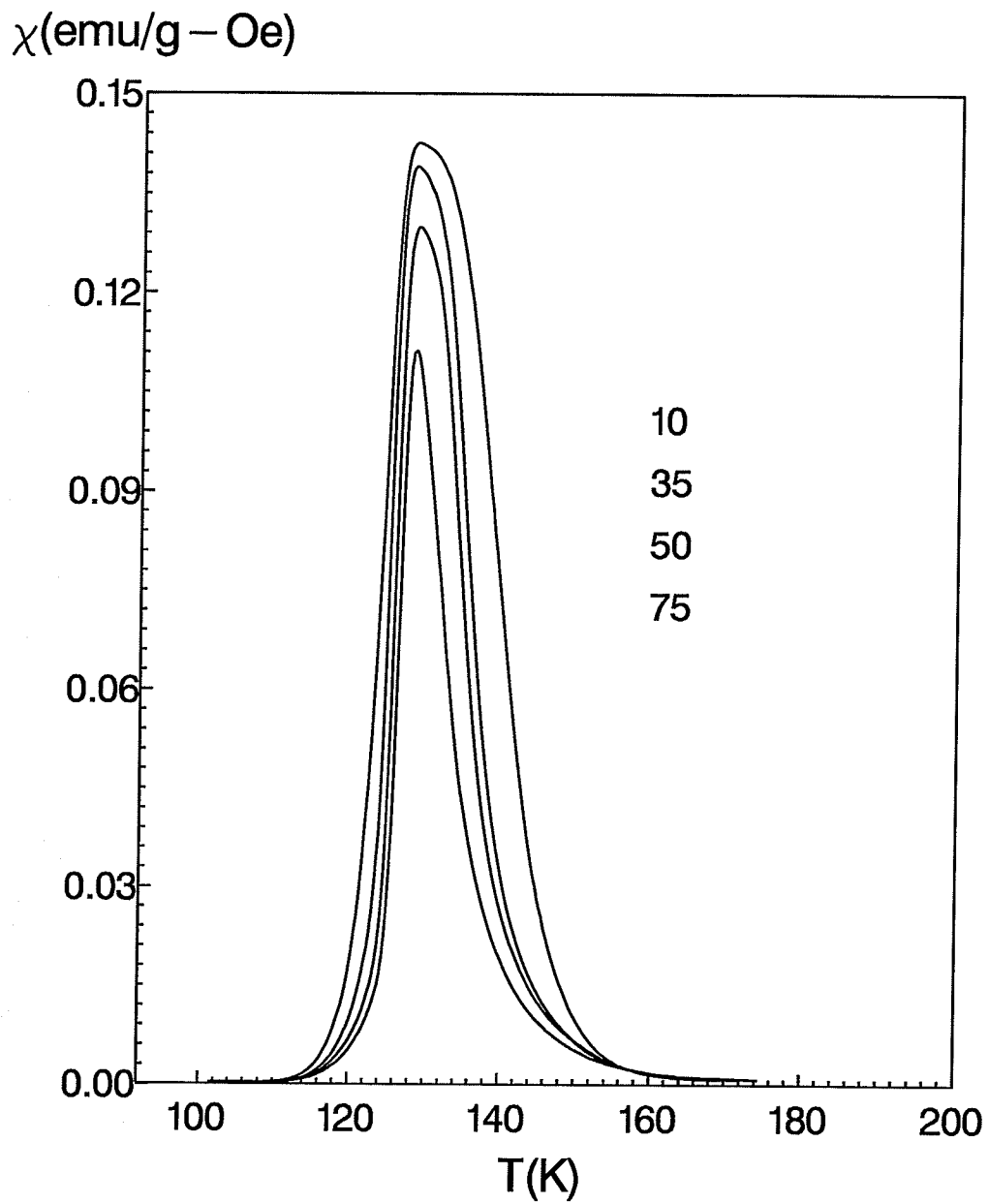


Figure 5.14: (a) a. c. magnetic susceptibility of $\text{Ce}(\text{Fe}_{0.92}\text{Ru}_{0.08})_2$ in a number of applied external fields ranging from 10 ~ 75 Oersted and labelled from top to bottom, respectively

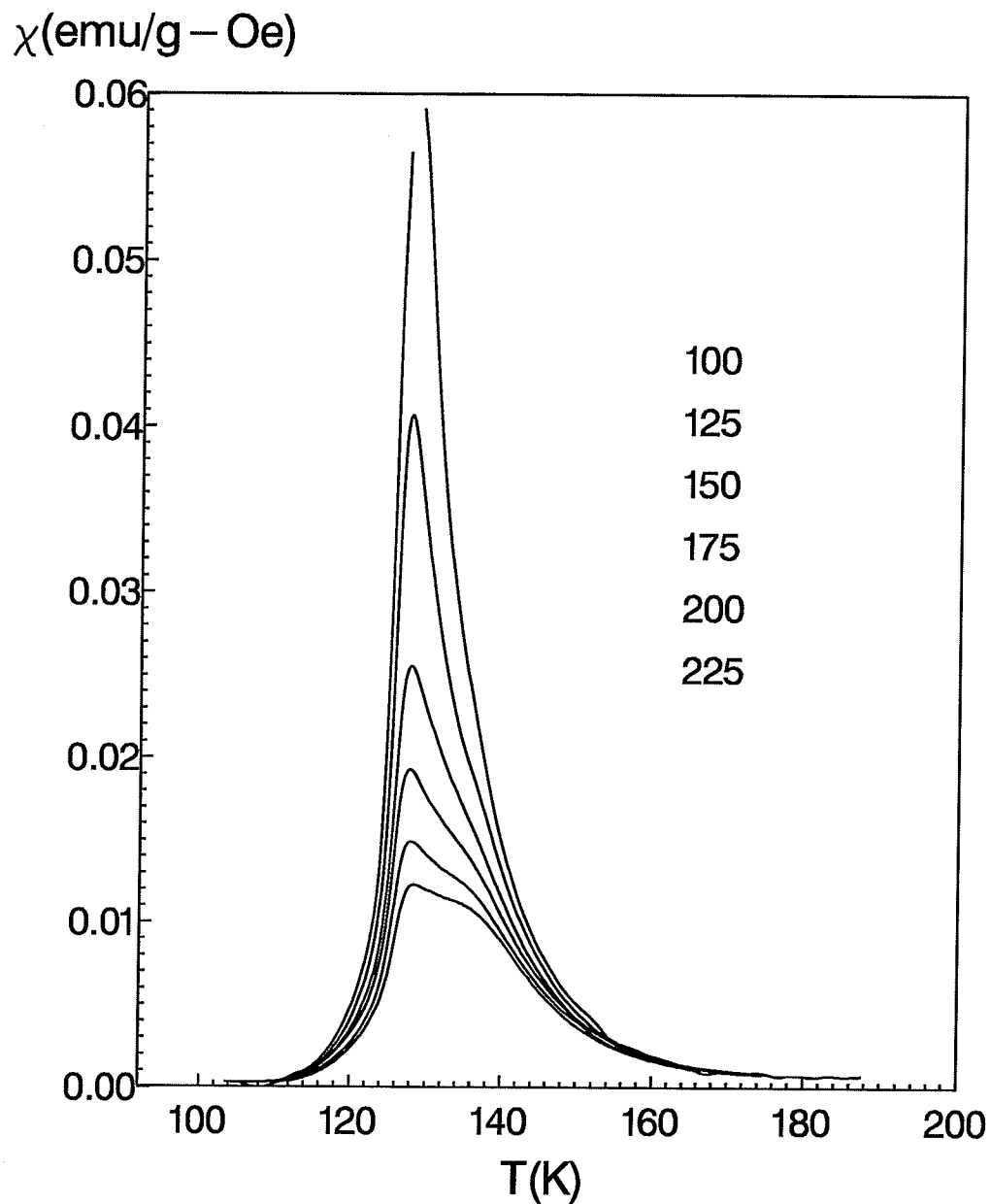


Figure 5.14: (b) a. c. magnetic susceptibility of $\text{Ce}(\text{Fe}_{0.92}\text{Ru}_{0.08})_2$ in a number of applied external fields ranging from 100 ~ 225 Oersted and labelled from top to bottom, respectively

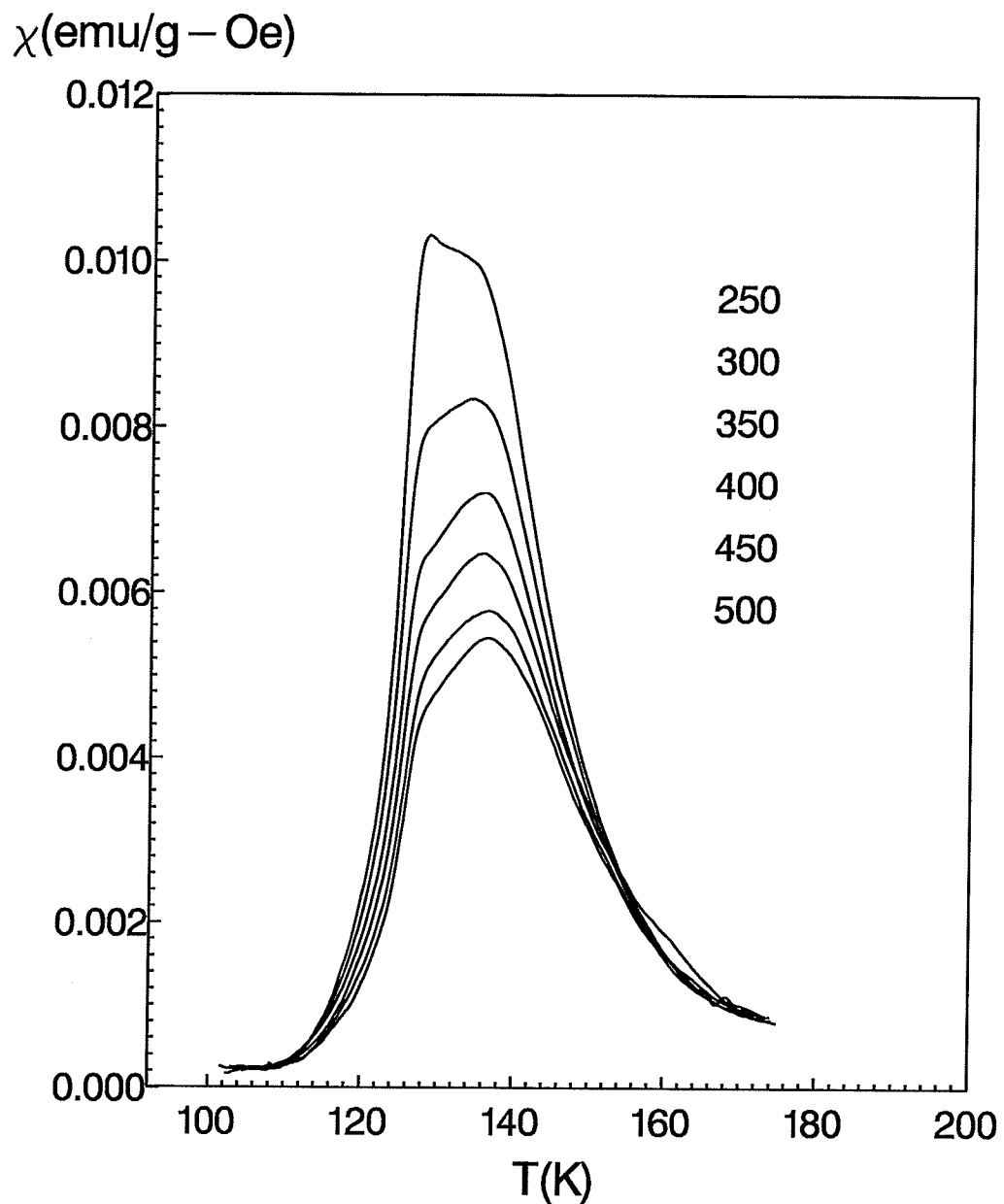


Figure 5.14: (c) a. c. magnetic susceptibility of $\text{Ce}(\text{Fe}_{0.92}\text{Ru}_{0.08})_2$ in a number of applied external fields ranging from 250 ~ 500 Oersted and labelled from top to bottom, respectively

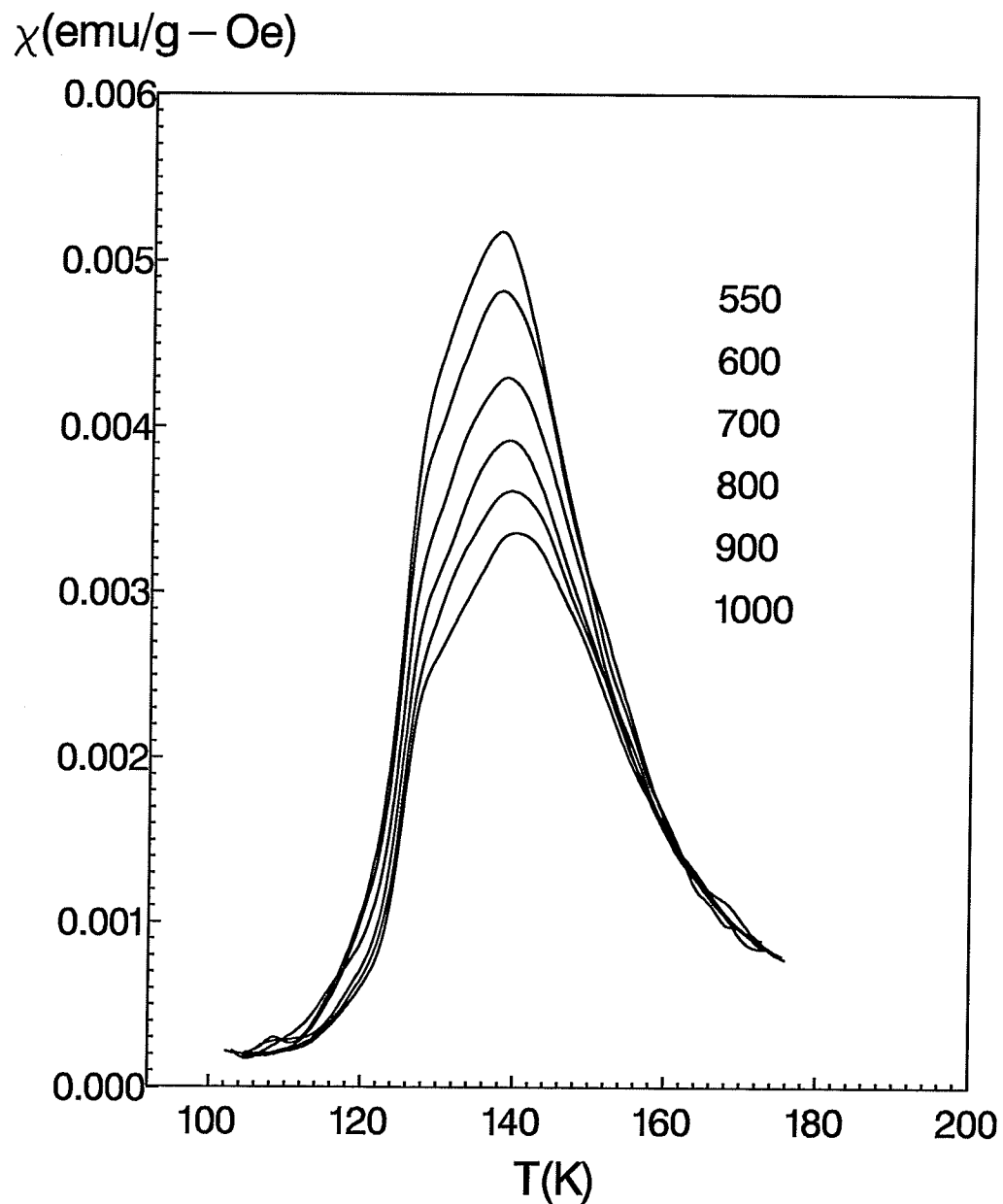


Figure 5.14: (d) a. c. magnetic susceptibility of $\text{Ce}(\text{Fe}_{0.92}\text{Ru}_{0.08})_2$ in a number of applied external fields ranging from 550 ~ 1000 Oersted and labelled from top to bottom, respectively

susceptibility, when superimposed on the critical peak⁵, tends to shift the apparent position of the critical peak towards lower temperature (for the same reason the critical peak may shift the Hopkinson maximum toward higher temperature to a lesser degree), therefore the actual peak temperature could be somewhat higher, implying that T_c also could be slightly higher. Since the amplitude of neither the regular contribution nor the critical peak is well known (we measure the sum), it is uncertain to what extent this will affect the value of T_c and thus $\gamma_{max}^*(t)$.

The asymptotic value of $\gamma^*(t)$ at small t can, however, be evaluated with reference to eqn. (5.9). The peak amplitude χ_m , is plotted against the reduced peak temperature, t_m , in fig. 5.17; the corresponding average yields slope $\gamma = 1.25 \pm 0.03$, but the slight upward curvature at low reduced temperature is consistent with a γ value of 1.44 ± 0.05 , in agreement with the 3D-Heisenberg prediction within experimental error. Fig. 5.18 shows the temperature dependence of the a. c. susceptibility in several applied fields along with the corresponding cross-over line.

5.3.2 Ferromagnetic Transition

The relationship of the peak susceptibility, χ_m , and the reduced temperature of the peak, t_m , with the internal field are plotted in fig. 5.19 and 5.20, respectively, on double logarithmic scale. The δ -exponent from the best fit is $\delta = 3.40 \pm 0.15$. But again, an upward curvature at low field is exhibited, with a low field fit yielding $\delta = 5.1 \pm 0.6$, in agreement with the 3D-Heisenberg prediction ($\delta = 4.78$) within experimental error. The critical temperature T_c obtained from fig. 5.21 and the cross-over exponent ($\gamma + \beta$) obtained from fig. 5.20 are $T_c = (131.4 \pm 0.4)K$ and

⁵The regular contribution to the susceptibility is significant up to fairly large field for these compounds since the anisotropy is quite large — critical peaks are not uncovered for fields less than 200Oe.

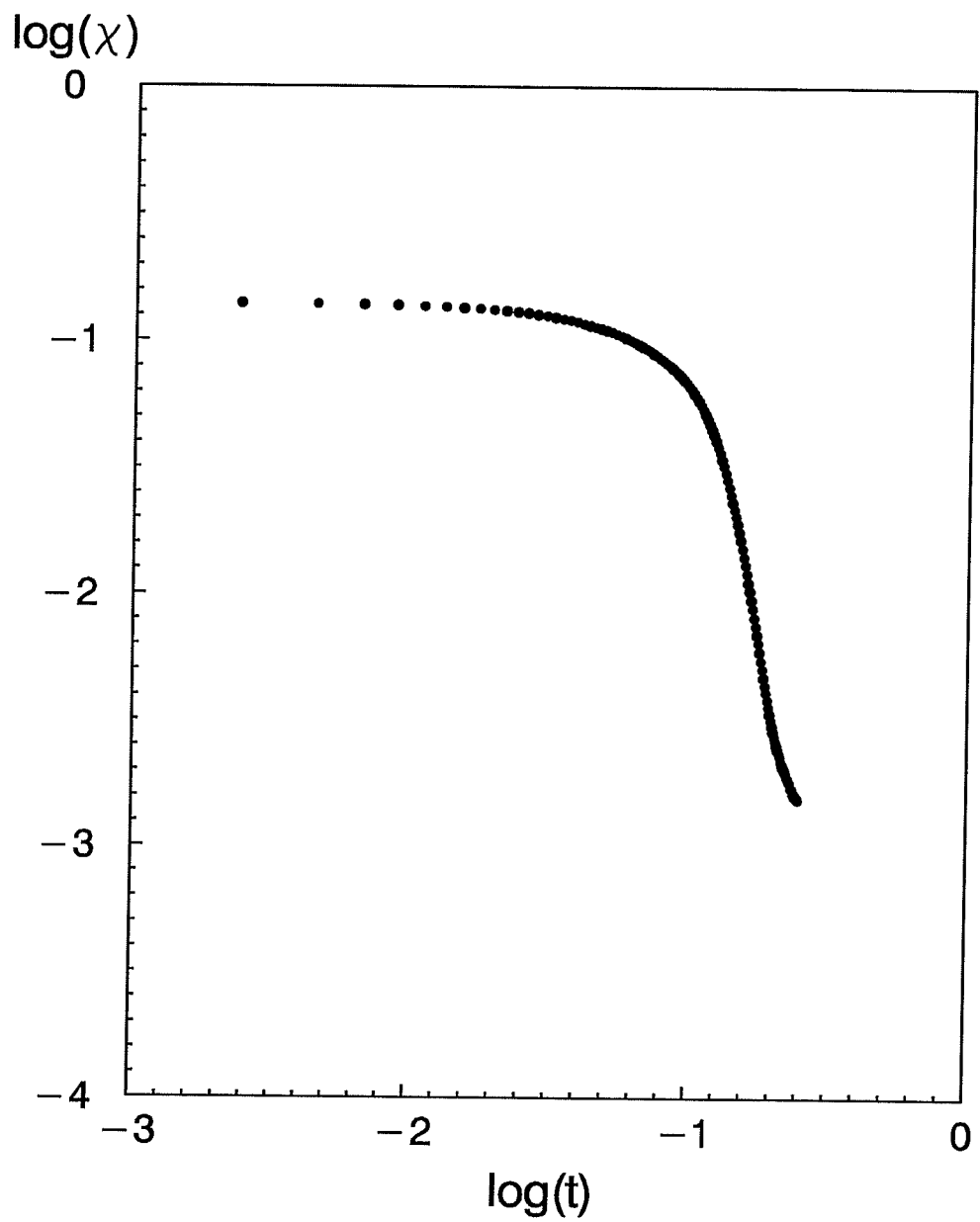


Figure 5.15: Zero field a. c. susceptibility of $\text{Ce}(\text{Fe}_{0.92}\text{Ru}_{0.08})_2$ vs. reduced temperature plotted on a double-logarithmic scale (above T_c)

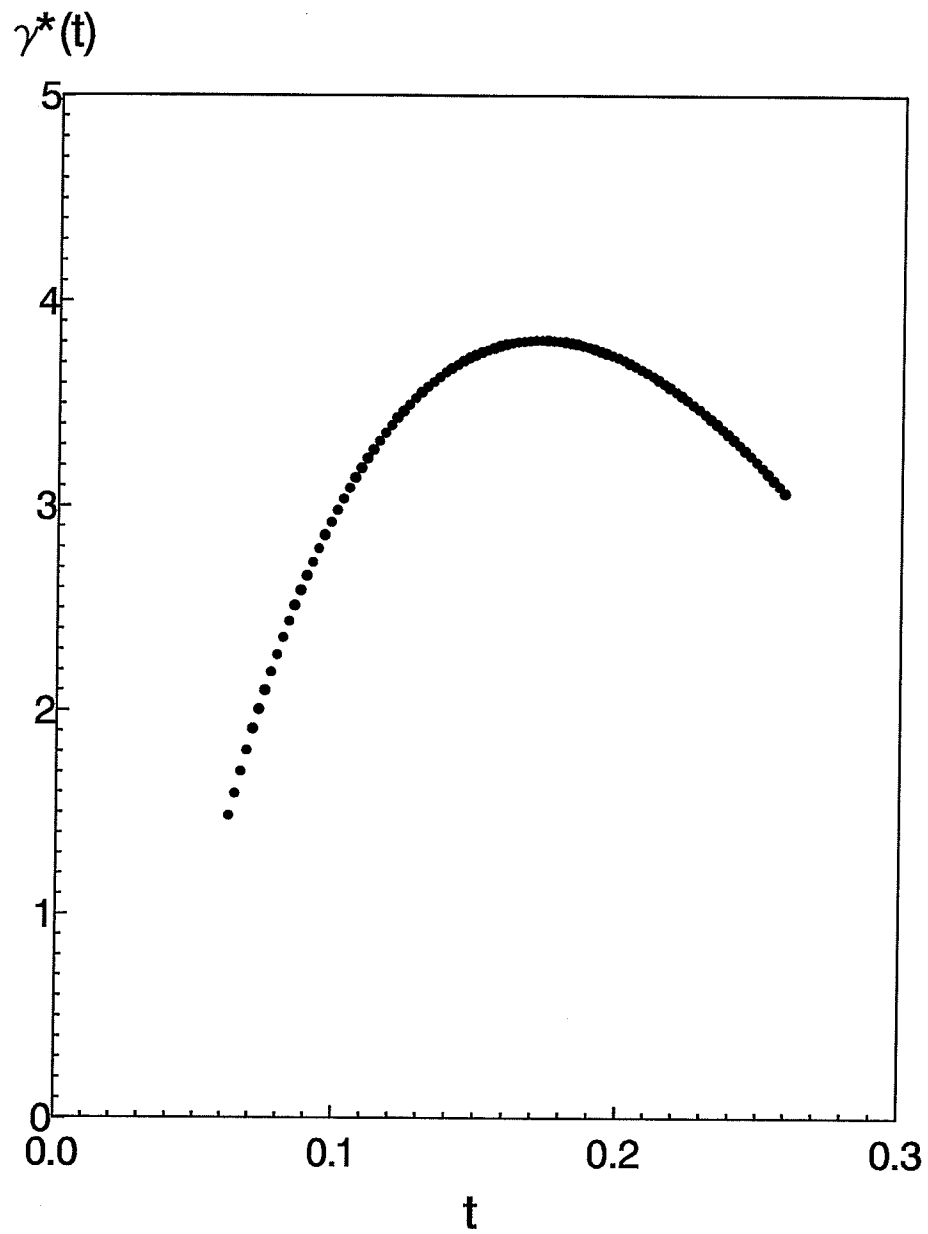


Figure 5.16: Effective susceptibility exponent $\gamma^*(t)$ vs. reduced temperature for $\text{Ce}(\text{Fe}_{0.92}\text{Ru}_{0.08})_2$, the peak occurs at $t_{max} = 0.18$, $\gamma^*_{max}(t) = 3.8$

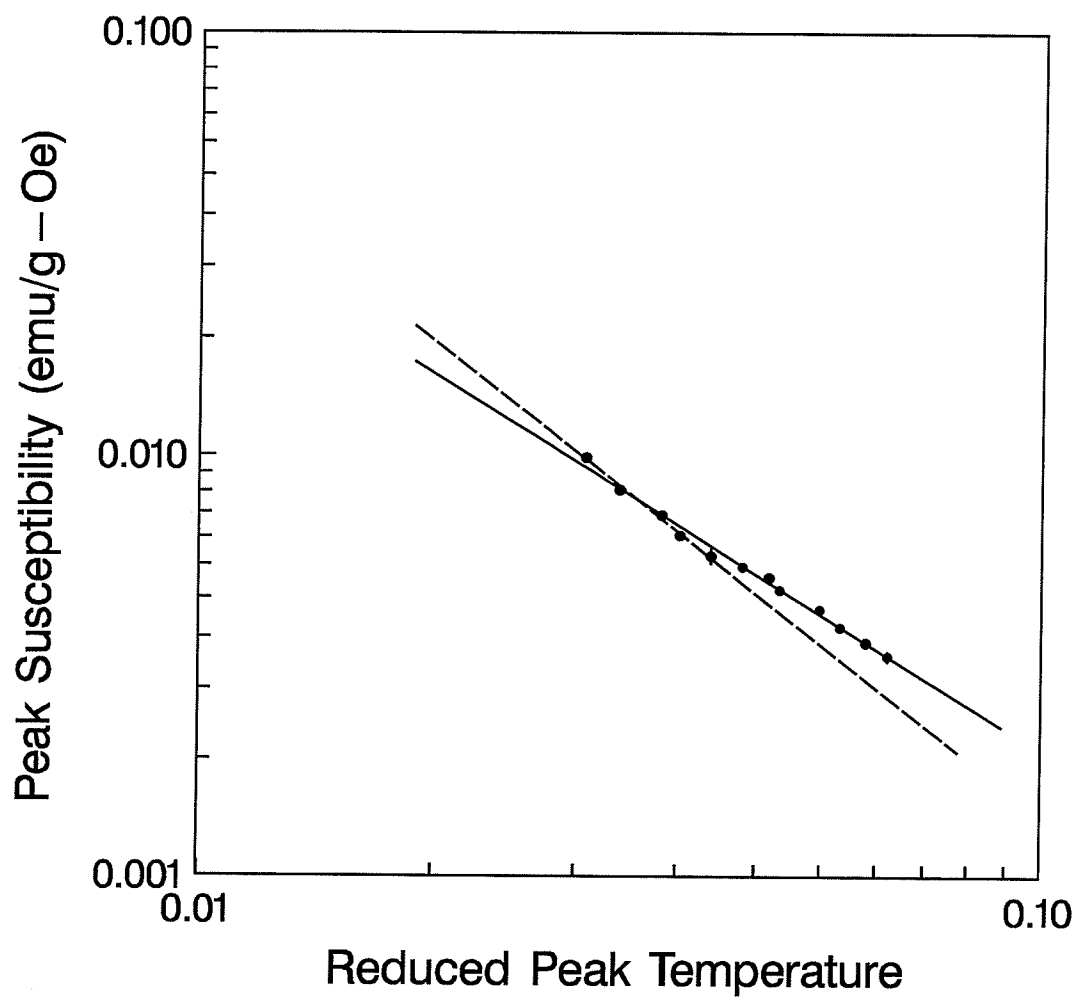


Figure 5.17: Peak susceptibility plotted against the reduced peak temperature for $\text{Ce}(\text{Fe}_{0.92}\text{Ru}_{0.08})_2$ on a double-log scale, the slope of the solid line is 1.22 ± 0.03 ; the low temperature value of the exponent γ is given by the dashed line which yields $\gamma = 1.5 \pm 0.1$, consistent with the Heisenberg result

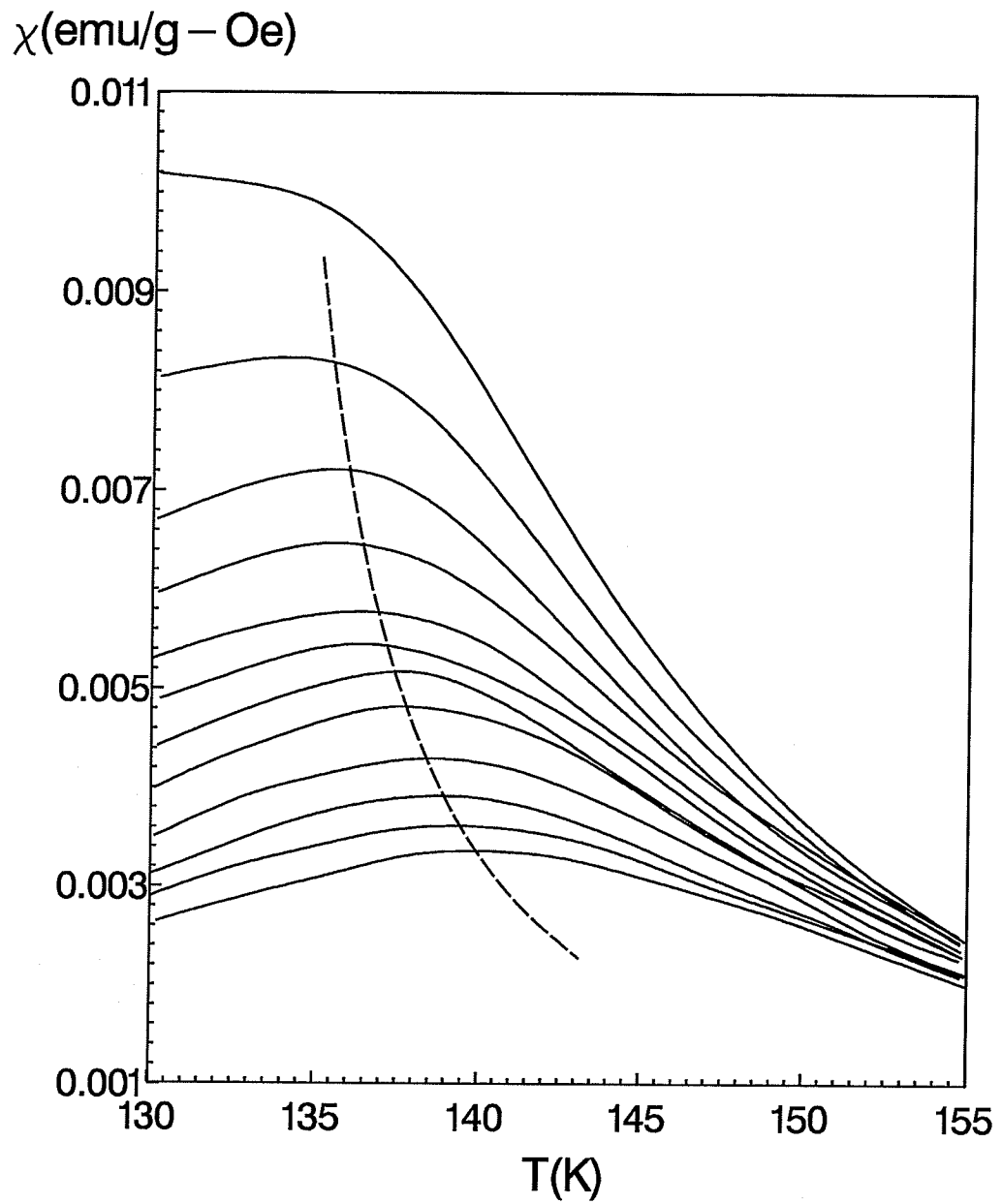


Figure 5.18: D. C. biasing field dependence of a. c. susceptibility of $\text{Ce}(\text{Fe}_{0.92}\text{Ru}_{0.08})_2$ near the critical temperature. The solid lines are temperature sweeps in different external fields and the dashed cross-over line illustrates the $\chi_m \sim t_m^{-7}$ relation.

Table 5.2: Nonlinear response of $\text{Ce}(\text{Fe}_{0.92}\text{Ru}_{0.08})_2$: $a_2(T)$ vs. T

Temperature T(K)	Slope $a_2(T)$ $\times 10^{-6}(\text{emu/g}\cdot\text{Oe}^3)$	Range (Oe^2)
117.8	12	120
118.4	22	
119.0	46	
119.8	59	50
120.5	72	
121.2	128	30
122.0	154	
122.8	152	
123.3	155	30
124.0	180	
124.8	196	
127.5	272	40
128.6	236	50
129.9	127	
131.1	24	60

$\gamma + \beta = 1.76 \pm 0.03$, respectively. The value of $\delta\gamma/(\delta - 1)$ is 1.73 ± 0.23 from the analysis. Again, the relation $\gamma + \beta = \delta\gamma/(\delta - 1)$ is satisfied within error limit.

5.3.3 Low Temperature Transition

The low temperature behaviour is again examined through the nonlinear response obtained from the plots of χ_t vs. H_i^2 at various temperatures and shown in fig. 5.22. The change in the slope is obvious as one approaches temperatures near the sharp rise in the zero field susceptibility; this is plotted in fig. 5.23, where the peak is estimated to be $2.7 \times 10^{-4} \text{emu/g}\cdot\text{Oe}^3$ at a temperature $T_f \simeq 127\text{K}$. Table 5.2 lists the slope ($a_2(T)$ coefficient, error is estimated to be $\pm 10 \times 10^{-6}$) as a function of temperature as well as the range of the fit for the $\text{Ce}(\text{Fe}_{0.92}\text{Ru}_{0.08})_2$ sample.

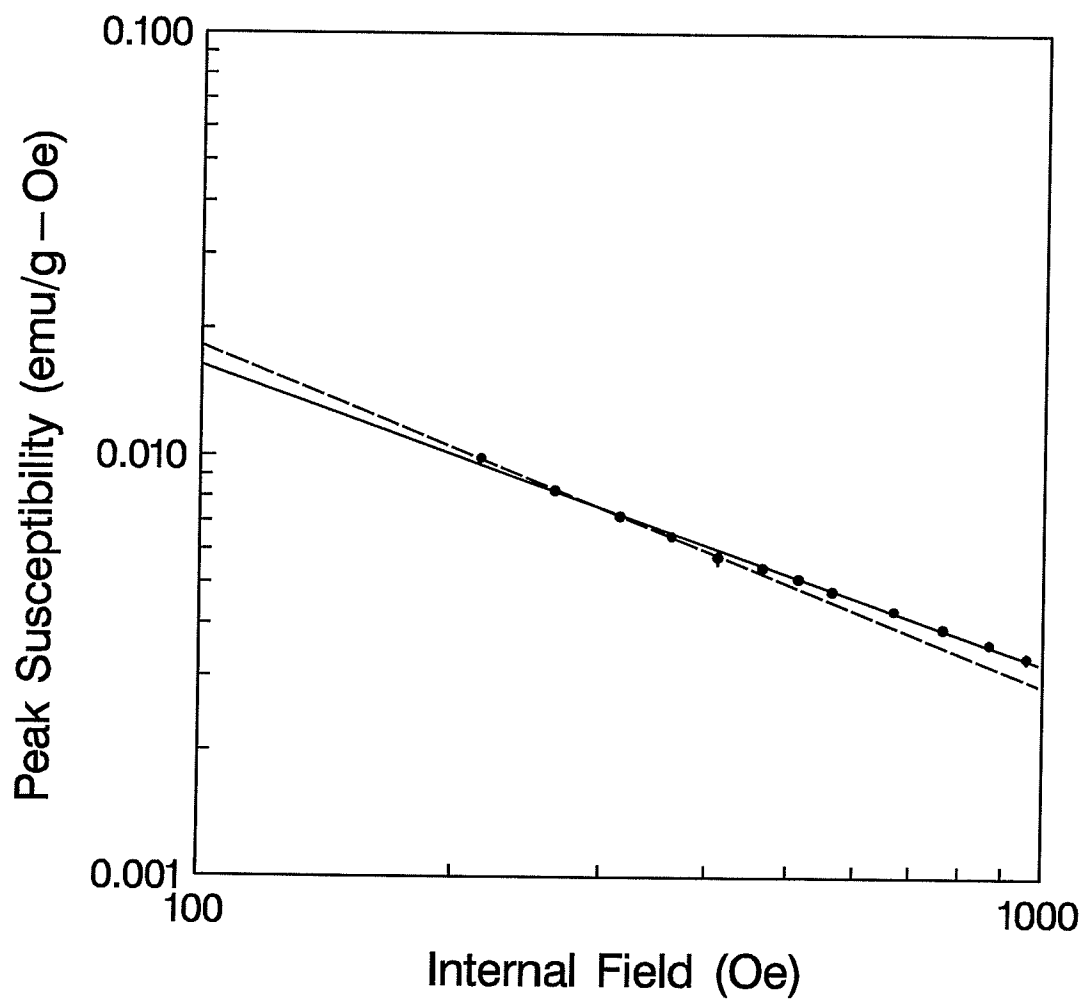


Figure 5.19: Peak susceptibility plotted against internal field on a double-logarithmic scale for $\text{Ce}(\text{Fe}_{0.92}\text{Ru}_{0.08})_2$. Where the error bars are not shown they are within the size of the dot. The solid line yields $\delta = 3.40 \pm 0.15$, and the broken line is a fit to low field points and yields $\delta = 5.1 \pm 0.6$

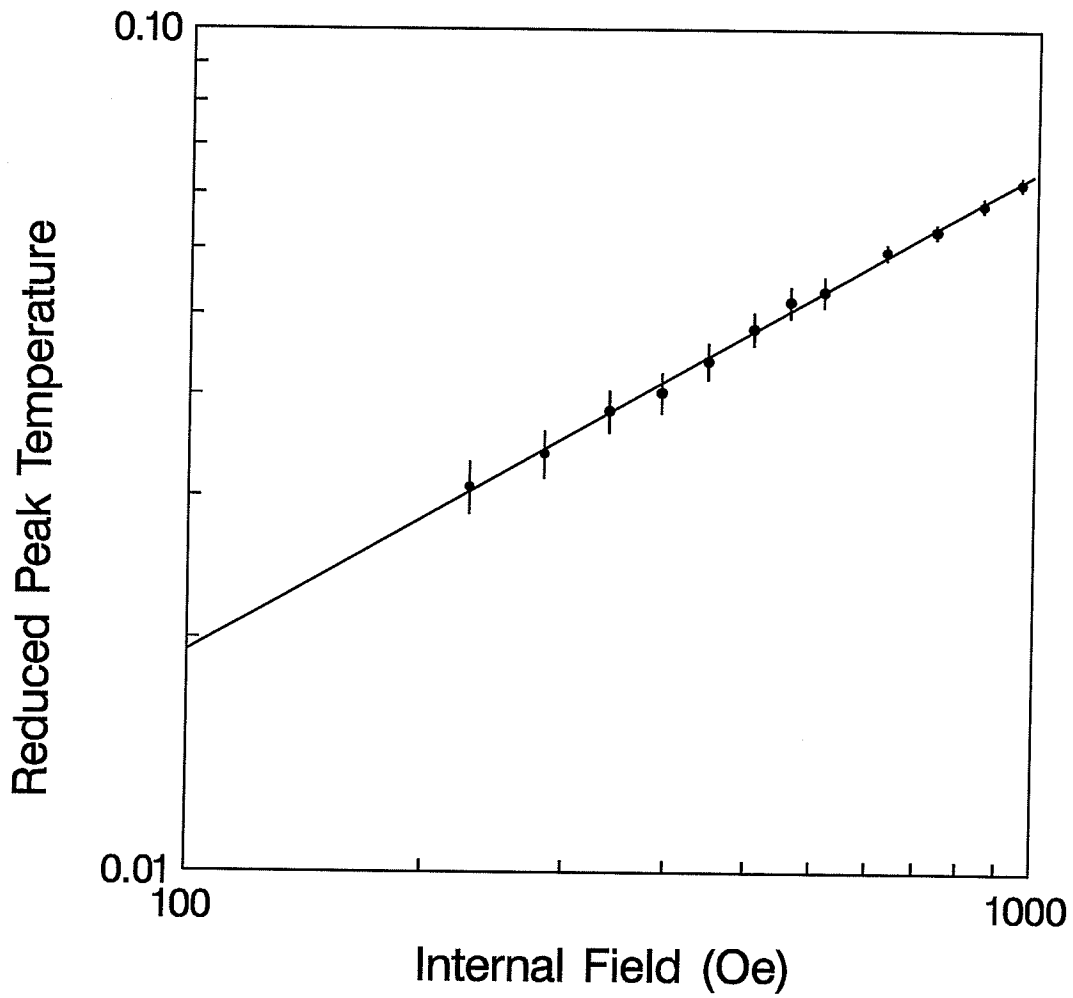


Figure 5.20: Reduced peak temperature plotted against internal field on a double-logarithmic scale for $\text{Ce}(\text{Fe}_{0.92}\text{Ru}_{0.08})_2$. The slope is $1/(\gamma + \beta)$, thus $(\gamma + \beta) = 1.76 \pm 0.03$, in agreement with the 3D Heisenberg prediction

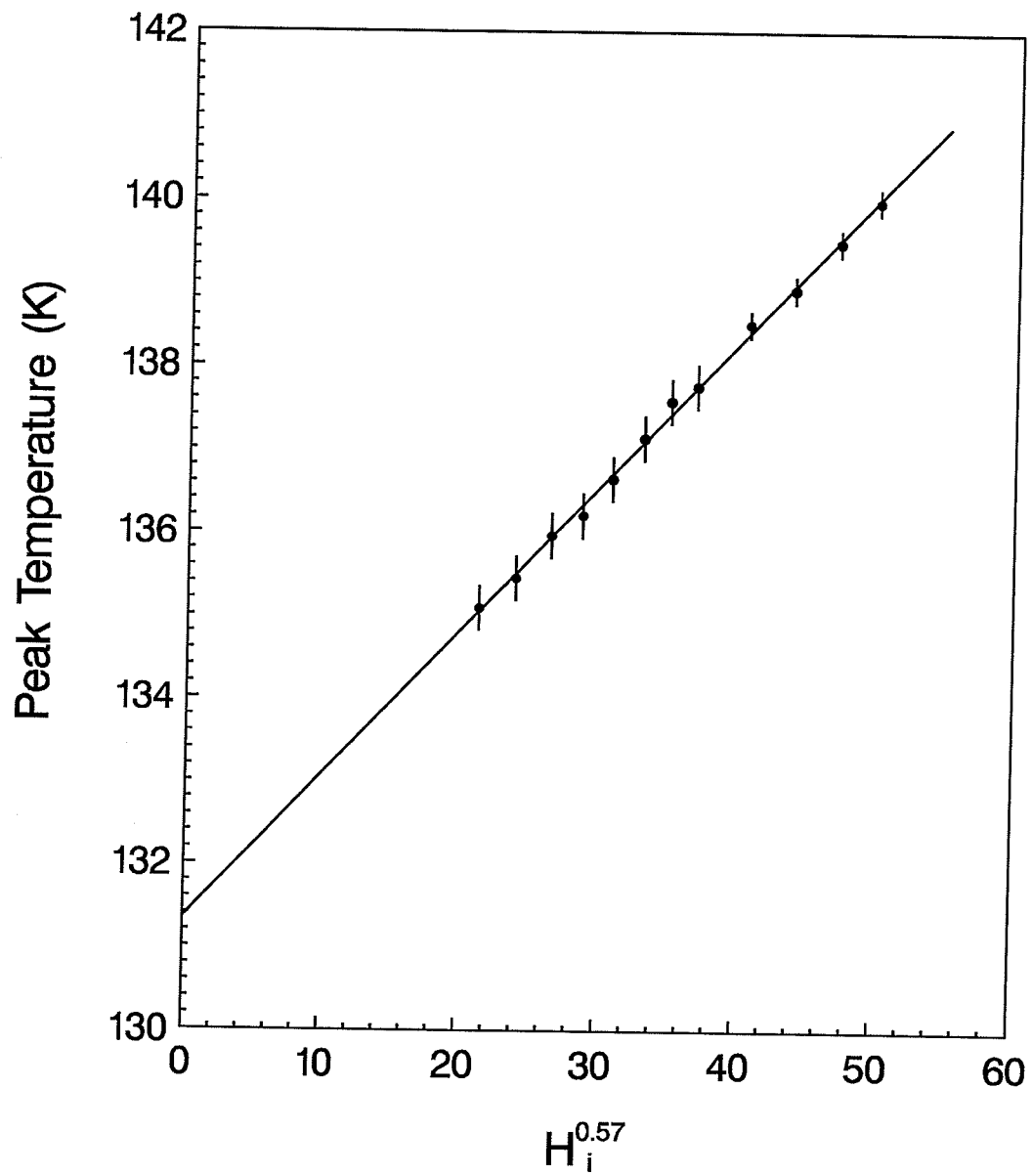


Figure 5.21: Peak temperature plotted against $H_i^{0.57}$ on linear scale for $\text{Ce}(\text{Fe}_{0.92}\text{Ru}_{0.08})_2$. The intercept at zero field yields $T_c = (131.4 \pm 0.4)K$

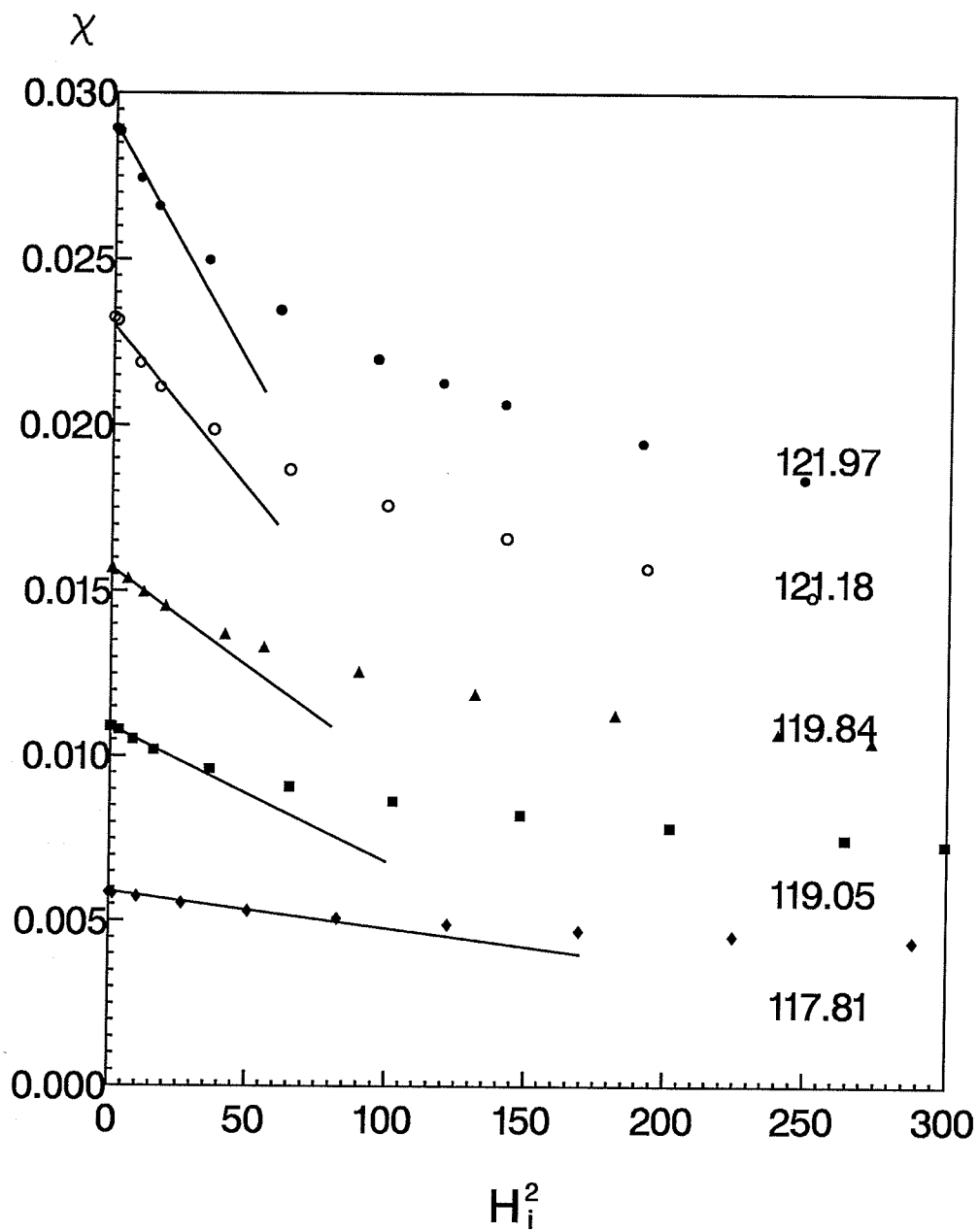


Figure 5.22: (a) Plot of susceptibility χ_t vs. H_i^2 for $\text{Ce}(\text{Fe}_{0.92}\text{Ru}_{0.08})_2$ at several different temperatures near the low temperature transition point in the range 117 ~ 122K. Errorbars are the size of the points.

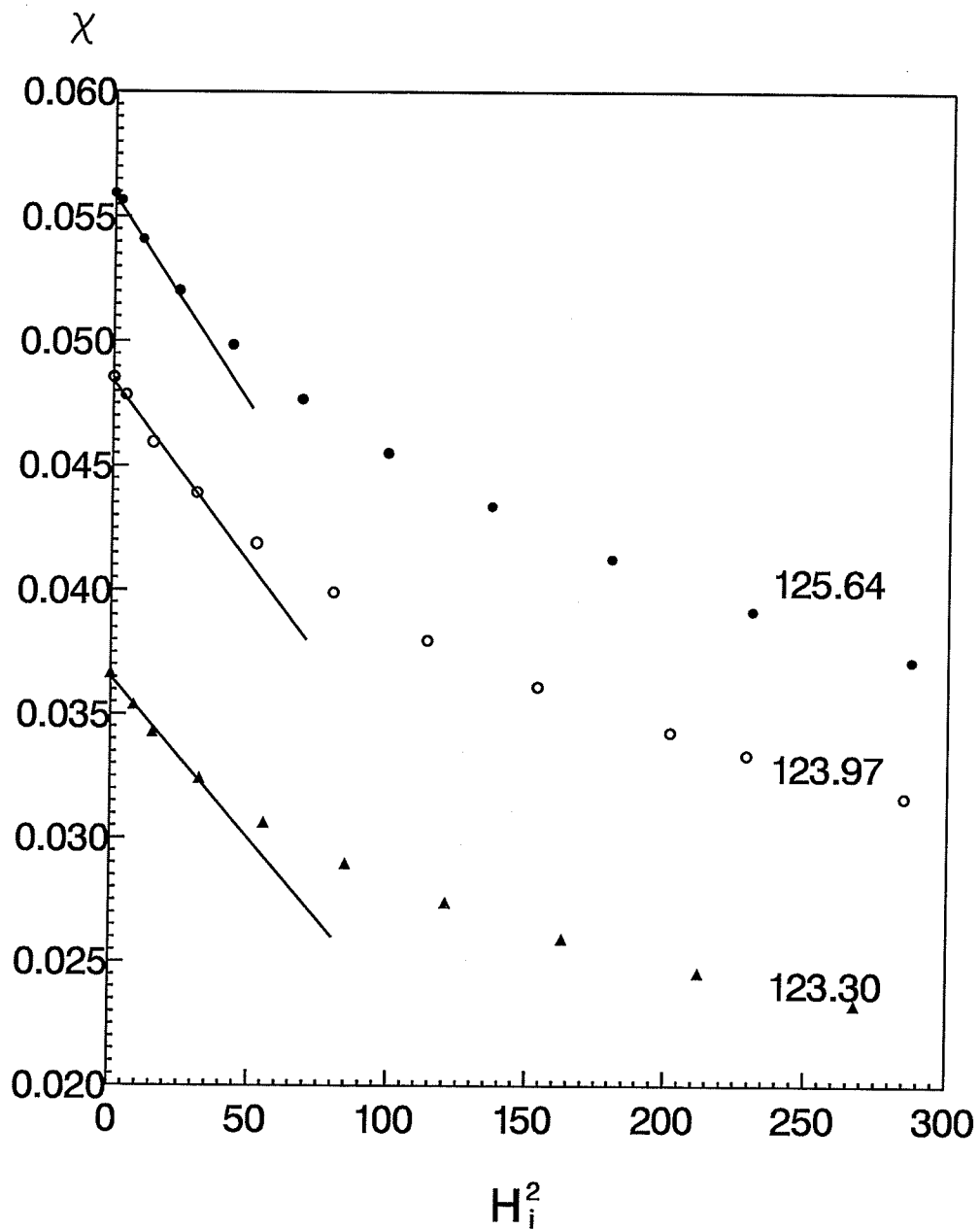


Figure 5.22: (b) Plot of susceptibility χ_t vs. H_i^2 for $\text{Ce}(\text{Fe}_{0.92}\text{Ru}_{0.08})_2$ at several different temperatures near the low temperature transition point in the range 123 ~ 126K. Errorbars are the size of the points.

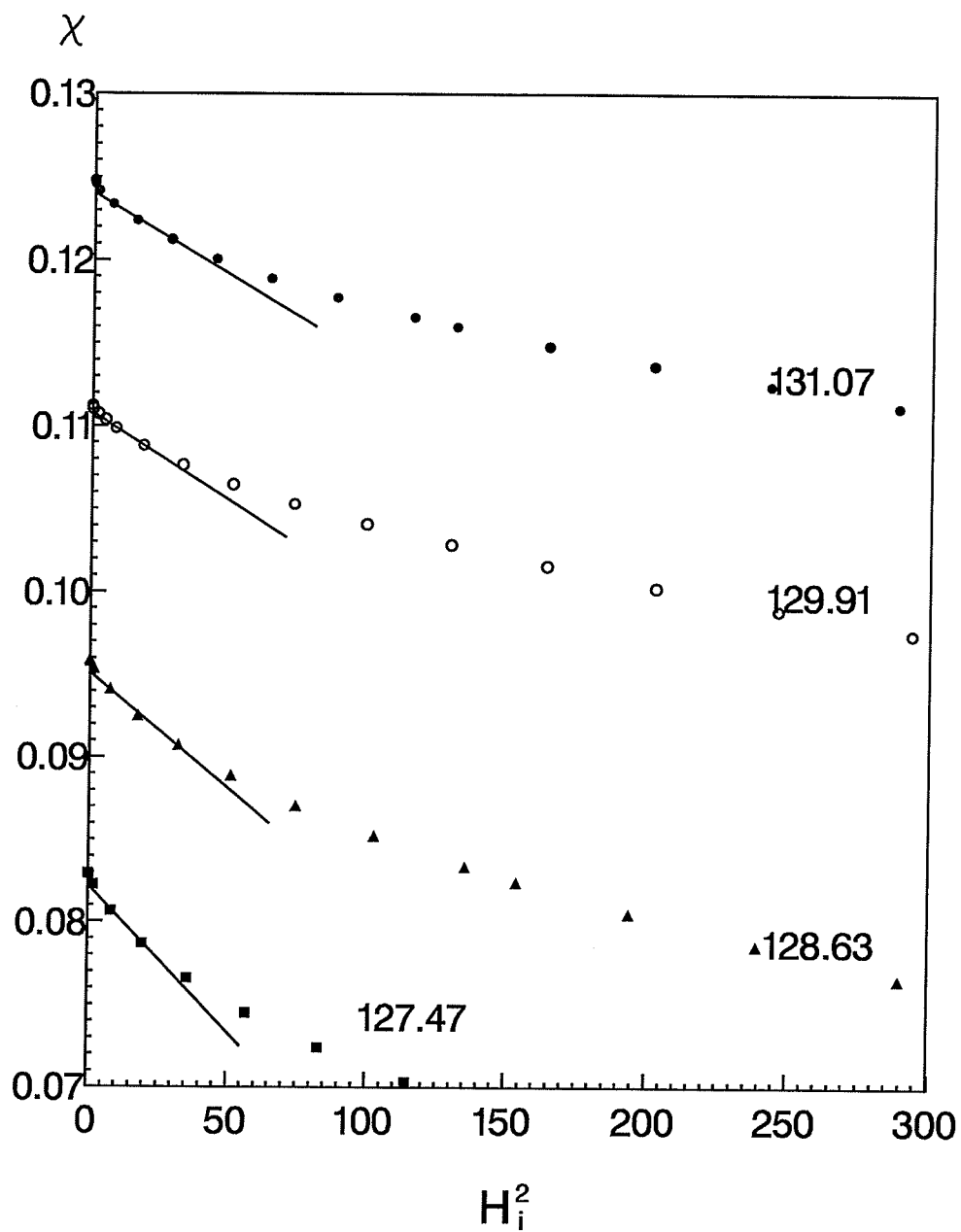


Figure 5.22: (c) Plot of susceptibility χ_t vs. H_i^2 for $\text{Ce}(\text{Fe}_{0.92}\text{Ru}_{0.08})_2$ at several different temperatures near the low temperature transition point in the range 127 ~ 132K. Errorbars are the size of the points.

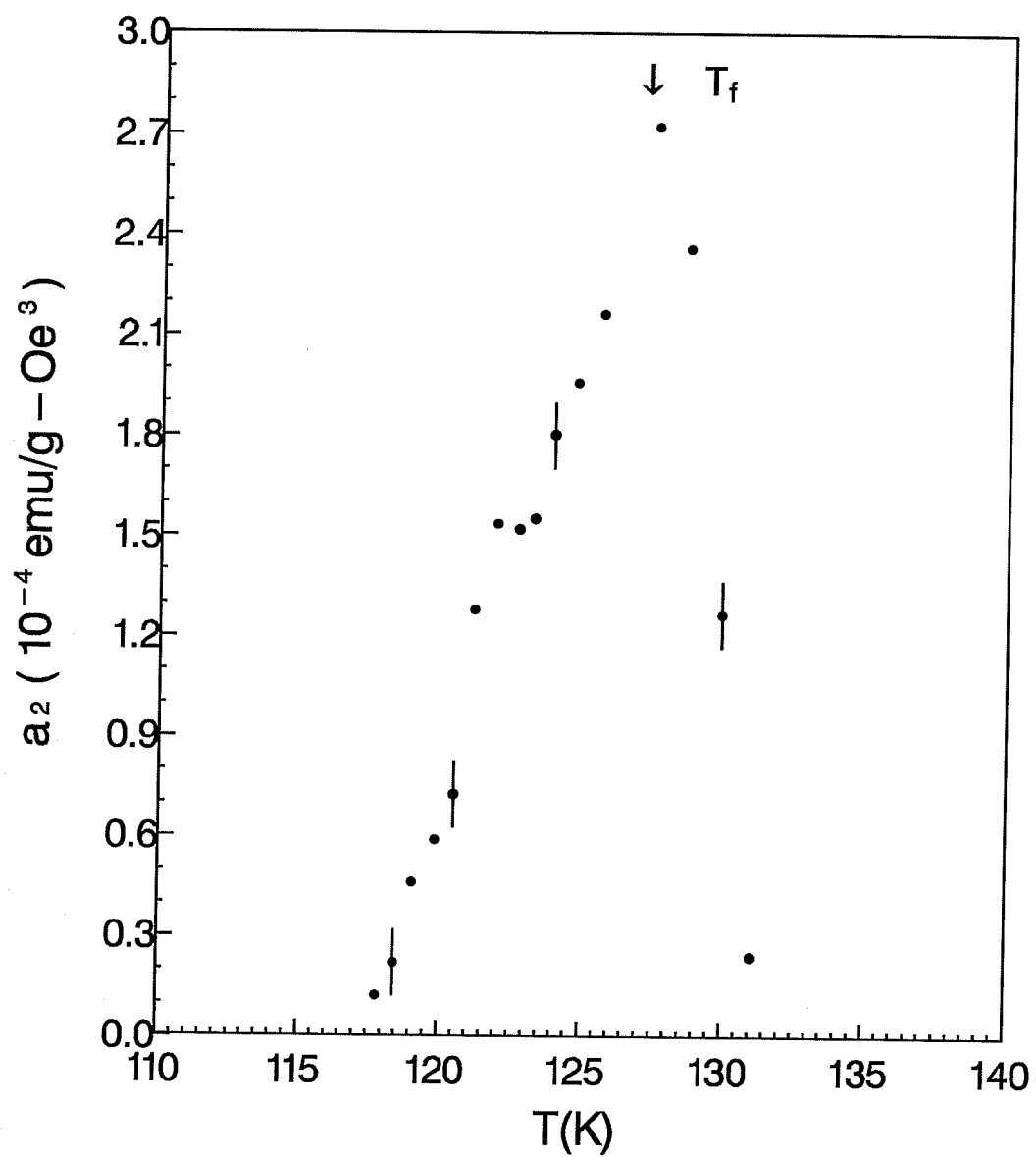


Figure 5.23: Temperature dependence of nonlinear coefficient a_2 for $\text{Ce}(\text{Fe}_{0.92}\text{Ru}_{0.08})_2$

Chapter 6

Discussion and Conclusion

6.1 A Summary

This section summarizes the experimental results obtained from detailed measurements on the samples $\text{Ce}(\text{Fe}_{0.93}\text{Ru}_{0.07})_2$, $\text{Ce}(\text{Fe}_{0.92}\text{Ru}_{0.08})_2$ and pure CeFe_2 ; the latter sample having been studied previously by Kunkel *et al* [7]. Results published by other authors for the $\text{Ce}(\text{Fe}_{1-x}\text{Ru}_x)_2$ compounds with compositions other than 7% and 8% are also included.

Some of the plots summarizing the results of the analysis of the present measurements are listed in table 6.1, with additional results listed in table 6.2.

Table 6.1: Summarizing plots

Figure label	Comments	Parameter
Fig. 6.1	$\log[\chi(0, t)]$ vs. $\log(t)$	
Fig. 6.2	$\gamma^*(t)$ vs. t	γ_{max}^*
Fig. 6.3	$\log(\chi_m)$ vs. $\log(t_m)$	$-\gamma$
Fig. 6.4	$\log(\chi_m)$ vs. $\log(H_i)$	δ
Fig. 6.5	$\log(t_m)$ vs. $\log(H_i)$	$(\gamma + \beta)$
Fig. 6.6	T_m vs. $H_i^{1/(\gamma+\beta)}$	T_c

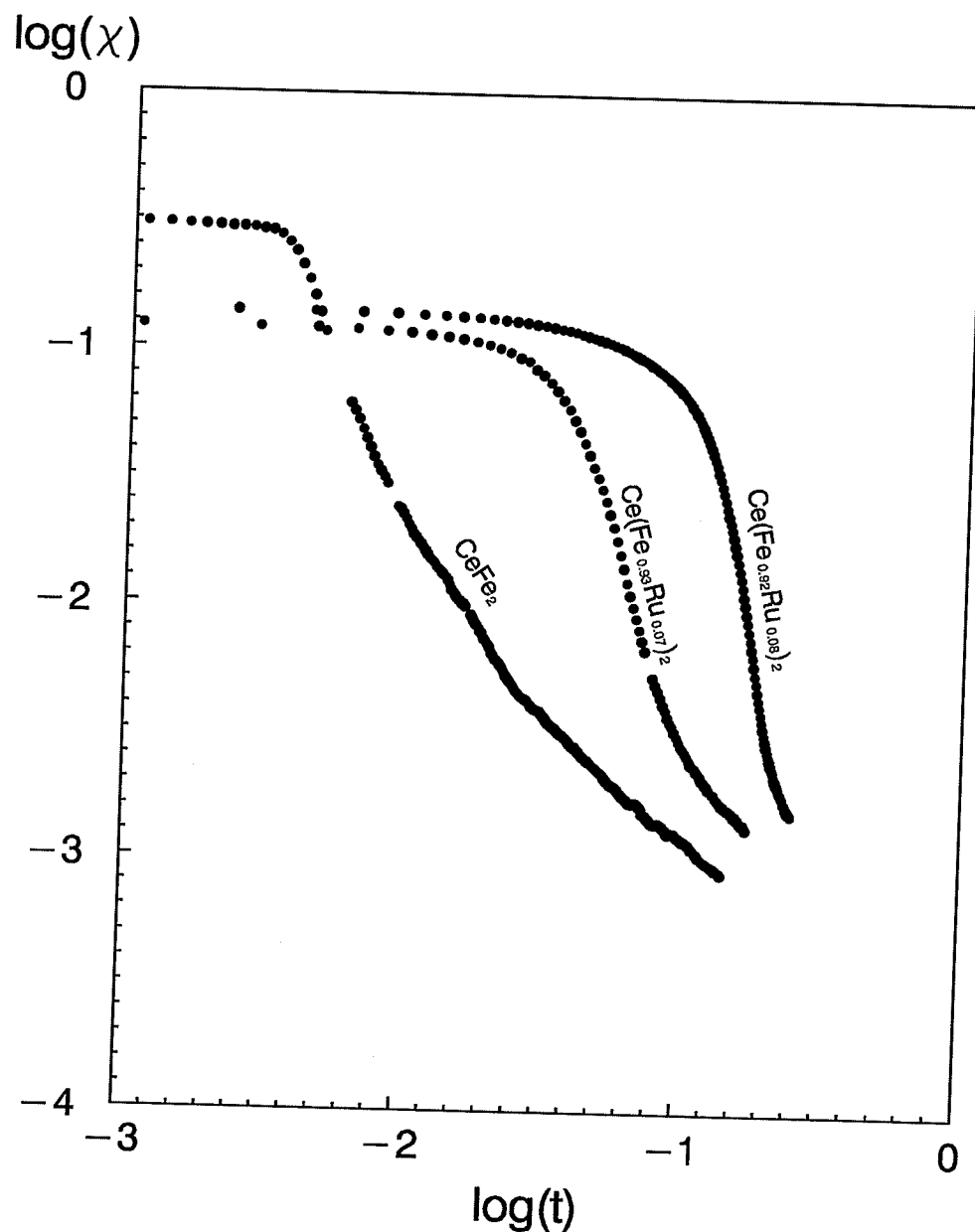


Figure 6.1: Zero field a. c. susceptibility vs. reduced temperature (above T_c) on double-log scale for CeFe_2 , $\text{Ce(Fe}_{0.93}\text{Ru}_{0.07})_2$ and $\text{Ce(Fe}_{0.92}\text{Ru}_{0.08})_2$; the severe flattening of these plots at low reduced temperature is due to the failure of the measured susceptibility (in all cases) to reach the demagnetizing limit (N^{-1}) because of anisotropy effects.

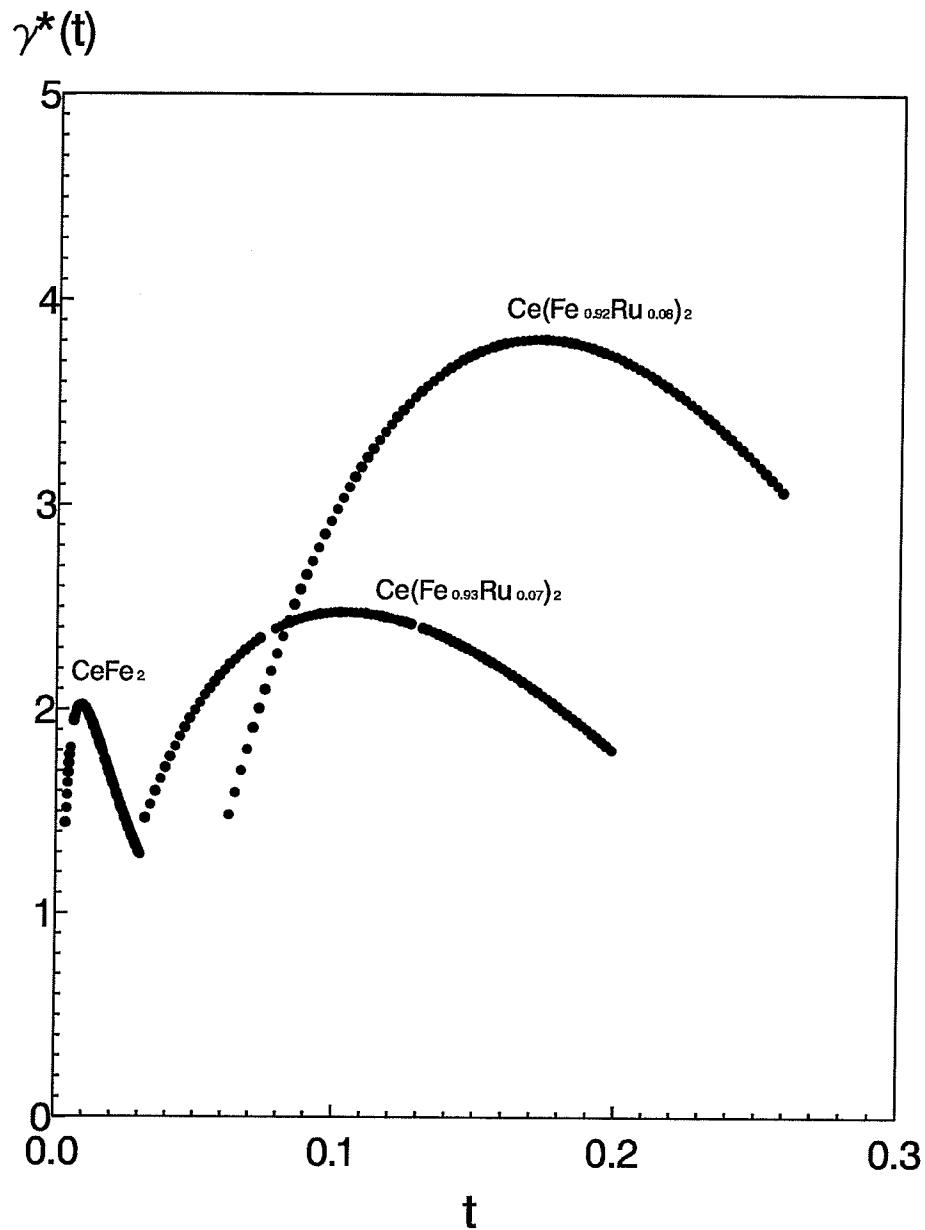


Figure 6.2: Effective susceptibility exponent $\gamma^*(t)$ vs. reduced temperature for CeFe_2 , $\text{Ce(Fe}_{0.93}\text{Ru}_{0.07})_2$ and $\text{Ce(Fe}_{0.92}\text{Ru}_{0.08})_2$. It is apparent that γ_{max}^* increases with increasing Ru concentration and the temperature at which the γ_{max}^* occurs also increases with increasing Ru concentration.

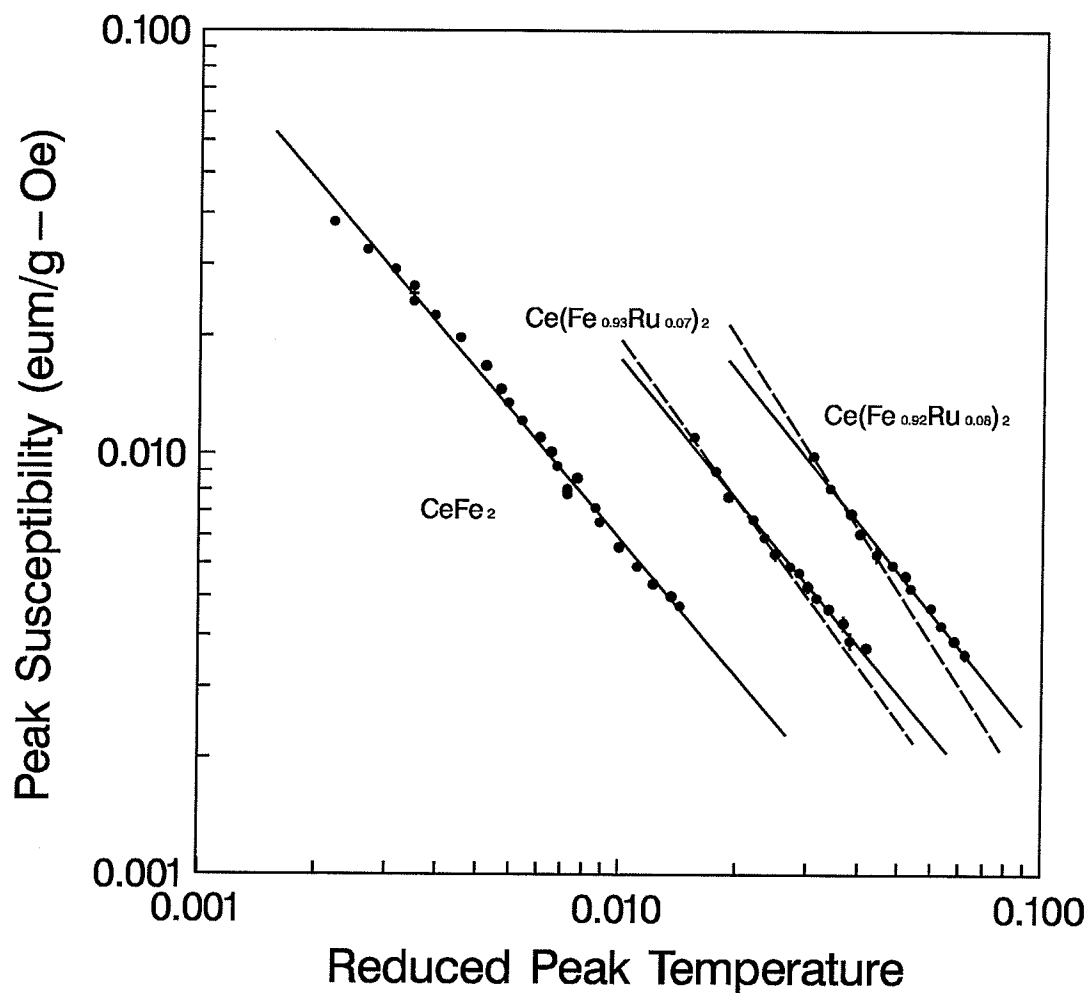


Figure 6.3: Peak susceptibility plotted against reduced peak temperature for CeFe_2 , $\text{Ce}(\text{Fe}_{0.93}\text{Ru}_{0.07})_2$ and $\text{Ce}(\text{Fe}_{0.92}\text{Ru}_{0.08})_2$ on a double-logarithmic scale, the slope of the broken lines yield γ values consistent with Heisenberg model predictions, the solid lines represent average γ values diminished somewhat by a possible crossover to mean field behaviour at higher temperature.

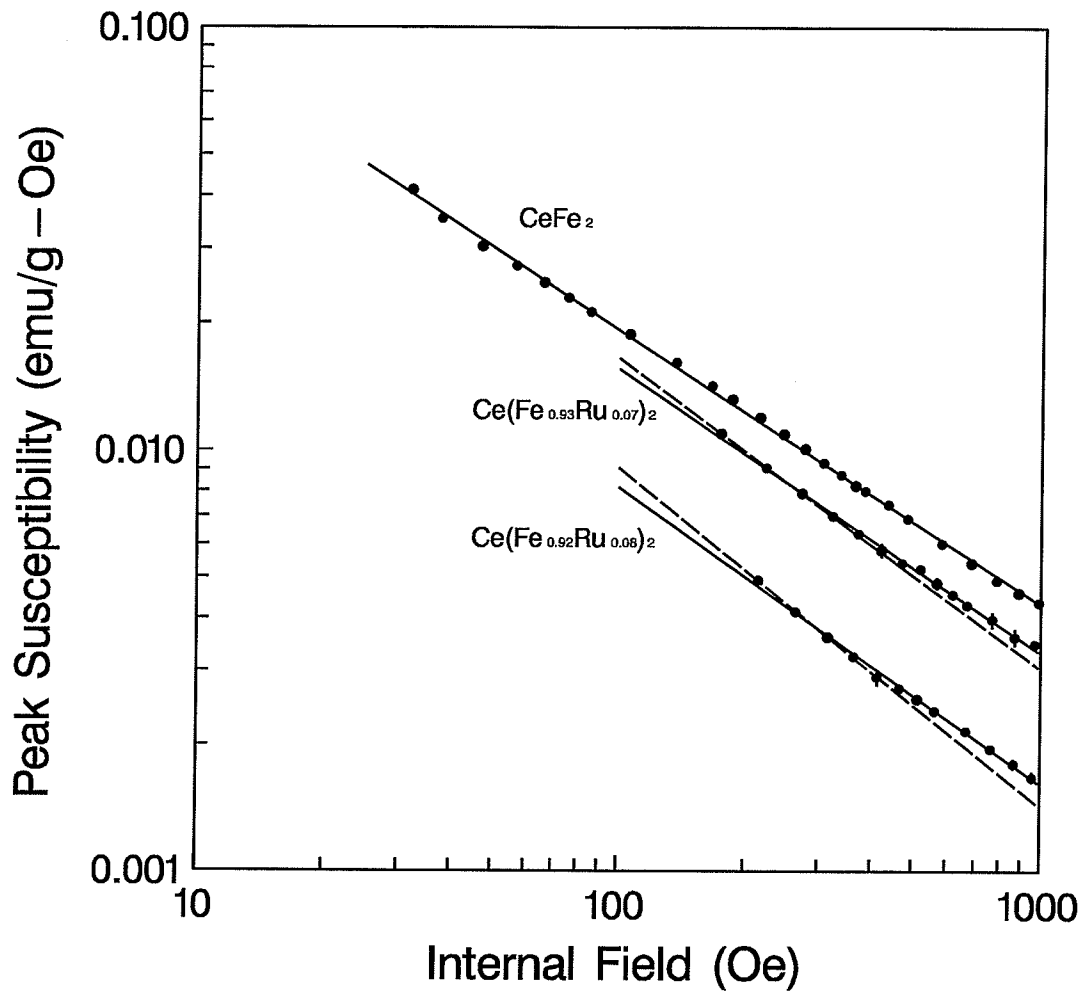


Figure 6.4: Peak susceptibility plotted against internal field on a double-logarithmic scale — the δ -plot — for CeFe_2 , $\text{Ce}(\text{Fe}_{0.93}\text{Ru}_{0.07})_2$ and $\text{Ce}(\text{Fe}_{0.92}\text{Ru}_{0.08})_2$. For clarity, the susceptibility of $\text{Ce}(\text{Fe}_{0.92}\text{Ru}_{0.08})_2$ has been shifted down by multiplying by a factor of 0.5

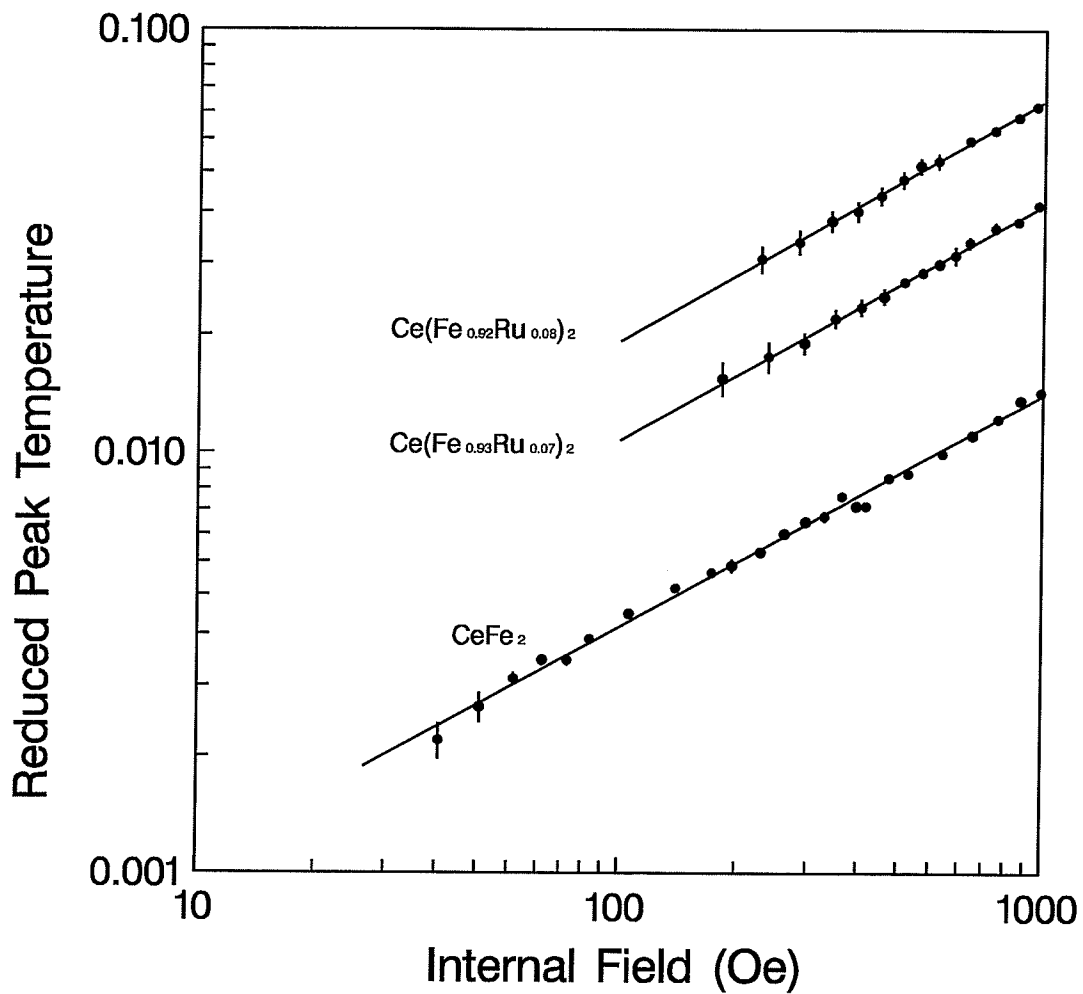


Figure 6.5: Reduced peak temperature plotted against internal field on a double-logarithmic scale — the cross-over plot — for CeFe_2 , $\text{Ce}(\text{Fe}_{0.93}\text{Ru}_{0.07})_2$ and $\text{Ce}(\text{Fe}_{0.92}\text{Ru}_{0.08})_2$. The lines drawn have a slope of 1.70, 1.79 and 1.76, respectively, consistent, within error, with the cross-over exponent predicted by the Heisenberg model.

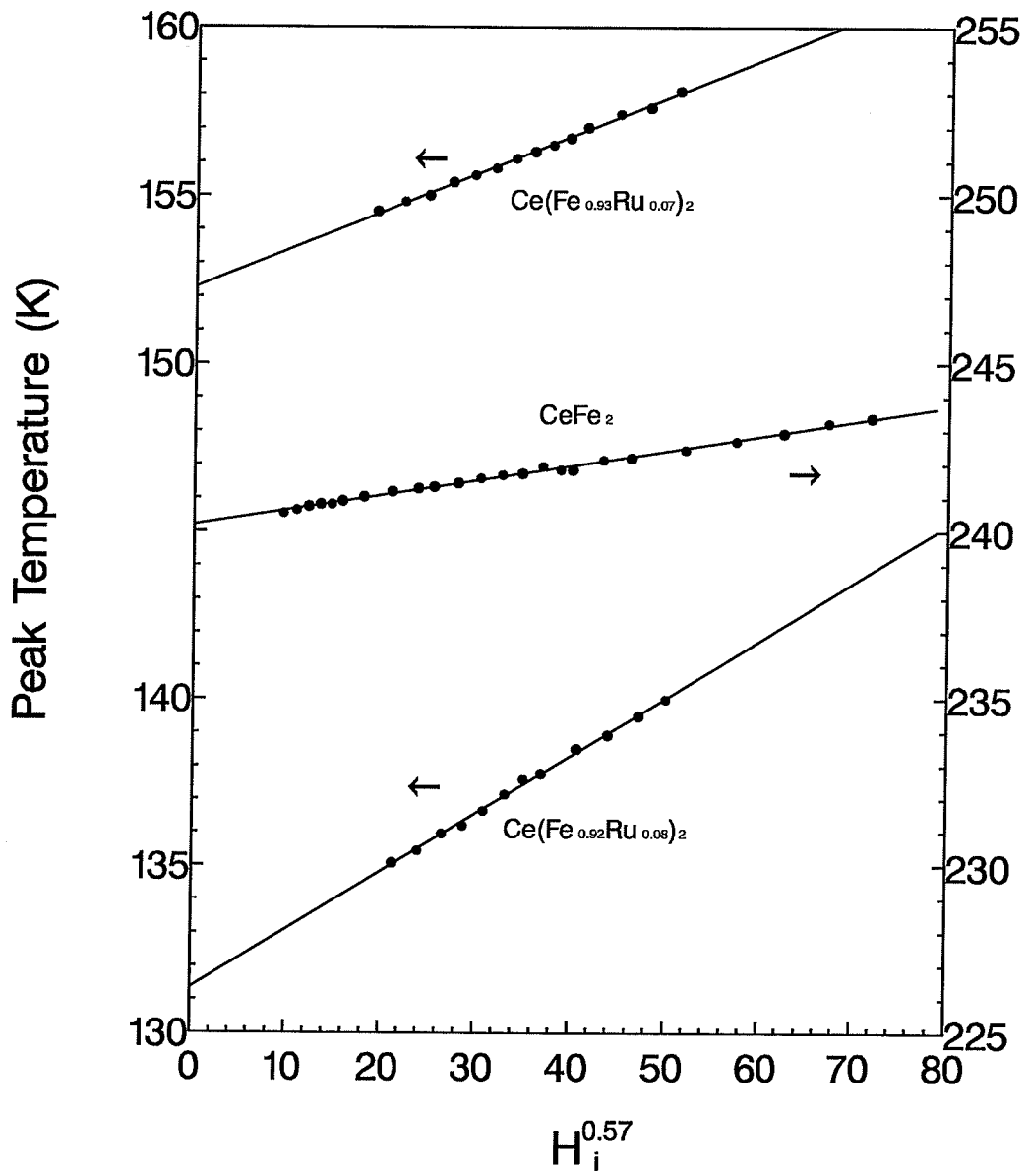


Figure 6.6: Peak temperature plotted against $H_i^{0.57}$ for $CeFe_2$, $Ce(Fe_{0.93}Ru_{0.07})_2$ and $Ce(Fe_{0.92}Ru_{0.08})_2$; the intercepts yields the corresponding values of T_c .

Table 6.2: Comparison of the results² of the data analysis for samples CeFe_2 , $\text{Ce}(\text{Fe}_{0.93}\text{Ru}_{0.07})_2$ and $\text{Ce}(\text{Fe}_{0.92}\text{Ru}_{0.08})_2$

Sample	CeFe_2	$\text{Ce}(\text{Fe}_{0.93}\text{Ru}_{0.07})_2$	$\text{Ce}(\text{Fe}_{0.92}\text{Ru}_{0.08})_2$
γ	1.18 ± 0.03	1.20 ± 0.03 (1.38 ± 0.05)	1.22 ± 0.03 (1.5 ± 0.1)
γ_{max}^*	2.0 ± 0.1	2.5 ± 0.1	3.8 ± 0.1
$t_{max}(\gamma)$	0.01 ± 0.001	0.1 ± 0.02	0.18 ± 0.02
δ	2.46 ± 0.02	3.08 ± 0.08 (3.8 ± 0.1)	3.40 ± 0.15 (5.1 ± 0.6)
$T_c(K)$	240.08 ± 0.01	152.3 ± 0.3	131.4 ± 0.4
$\gamma + \beta$	1.7 ± 0.1	1.79 ± 0.03	1.76 ± 0.03
$\delta\gamma/(\delta - 1)$	—	1.78 ± 0.16	1.73 ± 0.23
$T_f(K)$	—	117 ± 1	127 ± 1
a_{2max} (emu/g·Oe ³)	—	7×10^{-6}	2.7×10^{-4}

6.2 Discussion and Conclusion

6.2.1 The Ferromagnetic transition

Experimental results for the samples $\text{Ce}(\text{Fe}_{0.93}\text{Ru}_{0.07})_2$ and $\text{Ce}(\text{Fe}_{0.92}\text{Ru}_{0.08})_2$ have confirmed a well defined phase transition from paramagnetic to ferromagnetic order near the Curie temperature T_c through the observation of structure associated with critical fluctuations at a second order phase transition. The field and temperature dependence of the cross-over line is studied in detail, in search of a set of power law exponents describing the magnetic behaviour in the critical region.

Spin-orbit induced anisotropy, however, precludes the estimate of reliable values for asymptotic exponents (except perhaps for γ), although the Curie temperature can be determined quite accurately. For all the alloys examined, a power law behaviour with a unique exponent is not observed; the double-log plots exhibit considerable curvature and straight line fits are drawn to give high and low field (reduced temperature) effective exponents which are tabulated in table 6.2. The critical exponents δ , and γ , as suggested by low field and low reduced temperature fits, respectively, suggest agreement with 3D-Heisenberg model parameters. This may imply the magnetic moments are rather localized and the exchange coupling are limited to near neighbours.

A comparison of the experimental data for the $\text{Ce}(\text{Fe}_{1-x}\text{Ru}_x)_2$ samples mentioned here, namely CeFe_2 , $\text{Ce}(\text{Fe}_{0.93}\text{Ru}_{0.07})_2$ and $\text{Ce}(\text{Fe}_{0.92}\text{Ru}_{0.08})_2$, and that available from other authors [8] [9], shows the following systematics:

(1) T_c decreases with increasing Ru concentration at a rate of approximately $-11\text{K}/\text{at.}\% \text{Ru}$ (see fig. 6.8). With higher Ru substitution, the exchange bond disor-

²The numbers listed in parenthesis for δ and γ are from low field (reduced temperature) fits.

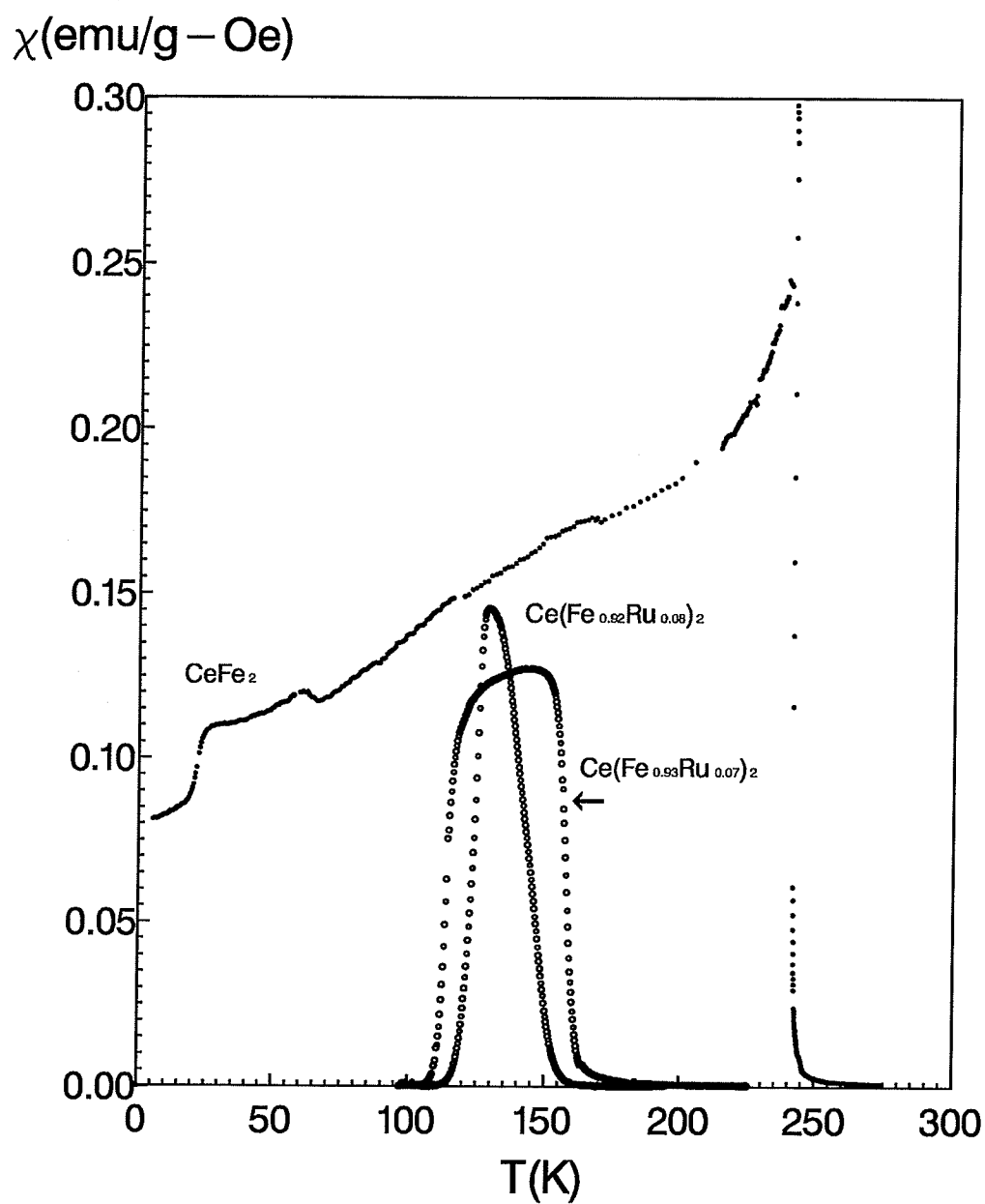


Figure 6.7: Zero field susceptibility for CeFe_2 , $\text{Ce}(\text{Fe}_{0.93}\text{Ru}_{0.07})_2$ and $\text{Ce}(\text{Fe}_{0.92}\text{Ru}_{0.08})_2$

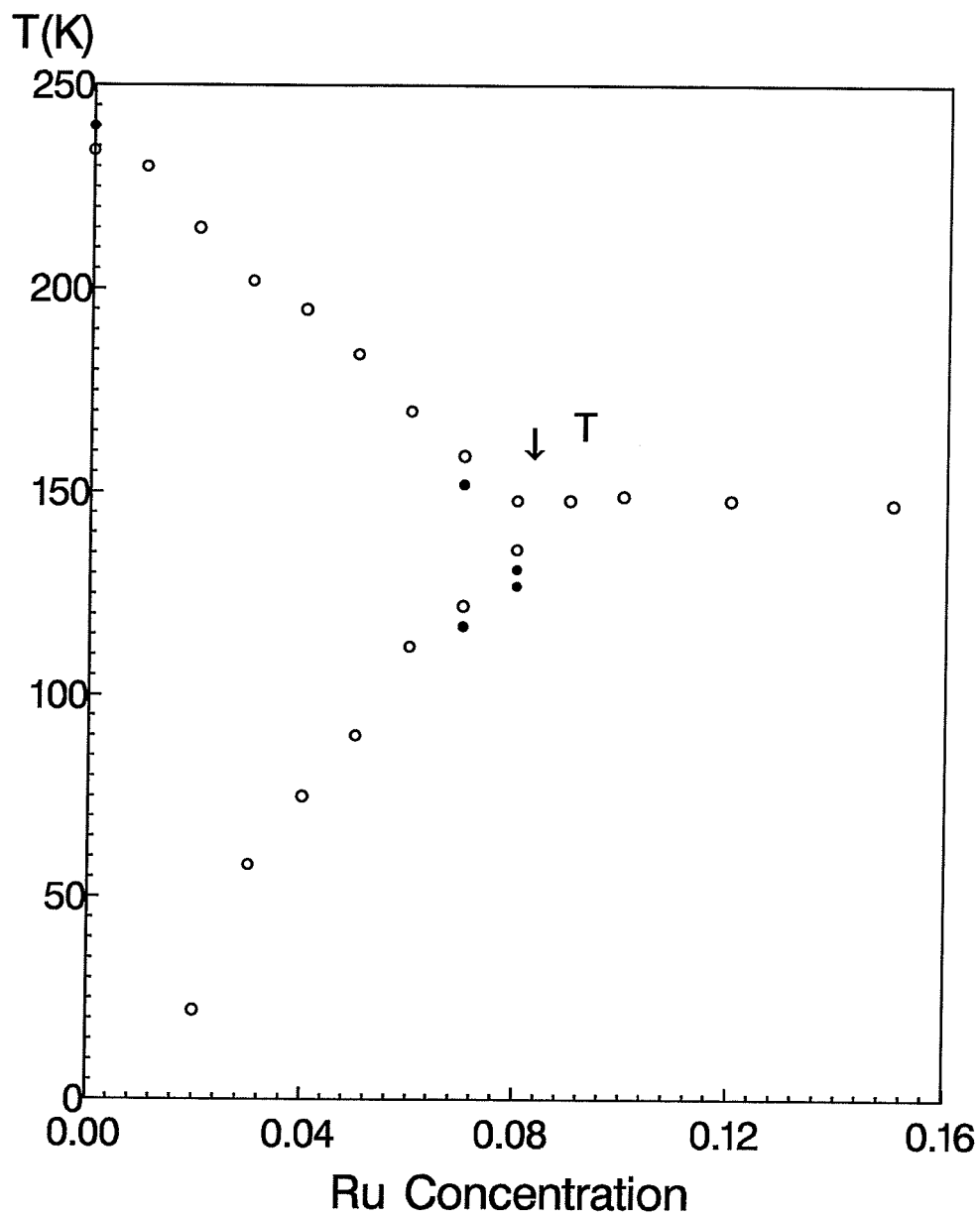


Figure 6.8: Phase diagram of Ce(Fe_{1-x}Ru_x)₂ compounds

der increases, magnetic fluctuations in the critical region become stronger thus making it more difficult to form a long range order and T_c drops. This result is consistent with that predicted for the ferromagnetic phase of a S-K model; as the ratio of the first to second moments of the exchange bond distribution ($\eta = J_0/J_1$) decreases (section 2.6), the value of T_c decreases and, in fact, T_{sg} (or T_f) $\propto J$ increases.

(2) The transition boundaries exhibited in the zero field susceptibility also become increasingly gradual with increasing Ru substitution (see fig. 6.7), making it more difficult to find the critical temperature.

(3) A non-monotonic variation in the effective susceptibility exponent γ^* is considered to be a characteristic of systems with exchange bond disorder [7]. A larger γ_{max}^* indicates greater bond disorder. Although an excessively large γ_{max}^* is perhaps also partly a consequence of the estimated T_c being too low (section 5.3.1.), this is expected to be a relatively minor effect which is supported by the systematic behaviour observed in both γ_{max}^* and t_{max} . It is apparent that γ_{max}^* as well as the temperature at which the maximum effective γ occurs, t_{max} , both increase with increasing Ru concentration. A similar behaviour has been observed for PdNi [3] for moderate concentrations and also FeNi in a recent report by Kaul *et al* [27]. A plot of peak susceptibility vs. peak temperature (fig. 6.3), however, does yield a value of γ consistent with the predictions of the Heisenberg model. It should be noted that in each case the range of reduced temperature plotted lies well below that where γ^* rises to a maximum due to magnetic disorder.

(4) Effective δ -value decreases with increasing field. This behaviour is again consistent with that suggested by models incorporating exchange bond disorder [26]. Such behaviour has been reported previously, for instance, FeMn [25], and PdFe [4], although the asymptotic value remains unchanged. However, due to the existence

of strong anisotropy in the present samples, it is not possible to observe the critical peaks in fields lower than $200Oe$, preventing the asymptotic exponent values from being revealed. At lower fields, however, the effective exponent δ^* increases (see table 6.2 and fig. 6.4) substantially for 7% and 8% Ru samples, thus not precluding asymptotic values of δ that agree with the Heisenberg model predictions. In fact, for the 8%Ru sample the low field value of δ^* is in agreement with the Heisenberg prediction to within the estimated experimental error.

6.2.2 The Low Temperature Transition

The low temperature transition is studied using the non-linear response. A peak in the non-linear response had previously been seen in pure spin-glass transitions, as well as in reentrant spin-glass transitions. In the present work anomalies were observed in the nonlinear susceptibility of $Ce(Fe_{0.93}Ru_{0.07})_2$ and $Ce(Fe_{0.92}Ru_{0.08})_2$, which are believed to be antiferromagnetic at low temperature, although they do not diverge as expected. The lower transition temperature T_f increases with Ru concentration, at a rate of approximately $dT_f/dx \simeq +15K/at.\%Ru$.

6.2.3 Phase Diagram

The ground state of $Ce(Fe_{1-x}Ru_x)_2$ is dependent on the temperature and the Ru concentration. Fig. 6.7 shows the zero field susceptibility of all three samples, with the phase boundaries identified by sudden changes (steps) in the magnetic response. Roy *et al* [8] studied the Ru substituted system using the method of zero field a. c. susceptibility, and together with additional data obtained from techniques such as resistivity, obtained a phase diagram for the $Ce(Fe_{1-x}Ru_x)_2$ compounds, shown in fig. 6.8, in which the dots represent our work and the circles represent that of Roy *et al*.

According to the diagram, the ferromagnetic region “shrinks” as the Ru composition increases, and is totally lost when x is greater than 0.09; the material can then have only two states, the paramagnetic and antiferromagnetic states. In fact the system at this point has just passed through the tri-critical point (point “T” in phase diagram).

6.2.4 Conclusion

From the present experiment and analysis, we reach the following conclusions:

The high temperature transition: paramagnetic-ferromagnetic state. The critical exponents are obtained through conventional scaling approach. Although due to large anisotropy of the material, it is not possible to induce the exponent values at low field and low temperature, experimental data suggest that they may asymptotically approach 3D-Heisenberg predictions.

The low temperature transition: The anomaly in nonlinear response verifies the phase transition, concluded to be from ferromagnetic to antiferromagnetic state by neutron diffraction data.

Upon cooling, the material undergoes sequential phase transitions from a paramagnetic to ferromagnetic to an antiferromagnetic state. With the substitution of Ru at a concentration under 0.09, the above described transition sequence is maintained, but a shift in the transition temperatures is observed, reducing the temperature range of the ferromagnetic (ground state) region.

It is evident that the rare earth compound, CeFe_2 , is near a type of instability, and a small level of substitution of Fe with transition metal elements (d electron) can cause its magnetic properties to change considerably. With increasing Ru concentration, $x \rightarrow 0.08$, the $\text{Ce}(\text{Fe}_{1-x}\text{Ru}_x)_2$ system approaches the tri-critical point, along with dramatically increasing disorder.

Whether the anomaly in the nonlinear response can be considered as a characteristic behaviour at an antiferromagnetic transition is not possible to state at the present time. A similar anomaly has been observed in reentrant spin-glass systems. From the existing data it is not clear if there are any features that could distinguish the antiferromagnetic from the the spin-glass phase using the non-linear response. The anomaly in the ferromagnetic-antiferromagnetic transition is considerably larger in amplitude, however. A non-linear analysis of a pure paramagnetic to antiferromagnetic transition (for instance, $\text{Ce}(\text{Fe}_{1-x}\text{Ru}_x)_2$ with $x > 0.09$) would be of considerable use and interest. The present work represents an important contribution in the establishment of the non-linear response as a means of distinguishing systems with a truly reentrant phase transition from systems which merely display interesting magnetic responses resulting from macro- magnetic anisotropy effects.

Appendix A

Homogeneous Function

A single variable function $f(x)$ is by definition homogeneous if for all values of the parameter λ

$$f(\lambda x) = g(\lambda)f(x) \quad (\text{A.1})$$

The function $g(\lambda)$ can be shown to take the form $g(\lambda) = \lambda^p$, where the parameter p is a constant called the degree of homogeneity. Similarly if a function with a vector variable is homogeneous, then

$$f(\lambda \mathbf{r}) = g(\lambda)f(\mathbf{r}) \quad (\text{A.2})$$

where \mathbf{r} is an n -dimensional vector represented by (x_1, x_2, \dots, x_n) . Equation (A.2) is equivalent to

$$f(\lambda x_1, \lambda x_2, \dots, \lambda x_n) = g(\lambda)f(x_1, x_2, \dots, x_n) \quad (\text{A.3})$$

This can be regarded as a multi-variable homogeneous function. A more general form for the homogeneous function is that the degree of homogeneity may be different for all the dimensions

$$f(\lambda^{b_1} x_1, \lambda^{b_2} x_2, \dots, \lambda^{b_n} x_n) = g(\lambda)f(x_1, x_2, \dots, x_n) \quad (\text{A.4})$$

$$= \lambda^p f(x_1, x_2, \dots, x_n) \quad (\text{A.5})$$

for which we can say that $f(x_1, x_2, \dots, x_n)$ is a generalized homogeneous function, where b_i ($i = 1, 2, \dots, n$) are fixed constants determined by the function $f(\mathbf{r})$. Again $g(\lambda) = \lambda^p$ is verified. Letting $\lambda' = \lambda^p$, so that $\lambda = (\lambda')^{1/p}$, the above can be written as

$$f[(\lambda')^{b_1/p}x_1, (\lambda')^{b_2/p}x_2, \dots, (\lambda')^{b_n/p}x_n] = \lambda' f(x_1, x_2, \dots, x_n) \quad (\text{A.6})$$

Now replacing λ' by λ , and denoting the exponents b_i/p by a_i , yields the following form for the generalized homogeneous function

$$f(\lambda^{a_1}x_1, \lambda^{a_2}x_2, \dots, \lambda^{a_n}x_n) = \lambda f(x_1, x_2, \dots, x_n) \quad (\text{A.7})$$

Homogeneity is quite a restriction to the function itself. The value of $f(\mathbf{r})$ at any point $(\lambda^{a_1}x_1, \lambda^{a_2}x_2, \dots, \lambda^{a_n}x_n)$ is related, by a simple change of scale by a factor λ , to the value at point (x_1, x_2, \dots, x_n) , although this change of scale is in general anisotropic (as the fixed exponents a_1, a_2 etc. are all different). Therefore a closed surface encircling the origin contains full information about the function.

Bibliography

- [1] B. R. Coles, B. V. B. Sarkissian, R. H. Taylor, Philosophical Magazine B, 36(4)489(1978)
- [2] V. Cannella, J. A. Mydosh, Phy.Rev. B, 6(11)4220(1972)
- [3] Z. Wang, H. P. Kunkel, G. Williams, J. Phys. Condensed Matter, 2,4173(1989)
- [4] Z. Wang, H. P. Kunkel, G. Williams, J. Phys. Condensed Matter, 4,10385-98(1992)
- [5] H. Ma, H. P. Kunkel, G. Williams, J. Phys. Condensed Matter, 3,5563(1991)
- [6] D. Sherrington, S. Kirkpatrick, Phys. Rev. Lett., 35(26)1792(1975)
- [7] H. P. Kunkel, M. S. Westmore, G. Williams, Philosophical Magazine B, 65(6)1207(1992)
- [8] S. B. Roy, B. R. Cloes, J. Appl. Phys. 63(8)4094(1988)
- [9] S. B. Roy, B. R. Coles, Phys. Rev. B. 39(13)9360(1989)
- [10] S. J. Kennedy, B. R. Coles, J. Phys: Condens Matter, 2,1213-1222(1990)
- [11] Y. Nishihara, M. Tokamoto, Y. Yamaguchi, J. M. M. M. 70,173(1987)
- [12] G.Kido, Y.Nakagawa, Y.Nishihara, F.Iga, J. M.M.M. 90-91,75(1990)

- [13] J. Eynon, N. Ali, J. Appl. Phys. 69(8)5063(1991)
- [14] Y. S. Yang, B. D. Gaulin, J. Appl. Phys. 73(10)6066(1993)
- [15] N.Ali, X.Zhang, J.Phys.,Condensed Matter, 4,L351(1992)
- [16] S.J.Kennedy, A.P.Murani, B.R.Coles, O.Mozes, J.Phys.F, 18,2499(1988)
- [17] Buschow, Ferromagnetic materials, (1985)
- [18] I. Maartanse, The Review of Scientific Instruments, 41(5)657(1970)
- [19] Roshko: Some electric and magnetic properties of Cr impurities dissolved in exchange enhanced hosts. Thesis. U. of M. (1979)
- [20] H. Eugene Stanley, Introduction to Phase transitions and Critical Phenomena (1971)
- [21] C. J. Shinkel, N. D. Van Amstel, Phys. Lett. 44A(7)467(1973)
- [22] A. H. Morrish, Physical Principles of Magnetism, (1965)
- [23] CRC, Handbook of Chemistry and Physics, (1983-84)
- [24] Magnetic susceptibility of superconductors and other spin systems. Edited by R. A. Hein *et al.* Plenum Press, New York 1991
- [25] R. M. Roshko, G. Williams, J. Phys. F: Met Phys, 14,703-9(1984)
- [26] J. S. Kouvel, M. E. Fisher, Phys. Rev. 136(6A)1626(1964)
- [27] S. N. Kaul, Ch. V. Mohan, preprint, submitted for publication